GEORG-AUGUST-UNIVERSITÄT
GÖTTINGEN

Development of InGaN/GaN nanostructures

Dissertation zur Erlangung des mathematisch-naturwissenschaftlichen Doktorgrades

Doctor Rerum Naturalium

der Georg-August Universität Göttingen

-

im Promotionsprogramm ProPhys
der Georg-August University School of Science (GAUSS)

vorgelegt von

Carla Ivana Oppo
aus Cagliari

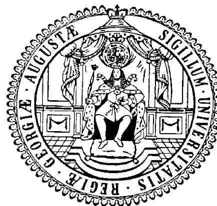

Göttingen – Dezember 2016

BETREUUNGSAUSSCHUSS:
Prof. Dr. Angela Rizzi
Dr. Jörg Malindretos

MITGLIEDER DER PRÜFUNGSKOMMISSION:
Referentin: Prof. Dr. Angela Rizzi
Korreferent: Prof. Dr. Hans Hofsäss

WEITERE MITGLIEDER DER PRÜFUNGSKOMMISSION:
Prof. Dr. Tim Salditt
Prof. Dr. Michael Seibt
Prof. Dr. Claus Ropers
Prof. Dr. Vasily Moshnyaga

TAG DER MÜNDLICHEN PRÜFUNG:

La *regola* è utile, ma quando la si segue pedissequamente è deleteria.

— F. Oppo

To *myself* and by mirroring
to all *that* people I met till now,
whose opinions for better or for worse
allowed me to became such person.

CONTENTS

1 INTRODUCTION 1

i THEORETICAL AND EXPERIMENTAL BACKGROUND 5

2 GENERAL PROPERTIES OF NITRIDES 7
- 2.1 Structural properties 7
- 2.2 Electronic properties 11
- 2.3 Polarization effects 13
  - 2.3.1 Quantum confined Stark effect (QCSE) 17
  - 2.3.2 Non-polar and semi-polar solutions 18
  - 2.3.3 Nanocolumn structures approach 19
- 2.4 InGaN material 20
  - 2.4.1 InGaN - Material properties and growth issues 20
  - 2.4.2 InGaN growth improvements 21

3 EXPERIMENTAL METHODS AND DEVICES 25
- 3.1 Pre-growth sample preparation 25
  - 3.1.1 Substrate preparation 26
  - 3.1.2 Mask preparation 26
  - 3.1.3 Mask characterization 29
- 3.2 MBE Growth of SAG nanocolumns 30
  - 3.2.1 The GENII system 31
  - 3.2.2 Molecular flux calibration 31
  - 3.2.3 Stoichiometric flux and growth rate 32
  - 3.2.4 Growth of SAG nanocolumns 34
- 3.3 Characterization techniques 36
  - 3.3.1 X-ray fluorescence (XRF) and diffraction (XRD) 36
  - 3.3.2 ID22NI: a hard X-ray microprobe beamline 38

ii RESULTS 41

4 SELECTIVE AREA GROWTH OF GaN NCs 43
- 4.1 Growth of GaN SAG NCs as a function of the ϕ_{Ga}/ϕ_N ratio 43
  - 4.1.1 Control of the ϕ_{Ga}/ϕ_N ratio 46
  - 4.1.2 Deviations from the SAG GaN NCs pencil-like structure 50
- 4.2 Growth of GaN SAG NCs as a function of time 52
- 4.3 Growth of GaN SAG nanopyramids 60
- 4.4 Results discussion 61

5 InGaN INCORPORATION ON GaN-BASED SAG NANOSTRUCTURES 67
- 5.1 Growth of epitaxial InGaN on GaN SAG NCs 67
  - 5.1.1 InGaN layers based growth conditions 67
  - 5.1.2 SAG NCs based growth conditions 71
- 5.2 Growth of epitaxial InGaN on GaN SAG NPs 73
- 5.3 Results discussion 77

6 InGaN INCORPORATION ON GaN-BASED SELF-ORGANIZED NANOCOLUMNS 79

6.1 MBE growth conditions 80
6.2 Characterization techniques 80
6.3 Characterization results 81
6.4 Results discussion 89
7 CONCLUSIONS 91

iii APPENDIX 93
A APPENDIX 95
A.1 Molybdenum or Titanium deposition at the Univex 350 95
A.2 Pattern a mask for SAG with electron beam lithography (EBL) 97

BIBLIOGRAPHY 103

1 INTRODUCTION

During the last two decades the interest on GaN-based materials for optoelectronic devices has significantly increased and great effort has been invested in the field of solid-state lighting, by the scientific community [1, 2] as well as by industry [3, 4, 5, 6]. In the last years, the achievement and production of white light emitting devices (LEDs), which are displacing incandescent lamps, has revolutionized the lighting market and finally led, in 2014, to the Nobel Prize award to its principal inventors [7]. Nevertheless, further improvements in efficiency and reduction in manufacturing costs are required to accelerate the adoption of the white LED technology.

Conventional white LEDs are currently assembled by combining blue LEDs with yellow phosphors. This solution, which dominates the white LED industry, is easy to manufacture and therefore very attractive for the creation of cheap and bright white light sources. However, the employment of phosphors brings to unavoidable energy conversion losses and low color rendering index (CRI), which make such LEDs undesirable for indoor use. For improving the CRI, white LEDs may also be set up by combining UV LEDs with red, green and blue phosphors, though this solution does not solve the efficiency problem of such devices.

A promising material for the development of a new generation of phosphor-free white LEDs, assembled by combining red, green and blue LEDs, is the $In_xGa_{1-x}N$ ternary alloy. In particular, this compound is characterized by a compositional dependent bandgap energy, which theoretically allows to continuously tuning the emitted light, from the infra-red to the ultra-violet range, through the whole visible spectrum [8]. However, the fabrication of such devices has proved to be very difficult to control, since the color and efficiency of LEDs, comprising $In_xGa_{1-x}N$ active layers, is deeply influenced by multiple detrimental effects occurring during the growth process. The huge difference in the physical and chemical properties of GaN and InN compounds, which brings to Ga incorporation promotion above In in the ternary alloy, has also been found to give rise to a strained and more defective crystal structure. Since the strain can be released through segregation of In atoms to the surface, spinodal decomposition or phase separation, as a matter of fact it is very difficult to increase the In content to above ca 20% in a homogeneous ternary phase [9, 10, 11, 12, 13].

Considering the need of efficiency improvement, it is worth notice to say that current commercial LEDs are realized by assembling GaN-based planar heterostructures, which are far from being perfect, mostly due to the absence of a lattice-matched substrate. Furthermore, the lack of central symmetry of the III-N wurtzite structure, the most stable for nitrides materials, leads to the

presence of a unique polar direction, which is also the standard direction for the growth of epitaxial III-nitrides. Such directional anisotropy induces strong polarization electric fields in the heterostructures, leading to quantum confined Stark effect (QCSE). This intrinsic property strongly reduces the radiative recombination probability, due to the spatial separation of electrons and holes wave functions, which in presence of defects becomes an important limit for the internal quantum efficiency (IQE) of LEDs.

For all the above reasons the research community is putting a lot of effort in the growth of non-polar and semi-polar planar structures to get rid off the detrimental polarization issues [1, 14]. However the growth of high quality GaN-based material along the non-polar and semi-polar directions turns out to be a real challenge [2].

A promising approach to address the above mentioned complications, is given by the development of the selective area growth (SAG) of GaN-based nanocolumns (NCs), a growth technique which is emerging as an attractive research field.

First of all, due to the lack of lateral constraint, which allows to easily relieve the mechanical strain, the epitaxial growth of NCs with high aspect ratio suffers much less from the lattice mismatch than the corresponding planar structures. Secondly, the SAG approach enables the control over NCs position and density, as well as over their axial and radial dimensions. Therefore, SAG technique allows to overcome the typical and severe technological limitations of the disordered self-organized growth (SOG) of NCs, i.e. size and density inhomogeneities, as well as compositional fluctuation in the growth of heterostructures.

The large surface-to-volume ratio provided by these NC structures is a feature of high interest when 3D-core-shell NCs are grown, since the active region area per substrate area results effectively enhanced. However, in this perspective, the emission of light from the side faces of NCs ordered in array might also suffer from strong reabsorption processes [15].

For all mentioned reasons, another aspect of GaN-based SAG NCs has been the focus of this thesis. Particularly relevant for this work are the different facets (polar, non-polar and semi-polar) which appear, depending on polarity, by the growth of GaN-based NCs with different parameters. Their control through the growth conditions might offer a further degree of freedom as compared to epitaxial layers. In particular, dense regular arrays of Ga-polar nanocolumns might serve as a template of semi-polar $\{1\bar{1}0n\}$ facets for the growth of InGaN/GaN multi quantum wells (MQWs), which will not be affected by the strong polarization fields present along the polar directions [1].

Following the investigations of our research group former colleague A. Urban [16], an additional study has been implemented in this work on the growth mechanisms regulating the formation of SAG GaN NCs as a function of the different growth parameters. The samples have been grown by molecular beam epitaxy (MBE) on a patterned $10\,nm$ thick Mo or Ti layer deposited on commercial $GaN(0001)/Al_2O_3$ templates. The morphology of the samples has been in-

vestigated by scanning electron microscopy (SEM), while a structural analysis has been performed by means of transmission electron microscopy (TEM).

Once the mechanisms behind the SAG of GaN NCs have been better understood, the additional growth of epitaxial InGaN on the NCs tip has been investigated. Also in this case different growth conditions have been applied to the growth of InGaN heterostructures, by considering the optimized scheme developed for the growth of epitaxial InGaN layers in our system [17], as well as by taking into account the procedures known from the state of the art [15, 18, 19, 20, 21, 22, 23]. Due to the heterogeneous distribution of indium and the low In/Ga samples composition, which result in very poor signal/background ratio, the investigation of GaN/InGaN heterostructured NCs is not trivial matter and high spatial resolution analysis are needed. For these samples, besides SEM and TEM analysis, the formation and composition of InGaN heterostructures has been therefore investigated by SEM chatodoluminescence (SEM-CL).

Finally, disordered self-organized (SOG) NCs, grown on the metal masks, due to parasitic nucleations during the growth of GaN/InGaN SAG NCs, have been investigated by means of several high-spatial resolution techniques. Following experimental [24, 25, 26] and computational [27] evidence in literature, which report In incorporation to be easier on GaN $\{000\bar{1}\}$ (N-polar) than on GaN $\{0001\}$ (Ga-polar) epitaxial layers, these structures turn out to be very interesting for studying the growth of InGaN/GaN heterostructures on GaN-based N-polar NCs. For these samples, the elemental composition and crystal structure of several SOG single GaN/InGaN NCs have been investigated by means of non-standard techniques, such as nano-X-ray fluorescence (nano-XRF) and X-ray diffraction (nano-XRD) imaging, which further allowed to study the axial and radial elemental distribution in single NCs.

In this work, several aspects of the growth mechanisms of SAG and SOG GaN-based NCs have been investigated and special attention has been put on the formation of InGaN heterostructures along different crystallographic directions. The aim of this study has been therefore that of giving a better understanding of the realistic possibilities of InGaN heterostructures inclusion on GaN-based NCs ordered arrays, for the development of alternative phosphor-free NCs-based LEDs technologies.

TEM and STEM analysis has been performed by Dr. Reza R. Zamani, SEM-CL have been recorded by Dr. Markus Müller in a collaboration with the Otto-von-Güricke University of Magdeburg, nano-XRF and nano-XRD imaging analysis have been carried out at the nano-imaging beamline ID22NI of the European Synchrotron Radiation Facility (ESRF) of Grenoble (France), under the mentoring of Dr. Gema Martínez-Criado and Dr. Jaime Segura-Ruiz, single NC μ-PL analysis has been performed by Dr. Pier Carlo Ricci at the University of Cagliari (Italy).

Part I

THEORETICAL AND EXPERIMENTAL BACKGROUND

2 GENERAL PROPERTIES OF NITRIDES

The first chapter of this thesis is aimed to introduce the theoretical background necessary for the understanding of the fundamental properties which characterize group III-nitride materials. First of all, a review of III-nitrides structural and electronic properties is presented, followed by an introduction to the polarization effects affecting their most common crystal structures and some possible solutions in this regard. Afterwords, the focus will move on the properties and growth issues of $In_xGa_{1-x}N$ alloys.

As references, the book by Morkoç [28] and Grundmann [29] are used, while additional references are suggested where necessary.

2.1 STRUCTURAL PROPERTIES

At ambient condition, the thermodynamically most stable crystal structure in which III-nitrides semiconductor compounds crystallize is the *wurtzite (WZ)*. Under certain conditions it is possible to grow or observe a phase transition to the metastable *zinc blende (ZB)*, whilst upon application of very high pressures the *rocksalt* structure *(RS)* can be induced. In this work, only the first two lattice structures will be focus of interest and thus introduced.

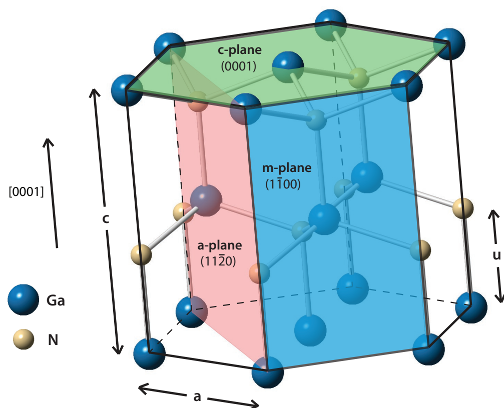

Figure 1: Ball-stick model of GaN WZ unit cell showing the polar *c-plane* (green) and non-polar *m-* and *a-planes* (blue and pink), as well as the ***u***, ***a*** and ***c*** parameters.

The *WZ lattice*, also known as *hexagonal* or *α-phase*, consists of two interpenetrating hexagonal close-packed *(hcp)* structures, one composed of group-III atoms and the second of nitrogen atoms. Each atom is tetrahedrally coordinated, while each (0001) *c*-plane is regularly piled, along the [0001] *c*-direction, with stacking order **AaBbAa**, where capital and small letters stand for the two different atoms involved.

The WZ structure is characterized by an *internal parameter* ***u***, defined as the anion-cation bond length along the [0001]-direction and by two lattice constants: the

Lattice constant	GaN	AlN	InN
u	0.377 Å	0.382 Å	0.379 Å
a	3.199 Å	3.110 Å	3.585 Å
c	5.227 Å	4.995 Å	5.800 Å

Table 1: Experimentally observed wurtzite structural parameter of the III-nitrides.

basal plane parameter $\boldsymbol{a}$ and the *axial parameter* $\boldsymbol{c}$, perpendicular to it. Their values are listed in Table 1, while the WZ ball-stick model of Figure 1 shows them, together with the most common planes: the polar c-plane (green) and the non-polar m- and a-planes (respectively blue and pink).

Since in this work particular attention is also given to the so called *semi-polar planes* of the *WZ lattice*, the graphical representation of GaN WZ common planes, as well as the angles they form with the c-plane, are shown in Figure 2(a). Furthermore, a telescopic representation of hexagonal symmetry points is depicted in Figure 2(b). Here dashed and bold lines help to visualize respectively the projection of m- and a-planes on the c-plane, while dotted lines are intended to show the symmetry only.

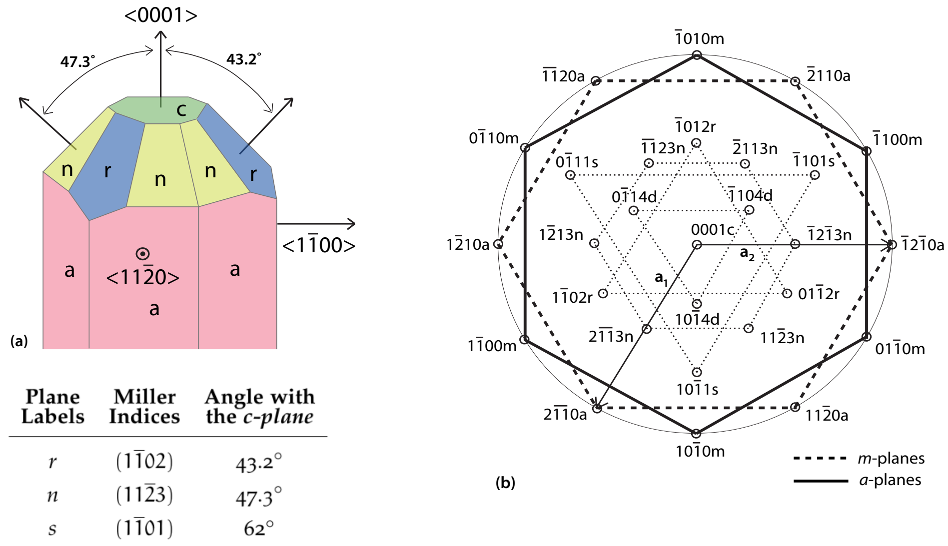

Plane Labels	Miller Indices	Angle with the *c-plane*
r	$(1\bar{1}02)$	43.2°
n	$(11\bar{2}3)$	47.3°
s	$(1\bar{1}01)$	62°

Figure 2: a) Graphical representation of GaN WZ, with labeling of crystallographic planes and family directions. b) Telescopic view of the planes labeling in hexagonal symmetry. Dashed and bold lines show the symmetry and the projection of m- and a-planes on the c-plane, while dotted lines show the symmetry only. Figures adapted from Ref. [28].

The *ZB lattice*, also known as *cubic* or β-*phase*, is composed of two interpenetrating face-centered cubic *(fcc)* sublattices of group-III and N atoms, with lattice constant given by $\boldsymbol{a}$. A ball-stick model of ZB GaN is shown in Figure 3(a-b). Also in this crystal structure each atom is tetrahedrally coordinated, but differently from the *WZ lattice* the stacking sequence for the (111) close-packed planes is **AaBbCc**. Stacking orders of WZ and ZB structures are shown in Figure 3(c-d).

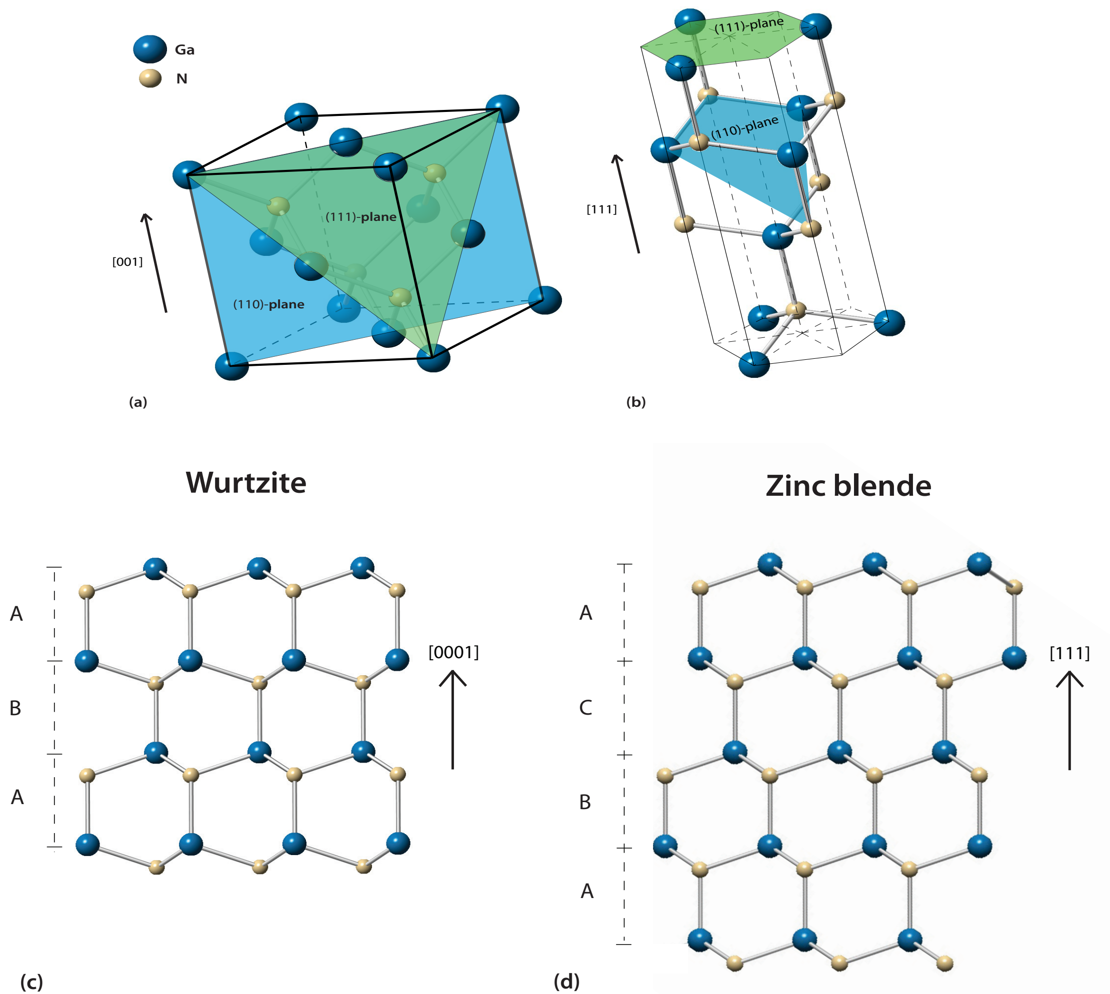

Figure 3: Ball-stick model of GaN ZB unit cell, along the (a) [001]- and (b) [111]-directions, showing the polar (111)-plane (green) and the non-polar (001)-plane (blue). (c) Stacking order of the WZ structure along the [0001]-direction and of the ZB structure along the [111]-direction.

Interestingly, these two crystallographic phases are energetically very close from their structural point of view. This similarity allows, under certain growth conditions, structural phase transitions which bring to WZ-ZB polytypism. The relationship between WZ and ZB crystal structure can be easily visualized

by looking at the ZB stacking sequence along the [111]-direction (Figure 3(b)). From this perspective it is possible to see the hexagonal symmetry of the ZB structure (C_3 rotational symmetry). More crystallographic details on the different III-nitride structures are listed in Table 2.

Crystal structure	Bravais lattice	Lattice vectors	Space group	
			H-M	S
WZ	Hcp	$a_1 = a\left(1/2, \sqrt{3}/2, 0\right)$ $a_1 = a\left(1/2, \sqrt{3}/2, 0\right)$ $c = c\left(0, 0, 1\right)$	$P6_3mc$	C^4_{6v}
ZB	Fcc	$a_1 = a\left(0, 1/2, 0\right)$ $a_2 = a\left(1/2, 0, 1/2\right)$ $a_3 = a\left(1/2, 1/2, 0\right)$	$F\bar{4}3m$	T^2_d
RS			$Fm\bar{3}m$	O^5_h

Table 2: III-nitrides crystal structures, related Bravais lattice, lattice vectors and crystallographic space group symmetry in Hermann-Mauguin (H-M) and Schönflies (S) notation.

When considering ternary alloys, as for example wurtzitic $In_xGa_{1-x}N$, *basal* $\boldsymbol{a}$ and *axial* $\boldsymbol{c}$ lattice constants are proportionally dependent to the mole fraction of the binary compounds and obey *Vegard's law* [30, 31]:

$$\boldsymbol{a}_{In_xGa_{1-x}N} = x\boldsymbol{a}_{InN} + (1-x)\boldsymbol{a}_{GaN} = (3.199 \pm 0.386x)\ \text{Å} \tag{1}$$

and

$$\boldsymbol{c}_{In_xGa_{1-x}N} = x\boldsymbol{c}_{InN} + (1-x)\boldsymbol{c}_{GaN} = (5.227 \pm 0.573x)\ \text{Å}. \tag{2}$$

2.2 ELECTRONIC PROPERTIES

III-nitride compound semiconductors are characterized by direct band-gaps, which make them of fundamental importance for optoelectronic applications, such as LEDs and laser diodes. Their conduction bands wave functions are composed of atomic *s*-orbitals, while their valence band wave functions of p^3-like orbitals. A schematic comparison of GaN wurtzitic and cubic band structures, near to the Γ-point, is shown in Figure 4(a-b). The fundamental difference between these two symmetries is given by the fact that, in the *ZB* phase, only the *spin-orbit interaction* acts on the degenerated valence bands to separate the so called *split-off* (SO) band, but the degeneracy of *heavy hole* (HH) and *light hole* (LH) bands at the Γ-point is still present.

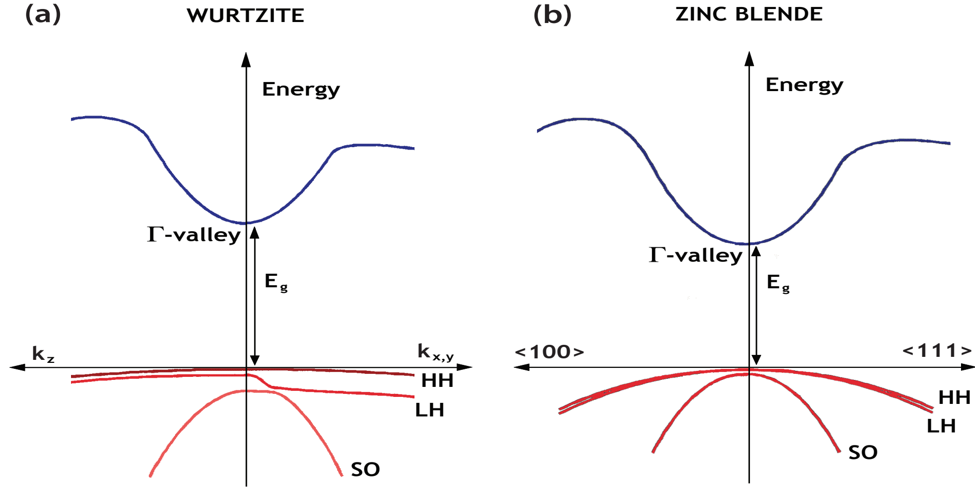

Figure 4: Schematic comparison of the Γ-point valence and conduction band structures of wurtzite (a) and zinc blende (b) symmetry such as GaN. The diagrams are not drawn to scale and are adapted from Ref. [28, 32].

Additionally to the spin-orbit interaction, the *WZ* crystal is also affected by the *crystal field* along the *c*-axis and therefore a triple splitting of its valence bands results in the formation of the so called heavy hole (HH, *A* band), light hole (LH, *B* band) and split-off (SO, *C* band), respectively. An additional representation of the sixfold degenerate Γ15 level splitting, in the cubic and hexagonal symmetry, is shown in Figure 5(a).

Assuming no localization effects, the temperature dependence of the band gap energy of semiconductors, follows the Varshni's formula [35]:

$$\mathbf{E}_G(T) = \mathbf{E}_G(T=0) - \frac{\alpha T^2}{(\beta + T)}. \tag{3}$$

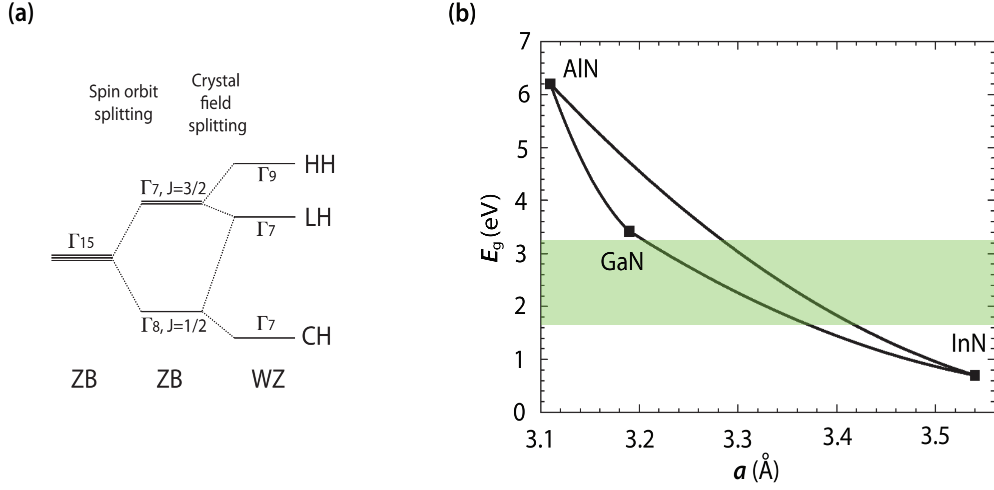

Figure 5: (a) Schematic illustration of valence bands separation under the influence of the spin-orbit (cubic symmetry) and the spin-orbit together with the crystal field (wurtzitic symmetry). Scheme adapted from Ref. [33]. (b) Room temperature bandgap energy as a function of the composition of AlInGaN alloys. The green band visualizes the bandgap energies corresponding to the visible range. Figure adapted from Ref. [34].

where α and β are fitting parameters characteristic of the material [36].

Already from the second half of the 1990s, nitrides materials attracted strong scientific interest, in particular due to the terrific potential offered by their combination into ternary alloys [37]. By now it is well known that, by controlling the composition of these systems, it is theoretically possible to continuously tune their band-gap from the near infra-red (IR) to the deep ultra-violet (UV) energy range. In particular, $In_xGa_{1-x}N$ alloys should allow to cover the whole visible range of wavelengths (Figure 5(b)), since the compositional dependence and the non-linearity of $In_xGa_{1-x}N$ band gap follow the equation [38]:

$$\mathbf{E}_g^{In_xGa_{1-x}N} = x\mathbf{E}_g^{InN} + (1-x)\mathbf{E}_g^{GaN} - x(1-x)\mathbf{b}^{In_xGa_{1-x}N}\ , \tag{4}$$

Where $\mathbf{E}_g^{GaN} = 3.4$ eV [39], $\mathbf{E}_g^{InN} = 0.7$ eV [40] and $\mathbf{b}^{In_xGa_{1-x}N}$ is the composition-dependent bowing parameter, which describes the band gap of InGaN alloys [38].

However, due to the important disparities between GaN and InN lattice constants, the growth of $In_xGa_{1-x}N$ materials revealed to be more complex and technologically challenging than that of $Al_xGa_{1-x}N$. The topic related to the growth difficulties of $In_xGa_{1-x}N$ alloys will be focus of Section 2.4.

2.3 POLARIZATION EFFECTS

The lacking center of inversion symmetry in the *WZ lattice* leads to very strong polarization effects in group III-nitride materials. The *total macroscopic polarization* ($\boldsymbol{P}$) of a solid, in absence of external fields, is given by the sum of the material intrinsic *spontaneous polarization* ($\boldsymbol{P}_0$) and the strain induced *piezoelectric polarization* ($\delta\boldsymbol{P}$),

$$\mathbf{P} = \mathbf{P}_0 + \delta\mathbf{P}. \tag{5}$$

The *spontaneous polarization* ($\boldsymbol{P}_0$), which is defined as the persistent polarization phenomenon in unstrained structures and in absence of applied external field, is not zero for nitrides materials along the usual growth [0001]-direction. For this reason the crystal surfaces result, as shown in Figure 6, either in a metal-polarity, also known as (0001)-polarity, or in a N-polarity, also known as $(000\bar{1})$-polarity. It is important to notice that (0001) and $(000\bar{1})$ surfaces are not equivalent and lead to different physical and chemical properties [41]. The spontaneous polarization turns out to be anti-parallel to the [0001]-direction for all wurtzitic III-nitrides materials [42, 43]. Its dependence on temperature has been found to be negligible [31]. The values of III-nitrides spontaneous polarizations calculated by Bernardini *et al.* [42] are the standard reference used today for this physical parameter.

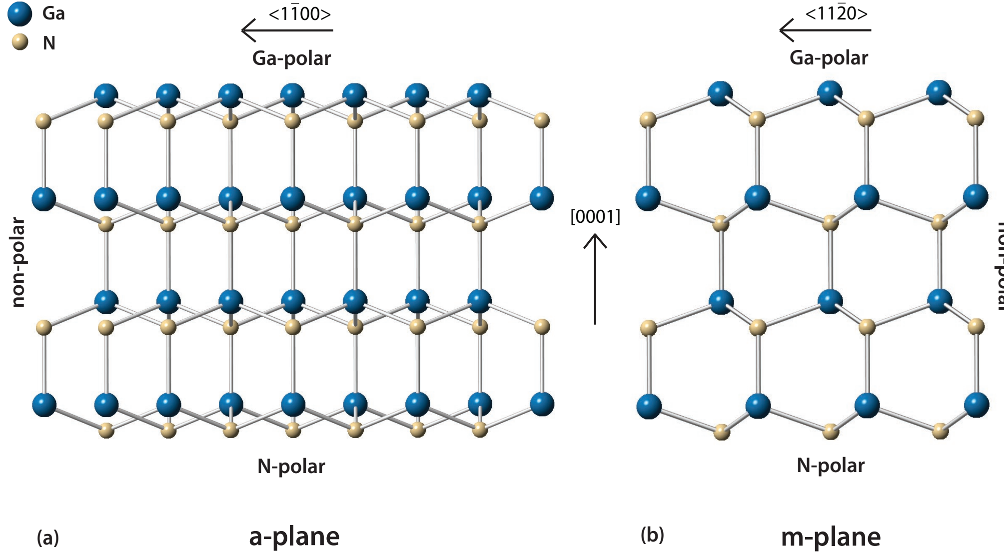

Figure 6: Ball-stick model of GaN *WZ lattice* from the point of view of the non-polar *a*- (a) and *m*- (b) planes. The characteristic metal- and N-polarity along the usual growth [0001]-direction are put in evidence.

With density-functional-theory (DFT) calculations in the generalized gradient approximations (GGA), Bernardini and Fiorentini [30] shown the spontaneous polarization of nitride ternary alloys to have a very large bowing parameter, strongly dependent on the alloy microscopic structure. For this reason and especially in the case of $In_xGa_{1-x}N$ alloy, where the binary constituents have a very large lattice mismatch, a non-linear dependence of the spontaneous polarization on the alloy composition has to be taken into account.

The spontaneous polarization, computed as a composition-weighted Vegard-like average of the polarizations of the binaries, takes the form [30]

$$\mathbf{P}_0^{In_xGa_{1-x}N} = x\mathbf{P}_0^{InN} + (1-x)\mathbf{P}_0^{GaN} - x(1-x)\mathbf{b}_{In_xGa_{1-x}N} , \quad (6)$$

where any non-linearity is treated by using a *bowing parameter*

$$\boldsymbol{b}_{In_xGa_{1-x}N} = 2\mathbf{P}_0^{InN} + 2\mathbf{P}_0^{GaN} - 4\mathbf{P}_0^{In_{0.5}Ga_{0.5}N} , \quad (7)$$

which keeps into account the response of polarization to perturbation in the alloy lattice constant *a(x)*. Using the numerical GGA values and the bowing parameter for random $In_xGa_{1-x}N$ alloy, Fiorentini *et al.* [44] further found the spontaneous polarization for arbitrary composition, in units of C/m^2, to be:

$$\mathbf{P}_0^{In_xGa_{1-x}N} = -0.042x - 0.034(1-x) + 0.038(1-x). \quad (8)$$

Nevertheless, due to the minimal difference between GaN and InN spontaneous polarizations ($\mathbf{P}_0^{GaN} = -0.029\ C/m^2$ and $\mathbf{P}_0^{InN} = -0.032\ C/m^2$) [42], as well as the low In content $\boldsymbol{x}$ generally incorporated within the ternary alloy (see Section 2.4.1), the interfaces between $In_xGa_{1-x}N$ and GaN in $In_xGa_{1-x}N/GaN$ heterostructures do not show, along the usual growth *c*-direction, an important discontinuity in spontaneous polarization.

On the other hand, due to the large lattice mismatch between the parental binary compounds, these multilayers are subject to huge elastic strain, which induce strong piezoelectric polarization discontinuities at the heterointerfaces.

The *piezoelectric polarization* ($\delta \boldsymbol{P}$) is a phenomenon related to the application of a mechanical stress, due to strain, to the crystal structure. In the linear regime and using Voigt notation, the piezoelectric polarization is related to the strain ε by [42, 31]

$$\delta P_i = \sum_j e_{ij}\varepsilon_j , \quad (9)$$

where e_{ij} and ε_j are the components respectively of the piezoelectric and strain tensor. By taking into account the hexagonal symmetry, the previous equation can be written as

$$\delta \mathbf{P} = \begin{pmatrix} 0 & 0 & 0 & 0 & e_{15} & 0 \\ 0 & 0 & 0 & e_{24} & 0 & 0 \\ e_{31} & e_{32} & e_{33} & 0 & 0 & 0 \end{pmatrix} \begin{pmatrix} \varepsilon_{xx} \\ \varepsilon_{yy} \\ \varepsilon_{zz} \\ \varepsilon_{yz} \\ \varepsilon_{xz} \\ \varepsilon_{xy} \end{pmatrix} = \begin{pmatrix} e_{15}\varepsilon_{xz} \\ e_{15}\varepsilon_{yz} \\ e_{31}(\varepsilon_{xx} + \varepsilon_{yy}) + e_{33}\varepsilon_{zz} \end{pmatrix}.$$

It is important to note that in the hexagonal symmetry the number of independent components of the piezoelectric tensor $\boldsymbol{e}$ is reduced to three, since $e_{24} = e_{15}$ and $e_{32} = e_{31}$ and that in absence of shear strain $\varepsilon_{yz} = \varepsilon_{zx} = \varepsilon_{xy} = 0$.

The strain experienced by an epitaxial layer grown on foreign substrate, is generally due to the presence of mismatch in the lattice constant *a* (the growth direction is usually along the *c*-direction) or mismatch in the thermal expansion coefficient of epilayer and substrate. Since the stress is present along the basal plane, the epitaxial layer undergoes a biaxial strain parallel to the substrate, while is free to relax in the *c*-direction, where no force is applied. Therefore, under biaxial strain

$$\varepsilon_{xx} = \varepsilon_{yy} = \frac{a - a_0}{a_0} \quad \text{and} \quad \varepsilon_{zz} = \frac{c - c_0}{c_0}, \tag{10}$$

where a and c are respectively the basal and axial lattice constants of the epilayer, with respect to the material relaxed crystal constants a_0 and c_0.

Considering the Hooke's law, the hexagonal symmetry and the Voigt notation, the stain ε_l applied to the crystal structure can be described by [31, 45]:

$$\sigma_k = \sum_l C_{kl}\varepsilon_l\ , \tag{11}$$

where σ_k are the internal or external stresses deforming the crystal and C_{kl} are the components of the elastic stiffness tensor:

$$C_{kl} = \begin{pmatrix} C_{11} & C_{12} & C_{13} & 0 & 0 & 0 \\ C_{12} & C_{11} & C_{13} & 0 & 0 & 0 \\ C_{13} & C_{13} & C_{33} & 0 & 0 & 0 \\ 0 & 0 & 0 & C_{44} & 0 & 0 \\ 0 & 0 & 0 & 0 & 0 & \frac{1}{2}(C_{11} - C_{12}) \end{pmatrix}. \tag{12}$$

Therefore, in the hexagonal symmetry, the biaxial strain ($\varepsilon_{xx} = \varepsilon_{yy}$) undergone by the epitaxial layer causes stresses $\sigma_1 = \sigma_2$, whereas σ_3 has to be zero. Using Equation 11 and Equation 12, the strain along the c-axis can accordingly be expressed in terms of the basal plane by

$$\varepsilon_{zz} = -2\frac{C_{13}}{C_{33}}\varepsilon_{xx}, \tag{13}$$

The non-vanishing component of the piezoelectric polarization along the z-direction can be then simplified to

$$\delta P_z = e_{31}\varepsilon_{xx} + e_{31}\varepsilon_{xx} + e_{33}\varepsilon_{zz} = 2\left(e_{31} - e_{33}\frac{C_{13}}{C_{33}}\right)\varepsilon_{xx}. \tag{14}$$

The piezoelectric polarization turns out to be in wurtzitic III-nitrides anti-parallel to the [0001]-direction for *biaxial tensile* strain and parallel to it for *biaxial compressive* strain. Since $In_xGa_{1-x}N$ heterostructures grown on GaN templates experience a compressive strain, due to InN larger lattice constants (see Table 1), their piezoelectric polarization results to be anti-parallel to the spontaneous polarization.
Also in this case, the values calculated by Bernardini *et al.* [42] are the standard reference used today for the piezoelectric constants of III-nitrides.

Also the piezoelectric polarization of ternary compounds has been demonstrated to be strongly non-linear in terms of the alloy composition [30]. Differently from the spontaneous polarization, this behavior is entirely due to the non-linear strain dependence of the bulk piezoelectric response and does not have structural origins. By taking into account the non-linearity of the piezo-polarization in binary compounds on the basal strain

$$\varepsilon_{xx}(x) = \frac{a_{subs} - a(x)}{a(x)}, \tag{15}$$

it is possible to predict the piezoelectric polarization of any alloy at any strain by using a Vegard interpolation [44]

$$\delta P^z_{In_xGa_{1-x}N}(x) = x\delta P^z_{InN}[\varepsilon_{xx}(x)] + (1-x)\delta P^z_{GaN}[\varepsilon_{xx}(x)], \tag{16}$$

where the basal strain dependent piezoelectric polarization of the binary compounds, in units of C/m^2, are

$$\delta P^z_{InN} = -\ 1.373\varepsilon_{xx} + 7.559\varepsilon^2_{xx} \tag{17}$$

and

$$\delta P^z_{GaN} = -\ 0.918\varepsilon_{xx} + 9.541\varepsilon^2_{xx}. \tag{18}$$

The basal strain can be calculated from the lattice constants of the unstrained alloy at x composition and of the substrate (see Section 2.1). As a consequence of Equation 13 and of the linear interpolation of elastic and piezoelectric constants, the piezoelectric polarization between the $In_xGa_{1-x}N$ heterostructure grown on GaN template and the unstrained GaN binary results nonlinear in terms of the alloy composition [31]:

$$\Delta(\delta P^{z}_{In_xGa_{1-x}N/GaN})(x) = [0.148x - 0.0424x(1-x)]\ C/m^2, \tag{19}$$

where the template is assumed to be totally relaxed and the epilayer fully and coherently strained.

In presence of shear strains also the *ZB lattice* shows piezoelectric polarizations, given by

$$\delta\mathbf{P} = e_{14}\begin{pmatrix}\varepsilon_{xz}\\ \varepsilon_{yz}\\ \varepsilon_{xy}\end{pmatrix},$$

where the coefficient e_{14} is equivalent to the coefficient e_{33} in the *WZ lattice*. In this structure, the strongest piezoelectric effect occurs when the growth of the heterostructure follows the [111]-direction, because the polarization results to be perpendicular to the interface ($\delta\mathbf{P}\perp$). For other orientations, like along the [110]-direction, the polarization became parallel to the interface ($\delta\mathbf{P}\|$), while for instance in all equivalent directions to the [001]-direction the strain tensor turns to be diagonal to the growth direction and no piezoelectric polarization is expected.

2.3.1 *Quantum confined Stark effect (QCSE)*

Polarization effects in nitrides materials became extremely important when considering GaN-based heterostructures, such as quantum wells (QWs). As shown in Figure 7(a), when the growth of heterostructures occurs along a polar-direction, the dishomogeneity of polarization experienced at the heterointerfaces, induces the formation of electric fields, which lead to a band banding of conduction and valence bands. As a result, electrons and holes wave functions are confined to the opposite ends of the interface. This spatial separation reduces the overlap of electron-hole pairs wave functions, which is generally experienced in absence of electric fields (Figure 7(b)). This phenomenon, know as *quantum confined Stark effect (QCSE)* results in an enlargement of the radiative lifetime,which in presence of non-radiative channels promotes non-radiative recombinations and lowers the emission efficiency. Moreover, the transition energy appears red shifted, due to the electric field induced

band banding. On the other hand, a blue shift of the transition energy can occur by increasing the carrier density, due to the consequent screening effect on the polarization field. The combination of these two effects determines the actual emission energy [43].

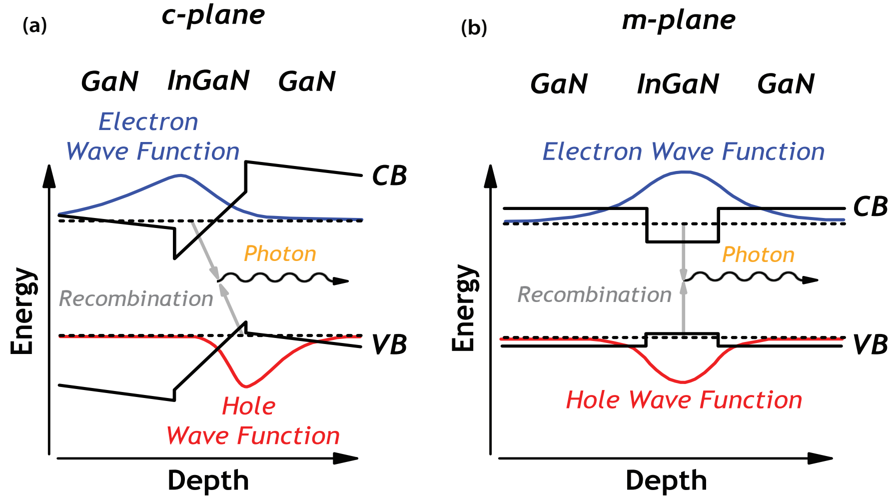

Figure 7: Schematic band diagram for a polar *c*-plane (a) and non-polar *m*-plane (b) $GaN/In_{0.1}Ga_{0.9}N(25Å)/GaN$ quantum well, obtained from self-consistent solutions of the Schrödinger and Poisson equations. It is easy to observe how the QCSE present along the polar direction leads to electron-hole pairs wave functions spatial separation. Along the non-polar direction, without this strong electric field, the ground-state electron and hole wave functions overlap. Figure adapted from Ref. [43].

2.3.2 *Non-polar and semi-polar solutions*

Different approaches have been developed to overcome the negative impact of the *QCSE*. Considering the growth along the *c*-direction of wurtzite crystal, which is currently the base of all commercial GaN-based LEDs, the excessive spatial separation of electron-hole pairs wave functions can be partially prevented by strongly limiting the width of the QWs active region (~ 2.5 nm) [1]. However, very thin QWs have the disadvantage of making the carrier injection into the active layer inefficient. Turning the growth of GaN-based LEDs from polar to non-polar or semi-polar crystallographic directions would reduce and even eliminate strain-induced polarization fields. Figure 8 shows the dependence of the total polarization discontinuity ($\Delta \mathbf{P}_z$) on the inclination angle relative to the *c*-plane for four different indium content $In_xGa_{1-x}N/GaN$ interfaces under biaxial compression. The inclination angle relative to the (0001) polar plane, the $(1\bar{1}00)$ non-polar plane and the most common $(11\bar{2}2)$ semi-polar plane are suggested.

It is interesting to note how the polarization discontinuity at the interface has been theoretically predicted to reach a zero point, not only and as expected for the growth along non-polar directions, but also for semi-polar planes having an inclination angle of about 45° relative to the *c*-plane [46]. This approach would also allow to the further optimization of the LED devices structure, by increasing the thickness of the QWs and thus their internal quantum efficiency (IQE) at high current density. However, these alternative planes impose their own challenges related to crystal quality and device design. For this reason, this topic is currently attracting important attention among the scientific community, as semiconductor growth techniques in non-polar and semi-polar crystallographic direction are still immature [47, 48, 49].

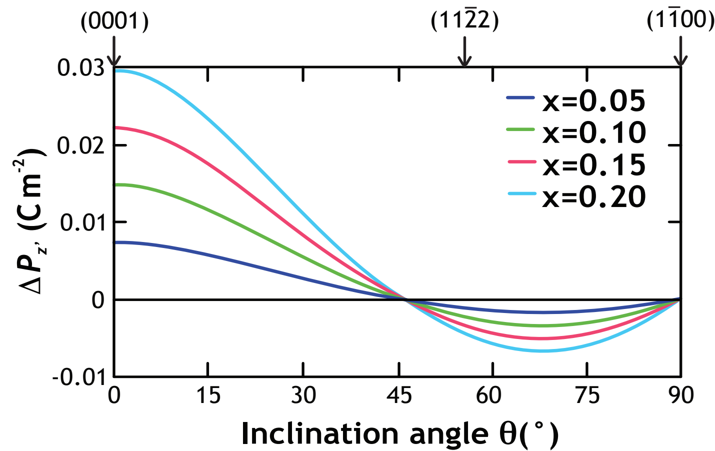

Figure 8: Dependence of the total polarization discontinuity (ΔP_z) on the semi-polar plane orientation θ, at a $In_xGa_{1-x}N/GaN$ interface under biaxial compression. Figure adapted from Ref. [46].

2.3.3 *Nanocolumn structures approach*

The growth of nanocolumns is nowadays an intensively studied technique, due to the promising potential of providing some solution to the previously illustrated issues.[15] First of all, the epitaxial growth of nanocolumns with high aspect-ratio suffers much less from the lattice mismatch than the corresponding planar structures. In fact, nanocolumn structures allow to easily relieve mechanical strain due to the lack of lateral constraint and therefore to reduce the dislocation density, especially on the top of the nanocolumns. Also the strain related to thermal expansion mismatches between GaN epilayers and foreign substrates, can be in this way relieved, offering important perspectives for the growth of optoelectronic materials and devices on Silicon substrates. Furthermore, the large surface-to-volume ratio provided by these structures is a feature of high interest when 3D-core-shell nanocolumn structures are

grown, since the active region area per substrate area results effectively enhanced. However, in this perspective, the emission of light from the side faces of nanocolumns ordered in array morphologies might also suffer from strong reabsorption processes [15].

Particularly relevant for this thesis are the different facets (polar, non-polar and semi-polar) which appear, depending on polarity, by the growth of GaN-based nanocolumns with different parameters. Their control through the growth conditions might offer a further degree of freedom as compared to epitaxial layers. In particular, dense regular arrays of Ga-polar nanocolumns might serve as a template of semi-polar $\{1\bar{1}0n\}$ facets for the growth of InGaN/GaN multi quantum wells (MQWs), which will not be affected by the strong polarization fields present along the polar directions [16].

2.4 InGaN MATERIAL

The InGaN ternary alloy is considered a key material for the development of new generation light emitting devices, since the compositional dependence of its bandgap energy theoretically allows to continuously tune the light emitted, from the infra-red to the ultra-violet range, through the whole visible spectrum (see Figure 5(b)). However, the fabrication of such devices has proved to be very difficult to control, since the color and efficiency of a LED, comprising $In_xGa_{1-x}N$ active layers, is deeply influenced by multiple detrimental effects occurring during the growth process.

2.4.1 *InGaN - Material properties and growth issues*

The first material issue faced during the growth of GaN-based heterostructures arises from the huge mismatch in the *basal lattice constant* $\boldsymbol{a}$ of nitride binary compounds. Although the difference between AlN and GaN lattice constants ($\Delta \boldsymbol{a}/\boldsymbol{a} \cong 2.5\%$) allows the growth of relatively high quality $Al_xGa_{1-x}N$ alloys, the same does not occur when considering InN and GaN, where the lattice constants mismatch of about $\Delta \boldsymbol{a}/\boldsymbol{a} \cong 10\%$ [50] introduces a biaxial compressive strain in the $In_xGa_{1-x}N$ epitaxial layer, which brings further polarization at the interfaces, with consequent deformation (increasing) of the bandgap energy as compared with the unstrained state [12]. In fact, due to notably different atomic radii for covalent tetrahedral bonding ($\boldsymbol{r}_{Ga}$ = 126 pm and $\boldsymbol{r}_{In}$ = 144 pm) [51], the presence of In atoms in the crystal structure generates strain in the epitaxial layer, which further increases for higher In content. To minimize the strain forming as a consequence of In atoms inclusion, the material system attempts to hold a composition with no mismatch with the underlying

Lattice mismatch

Atomic radius mismatch

layer and thus, during the growth process, Ga atoms adsorption is promoted over In [12]. This phenomenon, further supported by chemical effects, such as the weaker energy of In-N bonds ($\boldsymbol{E}_{In-N} \cong 7.7\ eV/atom$) as compared with that of Ga-N bonds ($\boldsymbol{E}_{Ga-N} \cong 8.9\ eV/atom$)[52], allows a strain release which results in undesired In atoms segregation to the material surface [27].

Bonding energy mismatch

In segregation

The poor matching of physical and chemical properties between GaN and InN has also been found to give rise to a solid phase miscibility gap [9]. Figure 9(a) shows the calculated temperature dependence of *binodal* and *spinodal curves* in $In_xGa_{1-x}N$ alloy at equilibrium. It is worth to remember that in thermodynamics the *binodal curve* set the conditions at which two distinct thermodynamic phases may coexist, while the *spinodal curves* is the limit of local stability of a solution. Therefore, depending on the growth temperature, the alloys with nominal composition falling between the two binodal lines are expected to be metastable with respect to compositional fluctuations, while the region between the two spinodal lines is considered the limit over which the compound is thermodynamically unstable. As a result, at typical InGaN growth temperatures, even for really low In-concentration, the material is expected to be affected by a phase separation which brings to the formation of non-uniform alloy composition, with extremely In-poor as well as In-rich InGaN regions. At long last, the growth of high quality InGaN/GaN epitaxial layers has proven to be very difficult also due to the different temperatures at which InN and GaN are generally grown. During the growth process the decomposition rates and mechanisms are strongly influenced by multiple parameters, such as temperature, pressure, fluxes of metal beams and nitrogen gas flow. For this reason nitrides dissociation temperatures are generally found to be within the range of $T_{S_{Ga}} = (800-900)°C$ for (0001) GaN material and already for temperatures as low as $T_{S_{In}} = 470°C$ for (0001) InN [53]. Because of this huge difference, the preparation of any $In_xGa_{1-x}N$ alloy, as compared with that of GaN, requires extremely lower growth temperatures, which detrimentally affect the quality of the grown crystal.

Miscibility gap

Phase separation

Decomposition temperatures mismatch

As a consequence of all these factors, no efficient InGaN-based green-light emitting devices are currently available and the optoelectronic potentialities offered by $In_xGa_{1-x}N$ alloys have still to be fully put into use. Owing to it, the interest on this topic continuously developed up to the present and a lot of scientific effort is currently put into this field for a better understanding of indium incorporation processes and their dependence on the growth parameters. The last years have seen therefore a multiplication of theoretical and experimental reports aiming to improve and control indium incorporation in GaN-based materials. The following subsection provides an overview of the most relevant research paths that have been followed in this work.

2.4.2 *InGaN growth improvements*

It is well known that the growth of III-nitrides smooth films requires temperatures of about half of the melting point of the growing material ($T_{melt_{Ga}} =$

2791 K, $T_{melt_{In}} = 2200$ K, $T_{melt_{Al}} = 3487$ K) [54]. However, under MBE conditions, this would mean growing GaN, InN and $In_xGa_{1-x}N$ alloys at temperatures higher than that of the material decomposition, which are therefore not applicable. For these reasons, the growth of layers has anyway to take place at high desorption temperatures, which result in limited adatom diffusion and consequent rough surface morphologies, when stoichiometric condition are applied. Nevertheless, it has been shown that the growth of GaN under Ga bilayer conditions leads to an enhancement of diffusion mechanisms, with consequent improvement of surface morphologies [55, 56]. A similar effect has been observed also when growing GaN under In adlayer conditions. By computing the diffusion barriers of N adatoms on GaN clean surface and under In adlayer, which resulted respectively of ~ 1.3 eV and ~ 0.5 eV, Neugebauer *et al.* [55] have demonstrated how the presence of a thin metallic layer on the surface allows the formation of an efficient channel for adatoms lateral diffusion (*In surfactant effect*). The presence of lower energy barriers leads in fact to faster diffusion of adatoms at the surface. Adatoms form therefore a less defective surface structure, because they are able to avoid to get immediately trapped by local energy minima.

In self-surfactant effect

The same reasoning holds also when $In_xGa_{1-x}N$ alloys are grown [57]. In this case Ga bilayer stabilized conditions cannot be applied because, as already mentioned, Ga incorporation is energetically favoured over that of In. A growth process under metal-rich conditions $(Ga + In > N)$ with Ga fluxes above the GaN stoichiometry $(Ga > N)$ would therefore prevent In to incorporate into the growing material. A controlled In incorporation, together with a better crystal quality can be reached by maintaining the metal-rich conditions, while keeping Ga fluxes below the GaN stoichiometry $(Ga + In > N$ and $Ga < N)$. The In content can in this way be directly deduced from the equation:

$$x_{In} = 1 - \frac{Ga}{N}, \tag{20}$$

while the remaining In atoms accumulate at the surface of the material.

However, particular attention has to be paid on fluxes and growth procedures. In fact, the temperatures generally used for the growth of InGaN do not allow sufficient desorption of In atoms from the surface. This means that, if In fluxes are more than slightly above the stoichiometry, In droplets may form at the material surface, vanishing the role of the surface In layer diffusion channel.

Indium self-surfactant effect has been experimentally shown also in the doctoral thesis of our research group former colleague Daniel Broxtermann [17].

From the phase diagram of Figure 9(a), it seams to be impossible to incorporate more than $x = 20\%$ of In within the $In_xGa_{1-x}N$ alloy. However, since the growth process is not an equilibrium condition, Broxtermann could optimize the growth parameters for our MBE system by finding a high growth temperatures window ($T_s = 570 - 650$°C), on which it is possible to grow InGaN/GaN heterostructured layers with quite high In-incorporation (up to $x = 21\%$). This has been achieved by increasing the In/N ratio enough to allow the forma-

tion of a stabilized indium bilayer and until a point for which In droplets formed at the surface. As already mentioned, the formation of a stable indium bilayers can be reached only for sufficient indium desorption, which requires substrate temperatures above 570°C, however no InGaN growth has been observed above $T_s = 650°C$. Figure 9(b) shows the XRD θ/2θ scans of InGaN/-GaN layers heterostructures grown under indium bilayer stabilized conditions at $T_s = 620$ °C, Ga/N = 0.8 and stoichiometric In-flux In/N = 0.2, 0.7, 1.0, 1.6 [17]. It is possible to observe that, under such growth conditions, In incorporation is not determined anymore only by T_s and Ga/N ratio, but also by the In flux. In particular, it is evident that x_{In} increases with the indium supply, with very little indium incorporation under stoichiometric conditions.

In growth under stabilized In bilayer

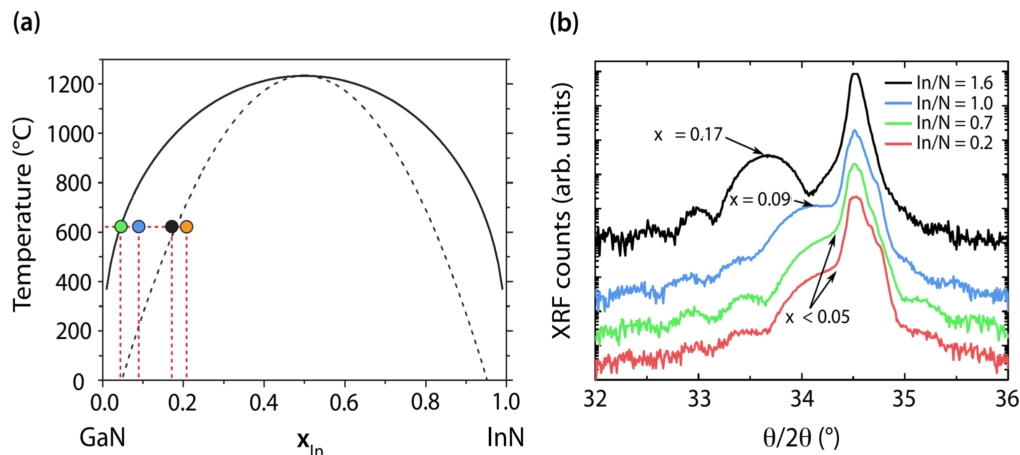

Figure 9: (a) Calculated temperature dependent binodal (black solid) and spinodal (black dashed) curves for $In_xGa_{1-x}N$ alloys at equilibrium. Figure adapted from Ref. [12]. The colored points refer to the experimental results of Broxtermann [17] for InGaN/GaN layers heterostructures grown under indium bilayer stabilized conditions at Ts = 620 °C, Ga/N = 0.8 and stoichiometric In-flux In/N = 0.7 (green), 1.0 (blue), 1.6 (black), 2.25 (orange). (b) XRD θ/2θ scans of InGaN/GaN layers heterostructures grown under indium bilayer stabilized conditions at Ts = 620 °C, Ga/N = 0.8 and stoichiometric In-flux In/N = 0.2, 0.7, 1.0, 1.6. Figure adapted from Ref. [17].

Although the (0001) Ga-polar surface currently represents the most technological relevant plane for the growth of III-nitrides materials, experimental evidences in literature [24, 25, 26] suggest indium incorporation to be easier on the $(000\bar{1})$ N-polar surface, so that higher temperatures can be used for a given indium concentration.

Duff *et al.* [27] have recently investigated the dependence from the growth plane of In incorporation and segregation. In their report, density-functional-theory (DFT) calculation in the generalized gradient approximations (GGA)

has been employed, together with a supercell approach and a large number of configurations (Ga and In adatoms, adlayers, bilayers, trilayers, mixed structures and several In_{Ga} orderings), to estimate surface energies for Ga-polar and N-polar surfaces of $In_{0.25}Ga_{0.75}N$. As they reported, indium self-surfactant effect occurs for both surface polarities under In-rich as well as N-rich growth conditions and it is followed by a greater In incorporation as compared with the clean surface structure. However, all possible reconstruction energies have been found to be lower for the N-polar surfaces by about 0.4 eV. Additionally, the driving force pushing In_{Ga} to the first layer, with consequent In segregation, is reported to be greater for Ga-polar rather than for N-polar surfaces. As a matter of fact, the In segregation in this system is detrimentally supported by a lower energy barrier for In atoms to be dragged into the vacuum, which has been quantified to be $E_{In}^{vac} \sim 2.5$ eV for Ga-polar and $E_{In}^{vac} \sim 7$ eV for N-polar surfaces. Therefore and notwithstanding the technological difficulties related to the availability of high quality N-polar GaN templates [58], the growth of InGaN/GaN heterostructures along the $[000\bar{1}]$-direction is surely a promising way to improve In-incorporation in the epitaxial layer.

Higher In-inclusion for N-polar surfaces

Lower In-segregation for N-polar surfaces

In Section 2.3.2, the possibly of growing InGaN/GaN heterostructures on non-polar and semi-polar surfaces has been introduced, since these directions would allow to reduce and in some case fully take back the negative impact of the QCSE. In addition to that, Northrup [59] reported calculations supporting an In incorporation enhancement on semi-polar surface $(11\bar{2}2)$ as compared to polar (0001) and non-polar $(10\bar{1}0)$ surfaces, due to the fact that In incorporates on the semi-polar surface at a significantly lower indium chemical potential.

Higher In-inclusion for semi-polar surfaces

All considerations reported above have been took into account as starting point for the work carried out in this thesis.

3 EXPERIMENTAL METHODS AND DEVICES

This chapter briefly introduces the experimental techniques and technical equipment used in this work to perform the sequential steps needed in the substrate preparation procedure, growth of nanocolumns and investigation of samples. Deeper attention will be put on those techniques which are not of common use in our research group, while for more details on conventional techniques and methods, the reader will be referred to previous works carried out by former colleagues or to the literature.

As previously introduced, in this work the attention has been focused on two main correlated topics. First of all, a more complete understanding of the growth processes involved in the molecular beam epitaxy of selective area growth (SAG) GaN nanocolumns, which continues the studies carried by our former colleague Arne Urban [16, 60] and which will be discussed in Chapter 4. Secondly, the use of these GaN-based nanocolumns arrays as ground structure for the additional growth of InGaN/GaN heterostructures, which will be the focus of Chapter 5 and 6. The experimental methods and devices involved in performing these investigations are described in this chapter.

3.1 PRE-GROWTH SAMPLE PREPARATION

The samples presented in this work have been generally grown homoepitaxially on commercially available $Al_2O_3/GaN(0001)$ templates. In particular, the templates produced by *Saint-Gobain LUMILOG* [61] have been selected, among others for their low dislocation density (in the upper $10^7 cm^{-2}$), which has been found to be essential for the growth of SAG nanocolumns with good crystal quality. Attempts of SAG nanocolumn growth on different substrates have been reported by Arne Urban in his doctoral thesis [60] (SiC substrates) and by Bastian Henne in his master thesis [62] (other $Al_2O_3/GaN(0001)$ templates).

3.1.1 *Substrate preparation*

Substrate cutting:

In a first step of preparation, the substrate wafer is cut, by means of a dicing saw, in several pieces of 1x1 cm^2, dimension suitable for their insertion into the sample holders of our MBE machine.

Sample cleaning:

The 1x1 cm^2 templates are afterwards cleaned by standard procedure in a ultrasonic bath (USB) following these steps:

- 2 min USB level 2 in $(CH_3)_2CO$ (Acetone)
- 2 min USB level 2 in CH_3OH (Methanol)
- 2 min USB level 2 in distilled H_2O
- Dry the sample with the N_2 gun

After the cleaning step in $(CH_3)_2CO$ it is important to squirt the sample with CH_3OH before putting them into the CH_3OH dewar (the same apply, with distilled H_2O, to the step between CH_3OH and distilled H_2O). In this way chemical contamination between the used and clean solutions can be avoid.

3.1.2 *Mask preparation*

Metal deposition on the template surface:

The mask used to achieve the growth of SAG nanocolumns consists of 10 nm thick Mo (or Ti) layer. The metal is deposited by means of electron beam evaporation on the suitable template surface. The metal deposition is performed under medium/high vacuum in a *Univex* 350 from Oerlikon Leybold Vacuum (see Urban's thesis for further details on the device) [60]. A step-by-step guideline for performing the Mo (or Ti) deposition at the Univex machine is reported in Section A.1.

Resist spin coating:

After the metal deposition, the samples are ready to be spin coated with a positive resist, necessary to perform the lithography of the mask. The resist used for this purpose is the $MicroChem's$ $PMMA$ *(Polymethyl mathacrylate)* 905 $A-2$, while the spin coater device is an OPTIspin SB20 from SSE Sister Semiconductor Equipment GmbH. The spin coating procedure follows the upcoming steps:

- Center the sample on the spin coater suction hole
- Turn on the vacuum
- Clean the sample with the N_2 gun

- Deposit 40μl of resist on the sample
- Start the spinning program **ST6k60p**:
  6000 round/min for 1 min (the resist will be then ~ 60μm thick)
- Heat the sample for 5 min at 180°C

The latter step allows to evaporate the solvent solution contained in the resist and leave the cured organic polymer compound on the sample.

It is recommended to clean the sample again with the standard process indicated before, but ***without*** the use of ultrasonic bath (this would, in fact, damage the metal surface and therefore compromise the outcome of the sample), if the spin coating procedure is not conducted directly after the metal deposition. After the cleaning step, it is also good to prevent any possible threaten of the sample due to the presence of residual organic solvents, by heating the sample for 1 min at 90°C.

Mask patterning:
The samples are now ready to be introduced in the Electron Beam Lithography (EBL), where the mask is patterned. This step is performed in the *Raith eLiNE* machine, a scanning electron microscope (SEM) equipped with high focused electron beam and characterized by an extremely precise sample alignment. For an overview of *eLiNE* characteristics, it is possible to consult Henne's Master Thesis [62], while a step-by-step guideline for performing the lithography of the metal mask for SAG is additionally reported in Section A.2.

Developing step:
During the electron beam exposure, resist polymer chains break and become dissoluble. For this reason, after the lithography a developing step is performed to remove the polymers from the exposed areas. The developer solution used in this process is the MIBK/IPA with ratio 1 : 3. The developing process is made following the upcoming steps:

- Slew 30 sec the sample in cold MIBK/IPA 1 : 3 developer (ice bath)
- Directly after, stop the reaction by dropping the sample in isopropanol for about 1 min
- Dry the sample with the N_2 gun

Etching of the mask:
To transfer the lithographed pattern from the resist level to the metal mask, an etching step is performed in a *Reactive Ion Etching Cluster Tool* (RIE), the *Oxford Instruments PlasmaLab* 100.

To avoid contaminations with previously run recipes, it is a good routine to perform a cleaning with oxygen in the RIE chamber to be used. This step needs about 30 min to be completed and therefore can be already initialized before

starting the previous reported developing step. The recipe to be started with empty RIE chamber is:

- *Clean* CH3 (for 15 min)

To further reduce the risk of contaminations, after the cleaning step it is appropriate to perform a dummy run of the etching recipe with an $Al_2O_3/GaN(0001)$ dummy sample.
The etching proceedings is summarized as following:

Process for the etching of 10 nm *Mo mask*:
- Clean the chamber 3 (CH3) with the recipe *cleanchamber(*CH3*)* for 15 min
- Put a dummy sample of $Al_2O_3/GaN(0001)$ in the *Main Chamber* and start the process *Mo@ch2* with the following parameters:

Used gasses	SF_6 60 sccm
	Ar_6 20 sccm
Pressure	60 mTorr
Power	35 *W*
Temperature	Room Temperature
Etching time	70 sec

- Remove the dummy sample, insert the real sample in the *Main Chamber* and start again the process *Mo@ch2* again, but with etching time of 51 sec
- Remove the sample

Process for the etching of 10 nm *Ti mask*:
- Open the BCl valve in the *gray room*
- Clean the chamber 1 (CH1) with the recipe *cleanchamber(*CH1*)* for 15 min
- Put the sample in the *Main Chamber* and start a process with the following parameters:

Used gas	BCl_3 10 sccm
Pressure	10 mTorr
Power	100 *W*
Temperature	Room Temperature
Etching time	55 sec

- Remove the sample
- Close the BCl valve in the *gray room*
- Clean the chamber 1 (CH1) with the recipe CH1-*pump back BCl3* for 30 min

Remover:
Finally a remover step with *Allresist* $AR300-70$ is performed to clean the mask surface from the last residues of resist. The procedure follows the upcoming steps:

- Sample plunged in remover $AR300-70$ for 30 min
- Squirt with a syringe full of remover the sample surface for at least 5 times (to optimize the remover action in the nanoholes of the mask)
- Clean the sample for 2 min in distilled H_2O
- Dry the sample with the N_2 gun

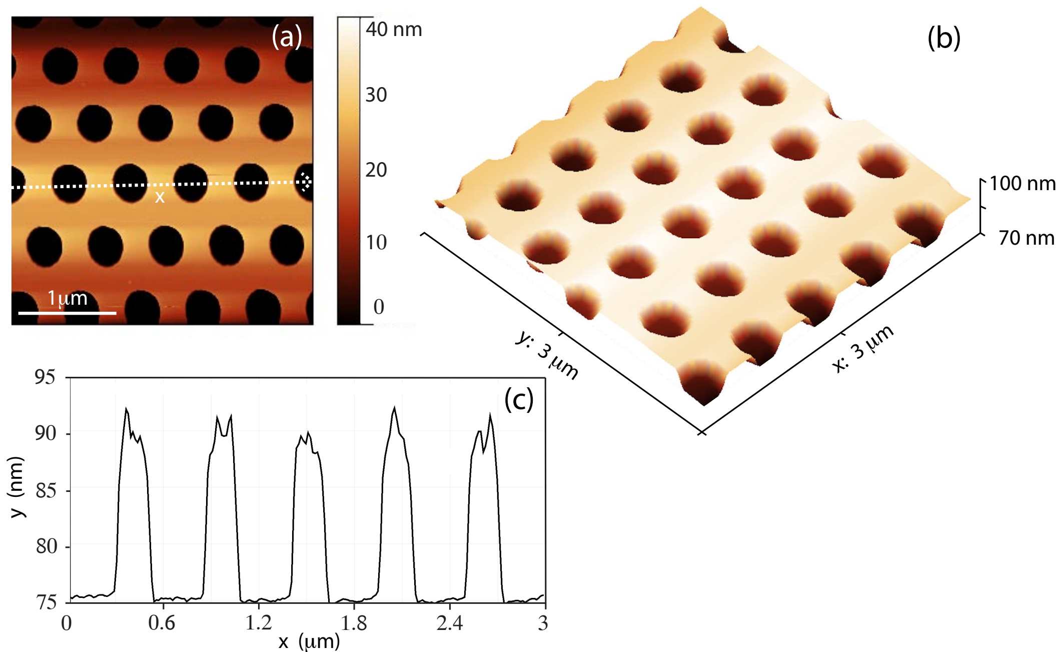

Figure 10: (a) AFM scan of a typical Mo mask after the remover step (scansize is 3x3 μm). (b) 3D representation of the AFM scan in (a). (c) Linear profile of the x-line in (a) showing the depth of the holes and their integrity.

3.1.3 *Mask characterization*

Since the growth process is also time consuming, it is good routine to check the outcome of the mask by means of *atomic force microscopy* (AFM) before inserting the sample into the *molecular beam epitaxy* (MBE) apparatus. This method is preferred to the *scanning electron microscopy* (SEM), which is instead chosen for the morphological characterization of the SAG NCs sample after growth. The electron beam of a SEM surface investigation would in fact break organic compounds of the residual gas in the SEM chamber and release carbon to the surface [63]. Even if the thin carbon layer deposited depends on the

exposure time and residual gas pressure and composition, any concentration can potentially give rise to nucleation sites, during the growth phase, suitable for the growth of parasitic self-organized NCs. An example of AFM characterization of the pre-structured mask is shown in Figure 10.

The masked substrates are now ready to be inserted in the MBE!

It is important to keep in mind that molybdenum masks need do be prepared only some days (maximum $1 - 1,5$ week from the metal deposition) before the growth process. Clean Mo thin films form in fact a surface oxide in air. XPS measurement [64] showed that the oxides of Mo start decomposing at about 500°C in vacuum and this would reduce or even vanish the selectivity properties of the mask during the growth of nanocolumns.

3.2 MBE GROWTH OF SAG NANOCOLUMNS

All the samples presented in this thesis have been grown by molecular beam epitaxy (MBE) in a *Veeco* GENII machine.

Molecular beam epitaxy is an ultra-high vacuum evaporation technique, commonly used for growing single crystal semiconductors. Like conventional thermal evaporation methods, it consists of a vacuum chamber (*Growth* or *Reactor Chamber*), containing internal sources of the materials to be evaporated. However, in such an apparatus, the ultra-high vacuum (UHV) environment ($P_R = 10^{-10}/10^{-11}$ $mbar$) allows the growth of higher quality samples. Nevertheless, this positive aspect is counterbalanced by very low growth rates, in the order of $250 - 500$ $nm/hour$ for GaN layers, when compared with that typical of conventional thermal evaporation techniques, which are in the order of $10 - 100$ $\mu m/hour$.

The high purity environment and extremely fine control over the growth rate result in a number of unique characteristics, such as the ability to create very sharp interfaces, both for intentional dopants and major constituents, or the possibility of using in situ analytical tools, such as reflection high energy electron diffraction (RHEED) and Auger electron spectroscopy (AES), which ease the monitoring of the growth processes.

Another advantage of the MBE is the use of lower growth temperatures than that typically used in conventional thermal evaporation techniques. Since nitride-based compounds are thermodynamically unstable under vacuum conditions, at high temperatures decomposition rates become faster than deposition rates, setting an upper limit to MBE substrate temperatures. Even if lower temperatures would result in a reduction of the surface atom mobility, the UHV environment gives impinging atoms sufficient time to diffuse across the substrate surface and incorporate at appropriate lattice sites. Moreover, the incorporation of impurities from outgassing of hot system components is drastically reduced, as well as the diffusion or redistribution of impurities and

layer components within the structure.

Since the growth of III-nitride materials by means of MBE is the cardinal topic in our research group. In the following paragraphs, only an essential summary of our MBE system will be presented and the attention will be focused on "tricks and tips" to perform an optimized SAG nanocolumn growth. For a complete and exhaustive introduction to the MBE apparatus and growth mechanisms the reader is further addressed to Broxtermann's thesis [17].

3.2.1 *The GENII system*

The GENII system in our MBE laboratory is devoted to the growth of III-nitride materials. Its material crucibles are therefore filled with Ga, In, Al and additionally with Mn and Si, occasionally employed as dopant elements. The geometry of the effusion cells, their internal temperatures and their vapour pressures are the parameters which control the molecular beam fluxes. A radio frequency plasma source (RF-PS) is used to excite the highly pure molecular nitrogen to the plasma state and obtain a low energy beam of atomic nitrogen, which enables the III-nitrides growth process. The possibility to individually open and close the beam flux cells, thanks to a mechanical shutters system, allows a very precise control in the material composition of the growing sample.

The GENII system is composed of three distinct vacuum chambers, which can be kept hermetically isolated one another. The so called *Intro Chamber*, vacuumed with a *baking* and a *turbo pump*, is the chamber with the lower vacuum quality ($P_{intro} = (10^3$ mbar [room pressure] – high 10^{-8} mbar). This is the chamber where the samples are first introduced and where a preliminary outgassing is performed, with the aim to extinguish the remains of water and solvents (baking at $T_{intro} = 200°C$ for 10 min under controlled pressure threshold). When the pressure in the *Intro Chamber* reaches the high 10^{-8} mbar, the samples can be moved into the so called *Buffer Chamber*. In this higher vacuum chamber, which is vacuumed by means of an *ion getter pump*, the samples undergo a further baking step (baking at $T_{buffer} = 600°C$ for 10 min under controlled pressure threshold), after which the pressure is lowered to $P_{buffer} \approx 10^{-9}$ mbar. At this point the sample are sufficiently clean to enter the *Reactor Chamber*, where another *ion getter pump* and an additional *cryo pump* further reduce the pressure to $P_R \approx 10^{-10}$ mbar. At this stage the preliminary procedures for the growth can start.

3.2.2 *Molecular flux calibration*

A crucial parameter for the growth of GaN SAG nanocolumns (NCs) in a MBE apparatus is the Ga/N flux ratio.

As already discussed in Section 2.4.2, it is well known that, in order to grow high quality GaN(0001) layers, the flux ratio between gallium and ionized

nitrogen (N) has to be slightly higher than 1: $\phi_{Ga}/\phi_N > 1$ (Ga-rich conditions). Thanks to the presence of in situ analytical tools, like the reflection high energy electron diffraction (RHEED), the growth conditions relative to the ϕ_{Ga}/ϕ_N ratio, can be checked by monitoring the metal bilayer desorption and adjusted also during the growth process, especially if a looped procedure (alternated GaN growth and desorption steps) is performed [17].

In contrast with planar structures, the growth of SAG NCs can not be monitored by RHEED with high sensitivity, since the presence of a 3D geometry does not allow the direct reflection of the incident electron beam. The beam is instead transmitted through the nanostructure, leading to a spotty pattern of the reciprocal reflexes. For this reason, every time a SAG NCs growth has to take place, it is of utmost importance to calibrate the molecular flux of the Ga effusion cell and consequently adjust the Ga cell temperature (T_{Ga}) to obtain the desired metal flux.

To truthfully reflect the flux values of the growth, it is recommended to perform the flux calibration at the most similar growth conditions. For this reason before starting the calibration the *Cryoshied* has to be filled with liquid nitrogen. This will allow a further reduction of the pressure in the *Reactor Chamber* up to $P_R \approx 5 \cdot 10^{-11}$ mbar. Since the metal mask patterned on the sample for the SAG is highly temperature sensitive, the temperature of the substrate during calibration is kept at a safe temperature of $T_S = 400°C$. The temperature of the Ga cell is generally kept at $T_{Ga_{base}} = 800°C$ (and therefore $T_{Ga_{tip}} = 900°C$), which would be in the flux order necessary for SAG NCs growth. Furthermore, the *ion getter pump* has to be closed, because the pressure present in the *Reactor Chamber* during the growth would damage it. When the pressure in the *Reactor Chamber* is stabilized, the daily flux calibration follows the upcoming steps:

- Note the *Reactor Pressure* (P_R) and the *beam flux monitor pressure* (P_{BFM})
- Open the Ga shutter and wait 6 min for it to stabilize
- Note again the values for P_R and P_{BFM}
- Close the Ga shutter

In the everyday routine the computer program EpiCal is used to calculate from the last P_{BFM} value the temperature at which the Ga cell has to be heated to reach the desired flux. Also the calibration curves recorded in EpiCal has to be readjusted every once in a while, since the conditions of the cells may change over time due to the reduction of the materials levels.

3.2.3 *Stoichiometric flux and growth rate*

The values of gallium and nitrogen fluxes used during the growth of SAG NCs are generally found in literature in *calibrated equivalent growth rate units for* (0001) *GaN layers*.

The conversion to these units is made by determining the gallium stoichiometric flux $\phi_{Ga_{stoich.}}$ during the growth of a (0001) GaN layers sample, but by setting the nitrogen flux $\phi_{N_{layers}}$ equal to that used during the SAG of NCs ($\phi_{N_{layers}} = \phi_{N_{SAG}}$).

The determination of the gallium stoichiometric flux $\phi_{Ga_{stoich.}}$ for GaN layers can be determined *in-situ* during the growth by means of RHEED. When the growth conditions are close to the stoichiometric point (slightly metal rich conditions) it is possible to observe diffracted beam intensity oscillations, which are associated with the growth of single GaN monolayers (MLs) [17].

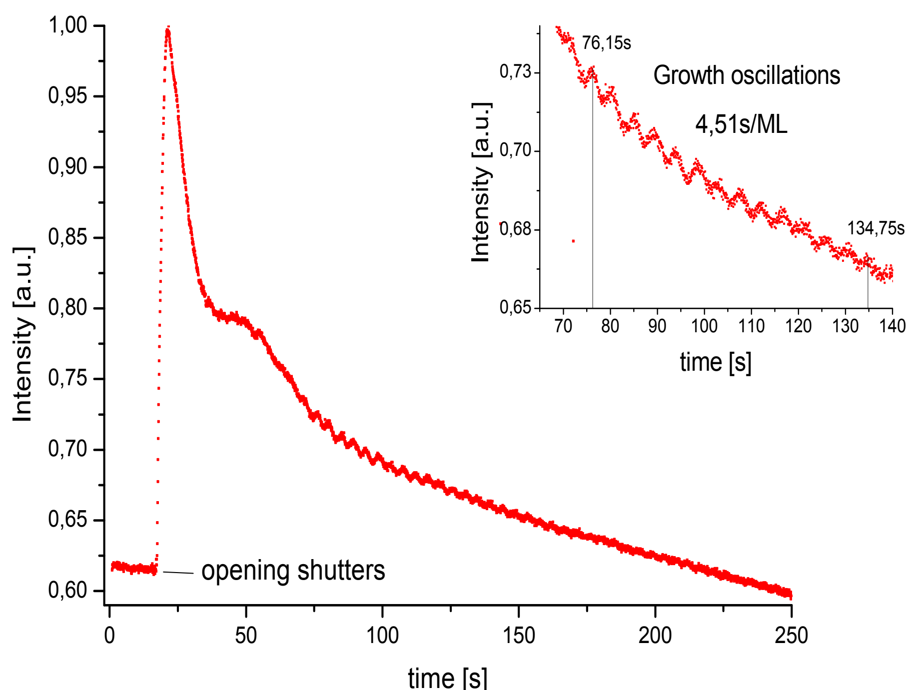

Figure 11: Stoichiometric flux calibration of a GaN layer grown with fixed nitrogen flux of 0.5 sccm and RF power of 300 W. The inset shows an enlargement of the growth oscillations from which a growth rate of 0.22 ML/s or rather 3.45 nm/min could be calculated.

Figure 11 shows an example of RHEED oscillations occurred during the gallium stoichiometric flux calibration of a GaN layer grown with fixed nitrogen flux of 0.5 sccm and RF power at 300 W. From this curve it is possible to extract an average growth rate ($r_{Ga_{stoich.}}$) in ML/s over several oscillations and by knowing the value of the *axial lattice constant* c (see Table 1), convert this stoichiometric growth rate in the conventionally used nm/min units.

Under nominal high nitrogen rich conditions, which are necessary for the growth of nanocolumns, the growth rate has a linear dependency from the sup-

plied gallium flux $\phi_{Ga_{SAG}}$ [17]. Therefore, also for the growth of nanocolumns, a gallium absolute growth rate $r_{Ga_{abs}}$, in terms of calibrated equivalent growth rate units for (0001) GaN layers, can be easily calculated as:

$$r_{Ga_{abs}} = r_{Ga_{stoich.}} \frac{\phi_{Ga_{SAG}}}{\phi_{Ga_{stoich.}}} . \tag{21}$$

3.2.4 *Growth of SAG nanocolumns*

As previously underlined, clean Mo thin films form a surface oxide in air and X-ray photoelectron spectroscopy (XPS) measurements [64] showed that the oxides of Mo start decomposing already at about 500°C. At the same time, it has been observed that also when active nitrogen is introduced into the *Reactor Chamber*, the XPS signal of pure Mo vanishes and a signal of MoN_x arises. This happens already when the nitrogen plasma is switched on and the shutter is still closed, so that when the growth process is initiated by opening the shutters the surface of the masks will already detrimentally consist of a mixture of highly unstable MoO_x and MoN_x. For this reason it is essential to take some expedients before starting with the growth procedure, so to avoid damages of the mask at this stage:

- The nitrogen plasma has to be ignited directly before starting the growth, to avoid as much as possible the formation of MoN_x on the mask surface.

If the growth is performed on Mo masks, the substrate temperature T_S is limited by the thermal stability of the mask itself and will be chosen as a compromise between mask good selectivity (T_S upper limit) and crystal quality (T_S lower limit). Therefore:

- The growth has to be initiated directly after reaching the desired (T_S), to avoid as much as possible the decomposition of the mask.

Taking into account these informations, after the calibration procedures the growth of the samples can start:

- Set the substrate temperature T_S at the growth value (in my case $T_S = 787$°C for the growth of GaN SAG NCs on Mo mask).
- Set the temperature of the gallium cell (T_{Ga}) at the desired growth value (from ϕ_{Ga} calibration).
- Put the substrate in the growth position (facing the materials cells).
- Start the rotation of the substrate (in my case $10\ rpm$), to prevent irregular distributions of the impinging fluxes.
- Check that the water level of the water cooling system is higher than the minimum suggested (this will help keeping the plasma stable during the

whole growth process).
- Set the RF power of the nitrogen in the RFX600A panel at the growth value (for GaN NCs in my case 400 *W*)
- Check that the ion-pump is closed!
- Open the program Nitroscan –> Scan
- Wait until the substrate temperature is around 50°C lower than the desired growth value (in my case $T_S \approx 730$°C)
- Close the valve (VENT) in the N_2 cupboard.
- Open the valve (RUN N_2) in the N2 cupboard (it will let the nitrogen arrive till the screw of the MBE machine).
- Unscrew the valve which allow the nitrogen flux to enter the *Reactor Chamber*.
- Turn on the plasma in the RFX600A panel.
- Adjust the *Reflected Power* to be at 0 (−1 in the digital indicator).
- Set the nitrogen flux at 3 $sccm$ and wait until $\phi_{BMF} \approx 3 \cdot 10^{-5}$ $mbar$ (the plasma need such high pressure to be able to ignite).
- Set the nitrogen flux at 0.3 $sccm$.
- Adjust continuously the *Reflected Power*.
- Wait until the plasma starts. (it should happen at $\phi_{BMF} \approx (10^{-6} - 10^{-7})$ $mbar$).
- When the plasma ignites, adjust again the *Reflected Power* and set the nitrogen flux accordingly to the desired growth value (in my case 1 $sccm$).
- Wait until when T_S reaches the desired temperature for the growth.
- Open the Ga and N shutters.
- Continue ajusting the *Reflected Power* till $\phi_{BMF} \approx 10^{-5}$ $mbar$ (at this point the plasma should stay stable).
- Carry on the growth...

If the plasma does not start it is possible that the pressure needs to be brought up again and then again dropped down. When the growth ended, make all the step back but pay attention to the following points:

- Screw again the valve which bring the nitrogen into the *Reactor Chamber* and at the end use a torque wrench to avoid applying a pressure higher then 30 $inch/cm$.
- Do not open again the ion-pump until when the pressure of the chamber reaches $\phi_R \approx 2 \cdot 10^{-8}$ $mbar$.

The above procedure and conditions are suitable for the growth of GaN SAG NCs on Mo mask. However it should be noted that the reproduction of the reported results could be not straightforward. The local temperature of the substrate often deviates from sample holder to sample holder. Moreover, many parameters depend on the status of the machine at the time of use. In particular, the efficiency of the plasma cell, which reduces over time modifying the growth conditions.

For these reason, it is suggested to take the parameters and growth conditions presented here and in the following chapters as a starting point for future works. Chapter 4 will give a better understanding of the growth processes involved in the molecular beam epitaxy of GaN SAG NCs and gives the reader a feeling about how the parameters should be modified to reach the desired NCs crystal quality.

3.3 CHARACTERIZATION TECHNIQUES

SEM and AFM analysis are generally used for the characterization of NCs morphology. However, when InGaN/GaN heterostructured NCs are grown and indium inclusion within the nanostructures has to be investigated, their characterization is not anymore a trivial matter. The heterogeneous distribution of indium, together with the low In/Ga samples composition, become an analysis issue, due to the insufficient signal/background ratio. For this reason, powerful optical based techniques, like micro-photoluminescence (μ-PL) on NCs arrays or SEM imaging with back-scattered electrons, show in such case strong limitations and the need of high spatial resolution techniques becomes essential. On that account, the samples were investigated by means of high-resolution transmission electron microscopy (HR-TEM), synchrotron hard X-ray nano-probe techniques and, in collaboration with the Otto-von-Güricke University of Magdeburg, Germany, by means of SEM chatodoluminescence (SEM-CL).

Since the use of hard X-ray nano-probe tools is not a conventional characterization technique in our group, the next subsections will be addressed to the theoretical and experimental background, necessary to understand the X-ray spectroscopy results reported in Chapter 6.

3.3.1 *X-ray fluorescence (XRF) and diffraction (XRD)*

X-ray fluorescence (XRF) is one of the most efficient analytical techniques to perform qualitative and quantitative elemental analysis of samples.

When excited by a primary X-ray source, the elements present in a sample generate a set of fluorescent (or secondary) X-rays, which is characteristic of each specific component. This is due to the fact that, when an atom is irradiated with X-ray photons of sufficient energy, it ejects a core electron, leaving a vacancy in its electronic configuration. This vacancy is promptly refilled by an outer shell electron and as a consequence of this transition an X-ray photon is created. If the electron transition happens from an energy level E_i to an energy level E_f, the emitted X-ray will be characterized by an energy equal

to $E_x = E_i - E_f$. Since every atom has a specific electronic configuration, the X-ray spectra are unique and specific of every element.

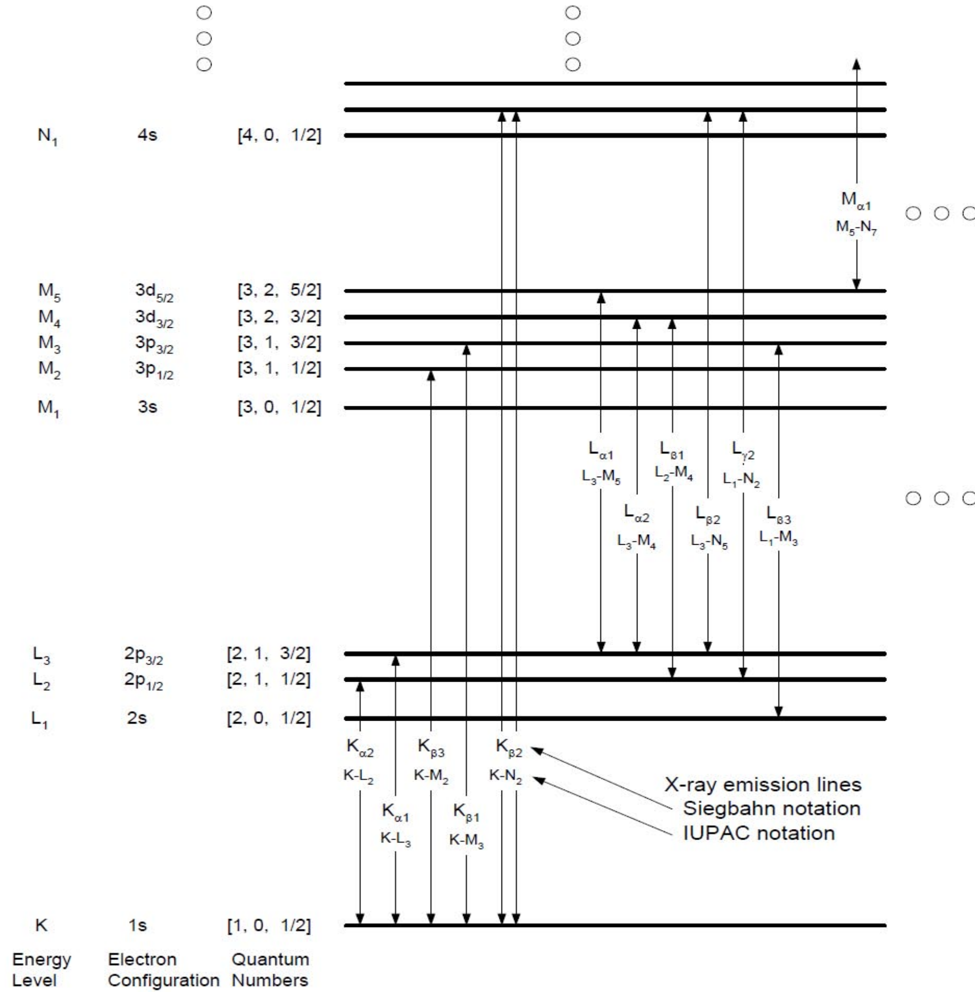

Figure 12: X-ray term diagram showing the allowed transitions determined by the usual selection rules ($\Delta n \geqslant 1, \Delta l = \pm 1$ and $\Delta j = 0, \pm 1$, with $j = l + s$). Figure adapted from Ref. [65].

Figure 12 shows an X-ray term diagram, which introduces the different atomic shells (K, L, M, N, etc.) and sub-shells ($L_{1,2,3}$, $M_{1,2,3,4,5}$, $N_{1,...}$, etc.), with the corresponding electron configurations (1s, 2s, $2p_{1/2}$, etc.) and quantum numbers ($[n = 1, l = 0, j = 1/2]$, etc.). The allowed transitions are determined from the usual selection rules ($\Delta n \geqslant 1, \Delta l = \pm 1$ and $\Delta j = 0, \pm 1$, with $j = l + s$), while the energies transitions specific of each element can be easily found in literature [66].

Furthermore, the intensities of the characteristic X-ray lines of the elements are related to their concentration in the material. However, this relation is not straightforward, because the measured intensity of the emissions lines are influenced by several parameters: the energy spectrum, the intensity of the ex-

citation beam, the geometry between the X-ray source and the sample, the efficiency of the detector, spectral artefacts and matrix effects. However, quantitative analysis software, can address these complexities and perform an estimation of elemental concentrations.

X-ray diffraction (XRD) is a non-destructive investigation technique, whose physical basis is well known in our research group and therefore will not be further recalled in this thesis. However, for an introduction to the XRD, the reader is directed to the bachelor work of Ture Hinrichsen [67].

3.3.2 ID22NI*: a hard X-ray microprobe beamline*

μ-XRF and μ-XRD measurements have been performed at the beamline ID22NI of the European Synchrotron Radiation Facility (ERSF). This beamline is a versatile high-energy X-ray experimental apparatus for the sub-micro scale analysis and is based on a multi technique approach, which allows the simultaneous combination of X-ray absorption, fluorescence and diffraction techniques. The experimental setup, schematically shown in Figure 13 is located at 64 m from the source and is composed of an X-ray focusing Kirkpatrick-Beaz system especially design for this beamline. For an exhaustive description of the X-ray focusing optics the reader is addressed to the references [68, 69, 70].

After focusing, the X-ray nano-beam impinges on the sample and induces luminescence and X-ray fluorescence photons emission, while X-ray diffraction is performed in transmission mode. The experimental setup is characterized by an excitation beam with fixed position and a sample holder XY-nanopositioning stage, which allows a nano spatial resolution scanning of the sample. The spectra are recorded at each raster position of the specimen by means of energy-dispersive detectors: a far-field confocal optical microscope coupled to a spectrometer for the luminescence and a thermally isolated 13-*element Si* solid-state detector located at 50 mm from the sample position for the XRF. XRD patterns are collected in transmission mode by means of a fast readout low noise (FReLoN) 2D-CCD based X-ray detector.

XRF spectra were treated with the analytical software PyMCA (*Python Multi-Channel Analyzer*) [71], which allows to fit the acquired spectra and identify the elemental composition of the samples. PyMCA fitting of spectra is performed after correction of the theoretical line emission energies and energy ratios, by taking into account the experimental parameters (incoming beam energy and flux, detector characteristics, attenuators, detection geometry, peaks shape and matrix composition). The fitting profile used to analyze the average spectrum of a map is applied to each pixel of the outcoming 2D map to calculate the different elemental maps through a batch treatment.

X-ray diffraction patterns were analyzed with the ESRF package Fit2D [72], which allows a detector distortions correction, noise subtraction and calibration of the recorded XRD CCD image. Fit2D performs the calibration by comparing the measurement data with that of a standard reference (Al_2O_3 pow-

der) acquired under the same experimental conditions. The calibrated image is then integrated over the azimuthal angle to generate a standard diffractogram, which can be uploaded in PyMCA. XRF and XRD maps can therefore be studied at the same time.

Specification on the experimental parameters of μ-XRF/XRD measurements will be reported in Chapter 6.

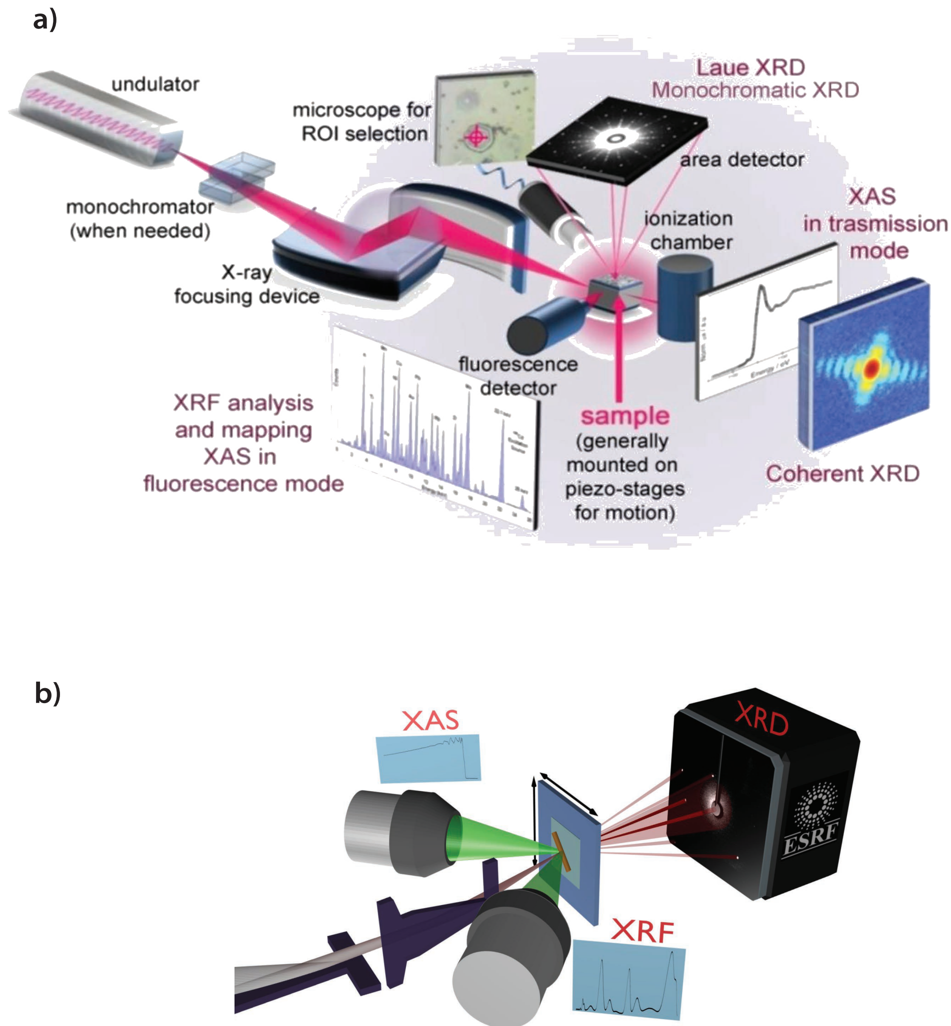

Figure 13: a) Schematic of the multi techniques setup at the nanoimaging station ID22NI of the European Synchrotron Radiation Facility (ESRF). b) Experimental setup during analysis. Figures adapted from Ref. [73].

Part II

RESULTS

4 SELECTIVE AREA GROWTH OF GaN NCs

This chapter provides a more complete understanding of the growth processes involved in the molecular beam epitaxy of SAG GaN NCs. This part of the work can be seen as a follow-up of the studies carried by our former colleague Arne Urban [16, 60]*. The aim is here to investigate the subject-matter of some open questions on growth mechanisms, which turn fundamental for further implementations of InGaN heterostructures on GaN-based NC structures.*

An essential requirement for the manufacture of new generation NCs-based LED technology is, without any doubt, the achievement of fully controlled growth methods for high crystal quality NCs ordered arrays. Contrary to the self-organized growth (SOG), the selective area growth (SAG) allows high control of NCs geometrical parameters, i.e. homogeneous height, diameter and pitch (distance between the edges of the NCs). The optimization of SAG NCs crystal quality would therefore result in the growth of uniform and efficient light emitters.

In the following sections a study of MBE SAG growth mechanisms will be made by taking the ϕ_{Ga}/ϕ_N ratio as control parameter for the growth. First, a sequence of sample grown on Mo mask under the same nominal conditions, with exception of the nominal ϕ_{Ga}/ϕ_N gas flux ratio, will be illustrated and the growth results analyzed. Once the best condition for the growth has been selected, a study on the NCs axial growth as a function of the growth time will be presented. This study, carried out for a set of NCs having different diameters, brings to a more complete explanation of the growth mechanisms occurring along the polar and semi-polar directions over time.
Finally, an overview of the SAG attempts on Ti mask will be presented and its relevance will become apparent in Section 5.2.

Table 3 gives an overview of the relevant nominal growth parameters used during the SAG of GaN NCs samples presented in this chapter.

4.1 GROWTH OF GaN SAG NCs AS A FUNCTION OF THE ϕ_{Ga}/ϕ_N RATIO

As already seen in Chapter 3 the MBE SAG of GaN NCs is a time-consuming process, because the pre-growth sample has to undergo several preparation

Sample	Mask material	T_S (°C)	ϕ_{Ga} (nm/min)	ϕ_N (nm/min)	ϕ_{Ga}/ϕ_N	Growth time (min)
G1625	Mo	787	0.75	6	1/8	180
G1638	Mo	787	0.6	6	1/10	180
G1639	Mo	787	0.5	6	1/12	180
G1641	Mo	787	0.46	6	1/13	180
G1651	Mo	787	0.45	6	1/13.3	135
G1655	Mo	787	0.6	6	1/10	140
G1767	Mo	789	0.6	6	1/10	20
G1768	Mo	789	0.6	6	1/10	40
G1766	Mo	789	0.6	6	1/10	60
G1765	Mo	789	0.6	6	1/10	120
G1756	Mo	789	0.6	6	1/10	180
G1757	Mo	789	0.6	6	1/10	240
G1760	Mo	789	0.6	6	1/10	300

Table 3: Nominal growth parameters used for the SAG of GaN NCs samples relevant for this work (Mo mask).

steps before entering the MBE machine. Moreover, the growth process itself is not always complications free. The nominal parameters set by the grower, such as substrate temperature T_S or gas fluxes ϕ, may not correspond to the same local values experienced by the nanostructures from sample to sample. The conditions of the evaporation cells may change, in fact, over time due to the reduction of the materials levels. Meanwhile, the T_S may change, for instance, depending on the sample holder used for the growth. For these reasons, when starting a sequence of samples, it is recommended to check directly after the first growth (generally a dummy sample) if the desired outcome has been reached. If this is not the case, it is of utmost importance to be able to understand which parameter should be modified (T_S, ϕ_{Ga} or ϕ_N) and how (higher or lower values) for achieving the aimed result. Figure 14 shows bird's eye and top view SEM micrographs of SAG GaN NCs samples relevant to this purpose.

The samples reported in Figure 14 have been grown for 3 hours, following the same procedures and under the same nominal condition, with exception of the gallium flux ϕ_{Ga}. Moreover, the samples have all been grown within a temporal range short enough to assume that no significant variation in the effective parameters took place.

Sample G1625 (Figure 14(a)-(b)) has been grown under a nominal fluxes ratio of $\phi_{Ga}/\phi_N = 1/8$. Even if the selectivity of the growth is of high quality,

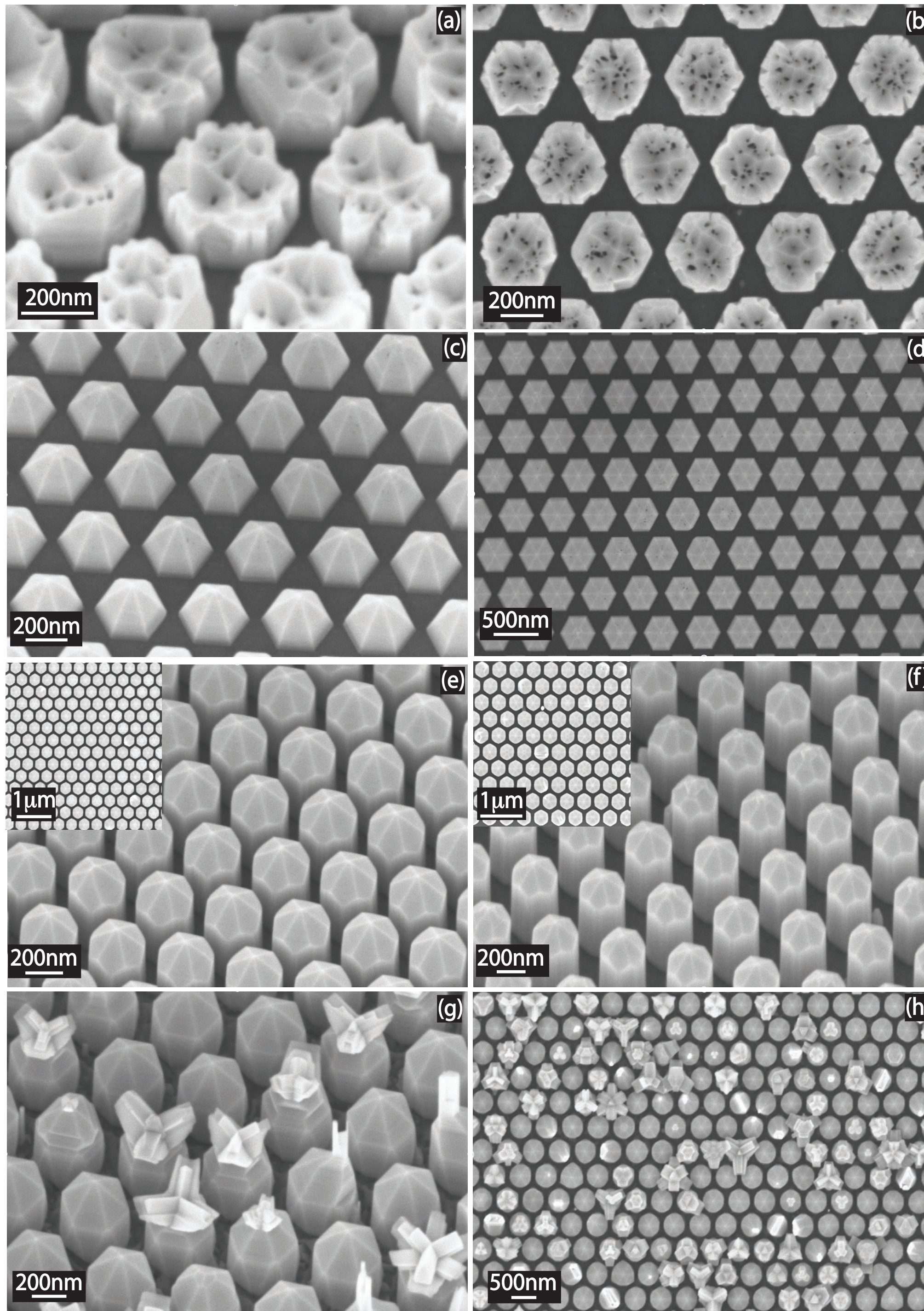

Figure 14: Bird's eye and top view SEM micrographs of SAG GaN NCs after 3h of growth. The growths have been performed at $T_S = 787$ °C and under a $\phi_N = 6$ nm/min. The nominal ϕ_{Ga} has been modified as following: (a)-(b) $\phi_{Ga} = 0{,}75$ nm/min (sample G1625), (c)-(d) $\phi_{Ga} = 0{,}6$ nm/min (sample G1638), (e)-(f) $\phi_{Ga} = 0{,}5$ nm/min (sample G1639) and (g)-(h) $\phi_{Ga} = 0{,}46$ nm/min (sample G1641). All the pictures show the center of the corresponding SAG field.

the SAG nanostructures did not show the formation of semi-polar surfaces, nor a proper development in the axial direction, and the growth of high defective structures detrimentally compromised the crystal quality.

By lowering the nominal fluxes ratio to $\phi_{Ga}/\phi_N = 1/10$, for the growth of sample G1638 (Figure 14(c)-(d)), it has been possible to strongly limit the generation of crystal defects in the SAG nanostructures and observe the complete formation of semi-polar facets. However these structures do not present any further axial growth (hexagonal nanopyramids).

The best growth conditions have been found by further lowering the nominal fluxes ratio to $\phi_{Ga}/\phi_N = 1/12$. Sample G1639 shows homogeneous growth of SAG NCs with large selectivity, high crystal quality and complete formation of the semi-polar facets at the NCs tip. These characteristics could be achieved, within the same run, for NCs grown with different geometrical parameters. As shown in Figure 14(e)-(f), NCs with nominal diameter of $d = 300nm$ have been grown in different patterned fields with nominal pitches of $p = 150nm$ (e) and $p = 250nm$ (f).

A further lowering of the nominal fluxes ratio to $\phi_{Ga}/\phi_N = 1/13$, as shown for sample G1641 in Figure 14(g)-(h), brought once again to a degradation of the NCs crystal quality, with inhomogeneous growth of tripod branches at the NCs tips. An exhaustive study of these unusual structures will be the content of Section 4.1.2.

In this Section, it has been presented how the morphology of SAG GaN NCs may drastically change depending on the ϕ_{Ga}/ϕ_N ratio and how SEM micrographs result a powerful instrument for the evaluation of the growth conditions. If no other issues occur during the growth process (most commonly mask quality related) it is therefore possible to quickly understand, from the NCs morphology of the grown sample, how to adjust the ϕ_{Ga}/ϕ_N ratio to reach the aimed result.

4.1.1 *Control of the* ϕ_{Ga}/ϕ_N *ratio*

After having reported how the morphology of NCs develops as a function of the ϕ_{Ga}/ϕ_N ratio, it is worth notice to introduce what are the principal parameters, which influence and control the ϕ_{Ga}/ϕ_N ratio itself.

First, it is important to point out the difference between the so called *nominal* and *local ratio*:

- The *nominal* ϕ_{Ga}/ϕ_N *ratio* is the mathematical ratio of the fluxes, which is determined from stoichiometric analysis (see Section 3.2.3). For the samples grown in this work it corresponds to the ϕ_{Ga}/ϕ_N values given

in Table 3.

- The *local* ϕ_{Ga}/ϕ_N *ratio* is the effective fluxes ratio locally experienced by a given nanostructure in a given moment of the growth process.

The *local ratio* is therefore the dynamic parameter which control the growth processes. However, it results extremely difficult to quantify, due to the big number of variables from which it depends:

Substrate temperature dependency
The T_S influences the local ϕ_{Ga}/ϕ_N ratio due to Ga adatoms desorption mechanisms on the mask surface. Higher T_S brings to higher desorption of Ga adatoms from the substrate, with consequent lost of Ga contribution to the growth and therefore lower local ϕ_{Ga}/ϕ_N ratio.

Mask quality dependency
If at the growth stage the mask shows any defect or degradation, due for instance to failures in the cleaning procedures or oxidation processes (see e.g. Section 3.1.3 and Section 3.2.4), parasitic nucleation may occur on these defective sites, reducing not only the selectivity of the SAG, but also the Ga adatoms contribution to the growth and therefore the local ϕ_{Ga}/ϕ_N ratio.

Geometry of the lithography
Also the geometry of the lithographic patterned array has a significant influence on the local ϕ_{Ga}/ϕ_N ratio:

- *Pitch dependency*: if the array pitch is larger than two times the Ga adatoms diffusion length on the mask ($2\lambda_m$), no impact on the local ϕ_{Ga}/ϕ_N ratio occurs, because the NCs do not compete for the Ga adatoms contribution (*isolated growth regime*). On the other side, if the array pitch is smaller than $2\lambda_m$, different NCs compete for receiving contribution to the growth from the Ga adatoms diffusing on the mask (*competitive growth regime*) and the local ϕ_{Ga}/ϕ_N ratio results lowered.

- *Diameter dependency*: considering again the λ_m, also the difference in the nanohole diameters may influence the local ϕ_{Ga}/ϕ_N ratio. Bigger diameter holes would in fact receive higher contribution from the mask diffusion of Ga adatoms than smaller diameter holes. However, in view of the smaller mask-free surface, the Ga adatoms density contribution from the mask diffusion results higher for smaller diameters and consistently also the local ϕ_{Ga}/ϕ_N ratio.

Lithography extension dependency
If the lithography is limited to small patterned area (which is the case when using EBL technique), the abrupt end of the lithographic array generates a local ϕ_{Ga}/ϕ_N ratio gradient, which decreases from the frame to the central part

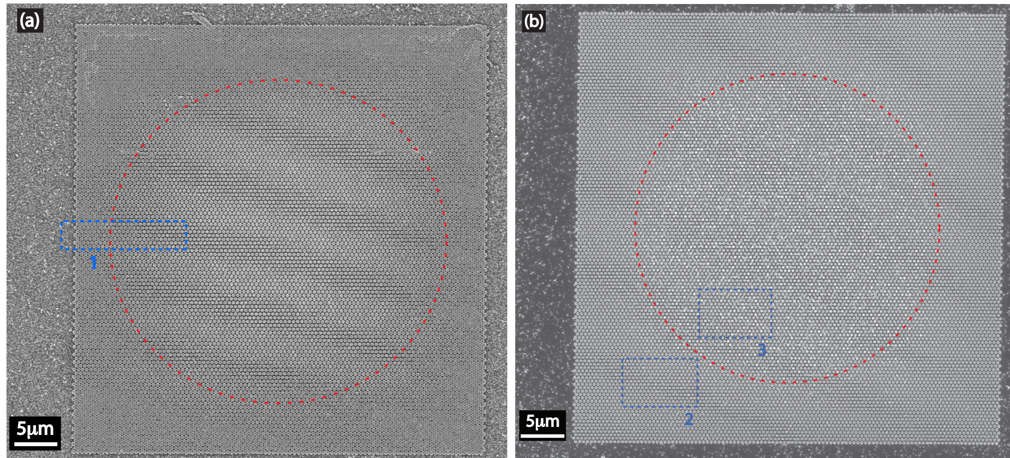

Figure 15: Top view SEM micrographs of SAG GaN grown by MBE under (a) lower (sample G1655: $\phi_{Ga}/\phi_N = 10$) and (b) higher (sample G1651: $\phi_{Ga}/\phi_N = 13.3$) nominal ϕ_{Ga}/ϕ_N ratio. The red dashed circles are a guide to the eyes, which point out a radial symmetry in the SAG growth morphology. The blue dashed rectangles are the zoomed fields of Figure 16 (rectangle 1) and Figure 17 (rectangles 2 and 3).

of the patterned field. This phenomenon is pointed out in Figure 15 to Figure 17. Figure 15 shows the top view SEM micrographs of two samples (G1655 and G1651), grown under different nominal ϕ_{Ga}/ϕ_N ratio on a square field lithography. In both samples it is possible to observe a radial variation of the nanostructures morphology, which has been put in evidence with red dashed circles (guides to the eyes). A closer view of a lateral section (rectangle 1) of sample G1655 is shown in the top and bird's eye view SEM micrographs of Figure 16. In these SEM micrographs, looking from the frame to the central part of the lithography, it is possible to observe a nanostructures morphology variation similar to that of Figure 14(a)-(d). At the same time a closer view of two different fields (rectangle 2 and 3) of sample G1651, shown in Figure 17, puts in evidence a nanostructures morphology variation similar to that of Figure 14(e)-(h). The radial gradient of the local ϕ_{Ga}/ϕ_N ratio can be explained by considering λ_m in a competitive growth regime. The NCs growing close to the lithographic field frames, may in fact enjoy from an higher contribution of Ga adatoms diffusion on the mask, than the NCs growing in the center of the patterned field. This explanation is consistent with the growth of SAG samples with lithographic pitches large enough to allow NCs isolated growth regime (not shown) and where this gradient effect is not present.

NCs height dependency

As it will be discussed in details in the following Section 4.2, after nucleation the SAG of NCs reach a stage of polar and semi-polar axial growth. At this point the growth rate is not driven anymore only by the direct impingement of Ga and N atoms on the NCs tip and by the Ga adatoms diffusion on the mask, but also by the Ga adatoms diffusion on the NCs sidewalls (λ_f) towards

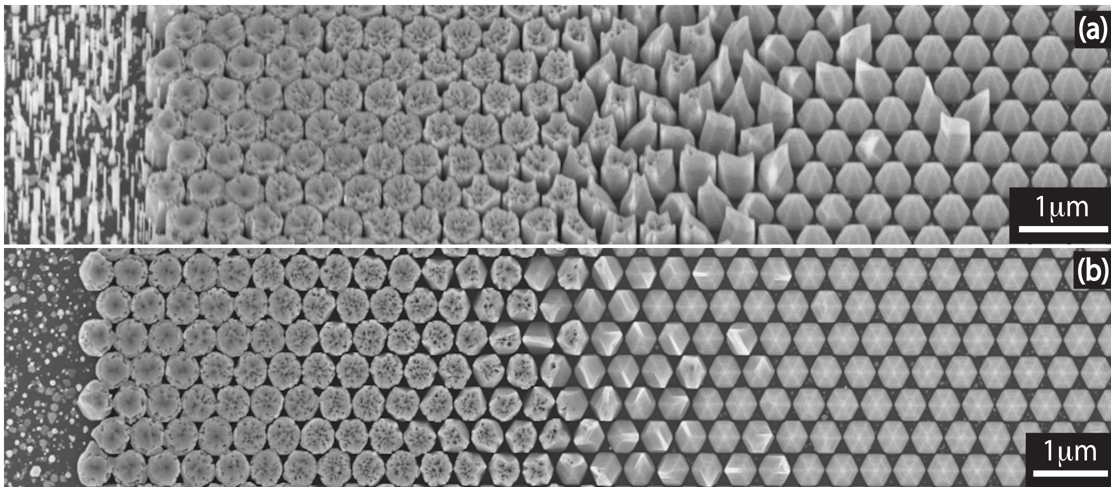

Figure 16: Top (a) and bird's eye (b) view of the SAG GaN NCs delimited by the blue dashed rectangle 1 of Figure 15(a). From the left to the right it is possible to observe the SOG of GaN NCs on the mask and a variation of SAG GaN NCs morphology (as the like in Figure 14(a)-(d)) due to a geometry induced radial gradient in the local ϕ_{Ga}/ϕ_N ratio.

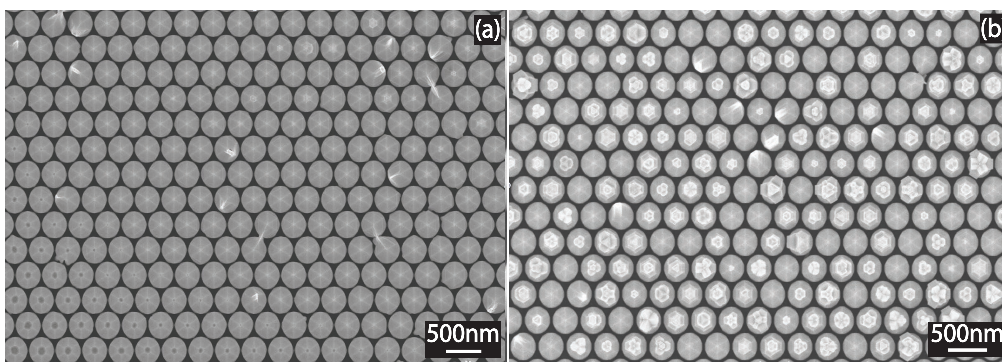

Figure 17: Top view of the SAG GaN NCs fields pointed out by the blue dashed rectangles 2 (a) and 3 (b) in Figure 15(b). From (a) to (b) it is possible to observe a variation in the NCs morphology (as the like in Figure 14(e)-(h)) due to a geometry induced radial gradient in the local ϕ_{Ga}/ϕ_N ratio. Furthermore, in (a) it is also evident how the NCs growth rate has been affected by the geometry induced variation in ϕ_{Ga}/ϕ_N ratio, since in the bottom-left part of (a), differently from the upper-right part of (a), the NCs tips are still not closed.

the NCs tip. However, during the axial growth the contribution given by the Ga adatoms diffusion on the mask constantly decreases, until completely vanishing when $h >> \lambda_f$, i.e. when the lateral sidewalls of NCs reach a height (h) higher than the Ga adatoms diffusion length on the NCs sidewalls themselves (λ_f). As a results, since $\lambda_f << \lambda_m$, the local ϕ_{Ga}/ϕ_N ratio, experienced at the NCs tip, results dynamically lowered with the axial growth (for $h << \lambda_f$) and stabilized again for $h >> \lambda_f$.

Shadowing effect dependency
Due to the inclination of the Ga effusion cell by $\alpha = 33°$ with respect to the substrate normal, SAG NCs grown by MBE may experience a screen effect, from the impinging beams, on the lower part of the NC. This effect is of noticeable importance for high density NCs arrays, i.e. for $d >> p$, where it brings to a reduction of the local ϕ_{Ga}/ϕ_N ratio experienced at the NCs tip.

Nominal ϕ_{Ga}/ϕ_N ratio dependency
It is trivial to understand that the local ϕ_{Ga}/ϕ_N ratio is directly proportional to the nominal one. However, it is important to stress this dependency, since the nominal ϕ_{Ga}/ϕ_N ratio is the sole value which can be experimentally quantified.

4.1.2 *Deviations from the SAG GaN NCs pencil-like structure*

This Section will focus on the analysis of the most common morphological deviations, from the classical pencil-like structure, which SAG NCs may develop throughout the growth.

In Section 4.1 it has been pointed out how the morphology of SAG GaN NCs may vary depending on the ϕ_{Ga}/ϕ_N ratio. Particular attention is now given to the branching mechanism, which occurs at the NCs tip for ϕ_{Ga}/ϕ_N ratio lower than that supporting the growth of pencil-like morphologies (see e.g. Figure 14(g)-(h)). High-resolution transmission electron microscopy (HR-TEM) of these structures has shown that the growth of branches is induced by the formation of tetrahedron-like ZB GaN on top of the NCs. These kind of structures are schematized, for making easier the understanding, in Figure 18.

The uncommon growth of pure ZB GaN areas at the NCs tip, can be rationalized by taking into account the low ϕ_{Ga}/ϕ_N ratio under which it takes place. Under very low ϕ_{Ga}/ϕ_N ratio, the Ga atoms impinging the NCs are directly incorporated into the structures, due to the high N atoms availability. Ga diffusion mobility is therefore drastically dumped and incorporation takes place before Ga atoms may reach appropriate lattice sites. This brings to a fast degradation of the crystal quality and boosts the appearance of crystal structure twinning mechanisms.

Figure 19(a) shows a transmission electron microscopy (TEM) image of a representative SAG GaN NC, exhibiting the formation of a lateral branch on its tip (red dotted square). Figure 19(b) is a high-resolution TEM of the red

dotted square area in Figure 19(a). From the HR-TEM image it is possible to see not only the highly degraded crystal structure (defective WZ structure), but also how even a small part of pure ZB can act as a seed for branching.

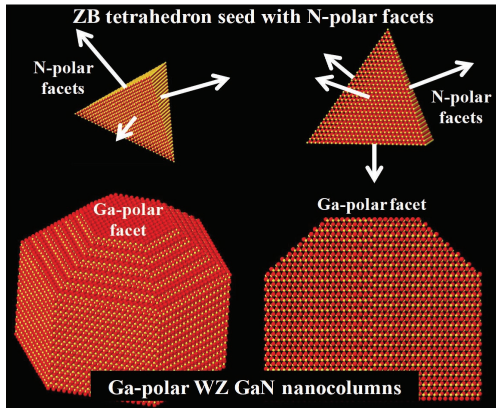

Figure 18: Twinning mechanisms, due to low ϕ_{Ga}/ϕ_N ratio growth conditions, lead to the formation of tetrahedron-like ZB GaN on top of the NCs, which provides three free N-polar {111} facets and acts as a seed for the growth of branches.

Due to the frenetic incorporation, also the growth rate of the nanostructures results increased. This phenomenon can be easily seen in samples suffering from pattern induced local ϕ_{Ga}/ϕ_N ratio gradient. In Figure 17(a), for instance, the NCs grown under higher local ϕ_{Ga}/ϕ_N ratio, on the bottom-left part of the array, show semi-polar tips which are still not completely formed. Differently, the NCs grown under lower local ϕ_{Ga}/ϕ_N ratio, on the central part of the array (up-right part of the image) show already complete, but more defective, semi-polar tips, in accordance with an higher growth rate.

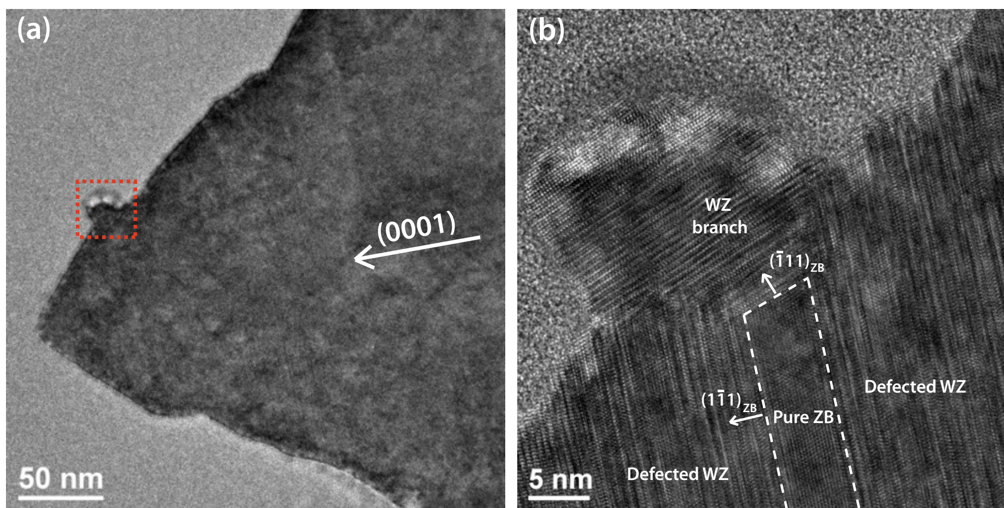

Figure 19: (a) TEM nanograph of a representative SAG GaN NCs tip, exhibiting the formation of a lateral branch. (b) HR-TEM nanograph of the red dashed square in (a), showing high degradation of the NC tip crystal structure with inclusion of pure ZB. It is also evident how the ZB insertion acts as a seed for branching. The experiments were done by R. Zamani, Georg-August University Göttingen.

Another confirmation for the branching mechanism comes from the attempt to gradually increase the ϕ_{Ga} during the SAG, with the aim to reduce the effective growth rate and keep the WZ crystal growth.

The samples (not shown) resulted less affected by tetrahedrons formation. SOG nucleation appeared boosted outside the lithographic patterns, but suppressed inside the SAG array due to shadowing effect.

Figure 20 shows another phenomenon which is often observed after the growth of SAG GaN NCs. The presence of thin GaN N-polar NCs coming out from the SAG Ga-polar NCs tip can be explained by considering the radial growth of SAG NCs. Once the Ga diffusion on the mask does not contribute anymore to the NCs axial growth ($h >> \lambda_f$), the Ga surplus at the NCs bottom induces a radial growth of the nanostructures. As shown in Figure 25(b), if a SOG NC nucleates close to a SAG NC and if the growth time is long enough to induce radial growth mechanisms, the SOG NC may, after a while, be incorporated within the SAG NC structure itself, giving rise to deformations of the SAG NCs morphology.

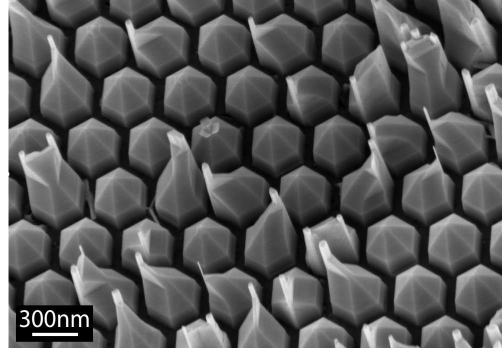

Figure 20: Bird's view SEM micrograph showing the inclusion of SOG NCs within the SAG structures.

4.2 GROWTH OF GaN SAG NCs AS A FUNCTION OF TIME

This Section introduces a study on MBE SAG NCs axial growth as a function of the growth time. With this purpose, Figure 21 shows the top view SEM micrographs of a set of SAG GaN NCs samples, grown on Mo masks having the same lithographic nanohole pattern (nanohole diameter from the right to the left: $d = 100nm$, $200nm$, $300nm$, $500nm$, $800nm$ and $1000nm$), which has been designed to allow the SAG of GaN NCs under *isolated growth regime* (see Section 4.1.1). For all samples, the growth has been performed under the same nominal conditions of ϕ_{Ga} and ϕ_N impinging fluxes and substrate temperature T_S (the best conditions selected in Section 4.1), whereas the growth time has been varied by $t = 20min$ (a), $40min$ (b), $60min$ (c), $120min$ (d), $180min$ (e), $240min$ (f) and $300min$ (g) (see also Table 3). Bird's eye view SEM micrographs of the same samples (with exception of the $t = 20min$, which does not show noticeable axial growth) are shown in Figure 22.

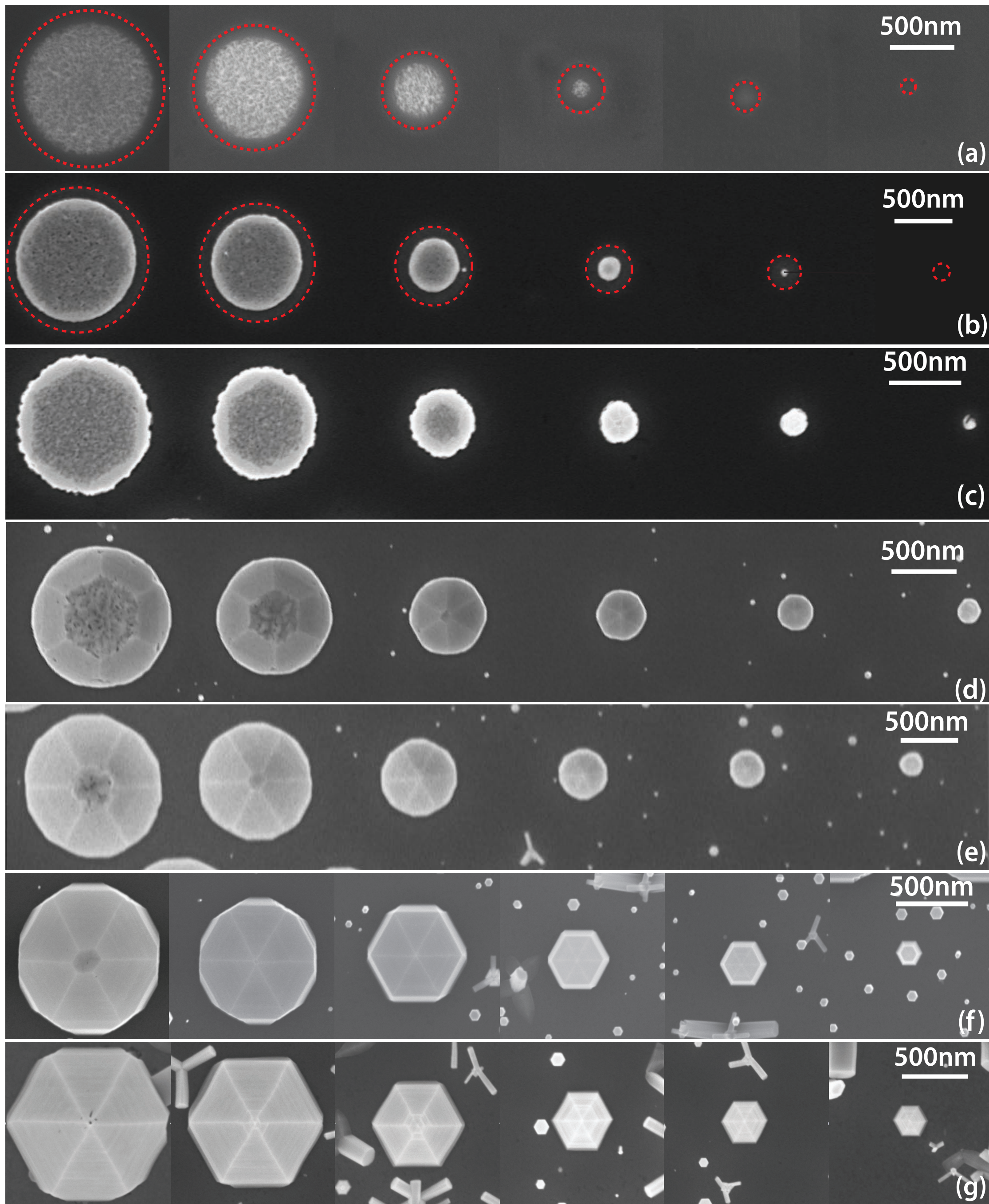

Figure 21: Top-view SEM micrographs of SAG GaN NCs with diameters of 100 nm, 200 nm, 300 nm, 500 nm, 800 nm and 1 µm, from the right to the left. The growth times are $t = 20, 40, 60, 120, 180, 240$ and 300 min for (a)-(g) respectively. Samples G1767, G1768, G1766, G1765, G1756, G1757 and G1760 for (a)-(g) respectively. The red dashed circles of are guides to the eyes indicating the edges of the lithographed nanoholes, which are not yet completely filled by the NCs in the first stages of growth.

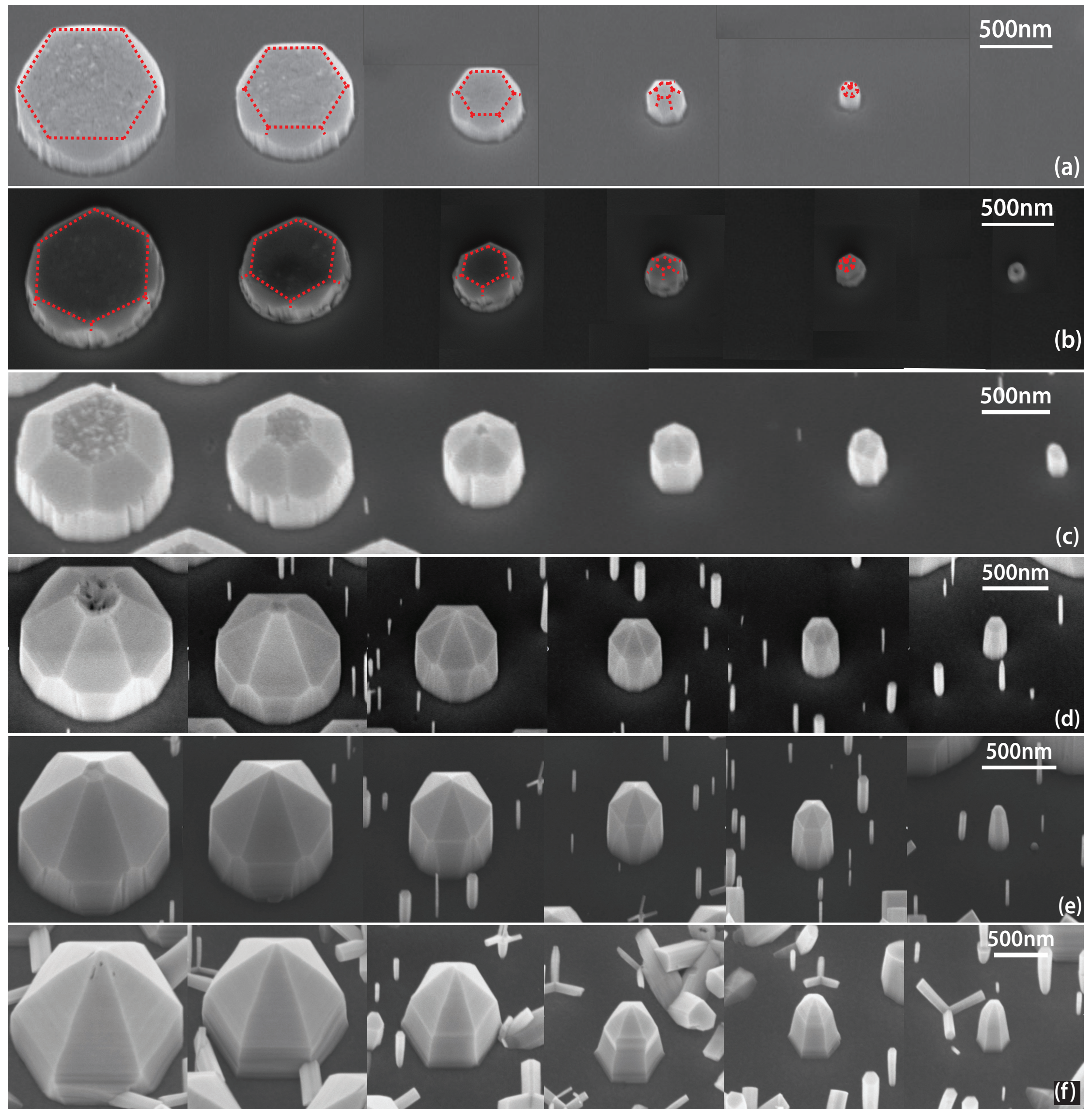

Figure 22: Bird's eye view SEM micrographs of SAG GaN NCs with diameters of 100 nm, 200 nm, 300 nm, 500 nm, 800 nm and 1 μm, from the right to the left. The growth times are $t = 40, 60, 120, 180, 240$ and 300 min for (a)-(f) respectively. Samples G1768, G1766, G1765, G1756, G1757 and G1760 for (a)-(f) respectively.

A description of what has been observed during this investigation is reported hereafter, while a more comprehensive discussion of the results will be the focus of Section 4.4.

Nucleation and coalescence as a function of the nanoholes diameter:

At the beginning of the growth process (Figure 21(a) and (b)), the SAG conditions support Ga adatoms diffusion on the Mo mask and GaN nucleation takes place exclusively within the lithographic nanoholes. GaN nuclei avoid the edges and start forming in the nanoholes center. The red dashed circles are guides to the eyes indicating the edges of the lithographic nanoholes, and pointing out the nucleation free surfaces close to the nanohole sides.

Also the incubation time before nucleation seems to depend on the nanohole dimensions. After a growth time of $t = 20min$ (a) the four biggest holes show nucleation and coalescence, while the $d = 200nm$ and $100nm$ nanoholes are still nucleation-free. After $t = 40min$ growth time (b), the $d = 100nm$ nanohole results to be the last one still nucleation-free, while the nanostructures growing into the bigger holes already show onsets of semi-polar facets. This phenomenon can be better observed in Figure 22(a), where dashed red lines have been added as guides to the eye, for pointing out the semi-polar facets formation.

After a growth time of $t = 60min$ (Figure 21(c) and Figure 22(b)) the $d = 100nm$ nanohole NC is eventually grown and its semi-polar tip already closed, while the other NCs show the ongoing development of their semi-polar facets.

Evolution of the NCs crystal shape as a function of the growth time:

Once the nucleation is occurred and the coalescence filled up the lithographic nanoholes (transition from Figure 21(b) to (c)), the NCs side walls show an irregular roundish shape, which does not allow the identification of any non-polar plane preference. In a following step (transition from (c) to (d)), due to the beginning of an additional radial growth, the side walls shape smooths down and, especially for the smaller diameters, a mixing of the two most energetically favorable non-polar surfaces appears (namely the *m-plane* and the *a-plane* facets). This phenomenon becomes even more visible in a further growth stage (transition from (d) to (e)), where also the bigger diameters start disclosing dodecagonal shapes.

Carrying on the growth (transition from (e) to (f)), the dodecagonal shape of the bigger diameters NCs became sharper. At the same time, for the smaller diameter NCs the radial growth supports a faster growth of m-planes surfaces, leading the NCs shape to a changeover from dodecagonal to almost hexagonal shape. The last reported growth step (transition from (f) to (g)) confirms the

previous observation and shows the tendency, also for the bigger diameter NCs, to the hexagonal shape conversion.

This phenomenon seems to be correlated with the growth of the NCs tip. In fact, all NCs show the transition to the hexagonal shape on a growth step directly after the closure of the semi-polar facets tip. This phenomenon is easier to point out for NCs with large diameters. Taking into account, for instance, the NCs with nominal diameter of $d = 500\text{nm}$ and $d = 800\text{nm}$, it is possible to see that their tips are still open in (d)-(e) and close in (e)-(f) respectively. In a further growth steps (f)-(g) both NCs show a shift to the hexagonal shape. It is believed that also the NC with nominal diameter of $d = 1000\text{nm}$, which follows the same developments in (f)-(g), would further evolve to an hexagonal shape for longer growth times.

Formation, development and completion of the NCs tips as a function of the nanoholes radius and the growth time:

With the aim of analyzing the influence of the tip growth on the total height of the NCs, a graphical representation of the NCs height as a function of the growth time is reported, for each NCs diameter, in Figure 24. Here the different markers represent the NCs tip height h_2 (red dots), the NCs prism height h_1 (black squares) and the NCs diameter d (blue triangles). For a better understanding of these quantities, a schematic drawing has been added in Figure 23.

A sampling of twenty NCs, for each NCs diameter and growth time, has been taken into account for determining the values of heights h_1 and h_2 and diameters d. The error bars are given by the standard deviation.

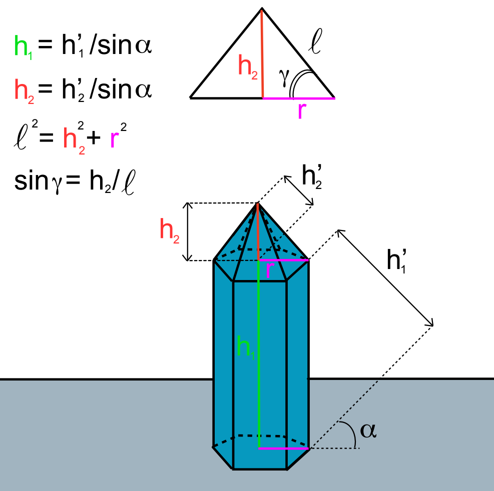

Figure 23: Scheme representing the graphical results of Figure 24, where the total height of the NC is given by the sum of the height of the cylindrical body h_1 and the pyramidal tip h_2. Here, r is the NCs radius, while h_1' and h_2' are respectively h_1 and h_2 projections on a plane inclined of an angle α, with respect to the NCs c-plane.

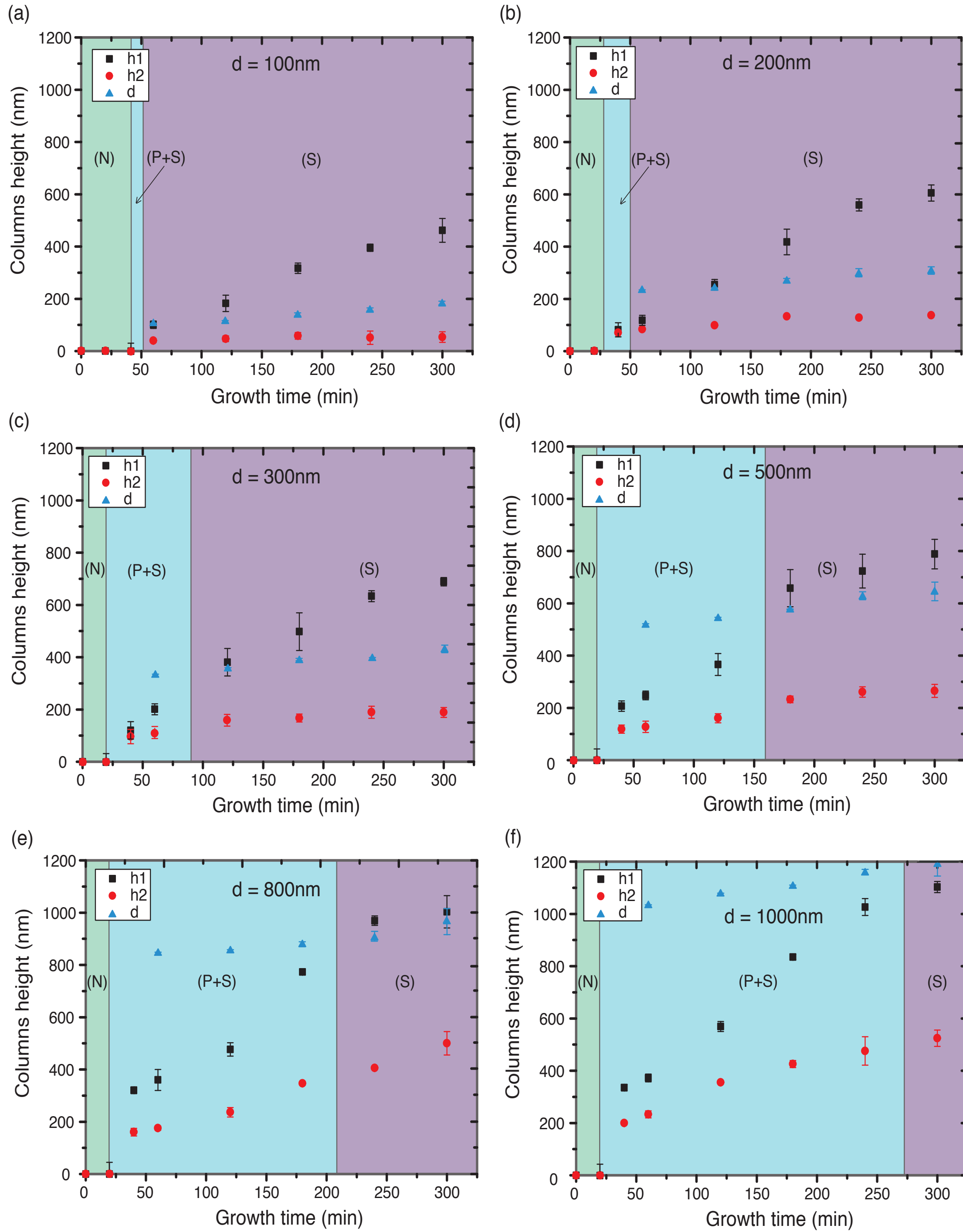

Figure 24: Axial growth as a function of the growth time for SAG GaN NCs with diameters of 100 nm (a), 200 nm (b), 300 nm (c), 500 nm (d), 800 nm (e) and 1 μm (f). The black and the red points refer respectively to the height of h_1 and h_2 (see Figure 23). Three different growth regimes can be identified: a nucleation phase in green (N), a mixed growth rate of polar & semi-polar planes in pale blue (P + S) and a lower semi-polar growth rate in violet (S).

Three different growth regimes can be pointed out in Figure 24:

- A *nucleation regime* (N), with green background color, at the beginning of the growth, where nucleation processes, coalescence and filling of the nanoholes take place.
- A *polar & semi-polar regime* $(P+S)$, with blue background color, showing a total height growth rates given by the combination of both growth contributions $(h_1 + h_2)$.
- A *semi-polar regime* (S), with violet background color, in which the total height growth rate trend decreases, due to the closure of the semi-polar facets at the NCs tip, which ends the growth contribution from h_2.

NCs radial growth as a function of the growth time:

Considering the values of the NCs diameter showed in Figure 24, a linear increment in the NCs radial growth is observed, as a function of the growth time, for the whole set of NCs. In Figure 24(d)-(e) a potential speed up of the radial growth rate may be spotted during the S growth regime. However, considering the error bars, no clear influence of the tip growth on the NCs radial growth seems to be noticeable during the transition from the $(P+S)$ to the S growth regime. The uncertainty in the measurements of the last two points, is given by the appearance of a tapering of the NCs prim shape (see Figure 24(f)).

The absolute values of the radial growth rate, in terms of nm/min, seem thus to be the same for the whole set of NCs. From this observation it is possible to state that, considering the different size of the nanoholes, the relative radial growth rate of the NCs having larger diameters is slower than that of the smaller diameter ones.

For the sake of clarity, the values of NCs diameters have been reported from the moment in which the filling of the corresponding nanoholes has been completed (i.e. from $60min$ growth), as for excluding the contribution of residual coalescence effects from the measured radial growth rate. The SAG NCs growth process is also schematized in Figure 25(1a)-(3a.1).

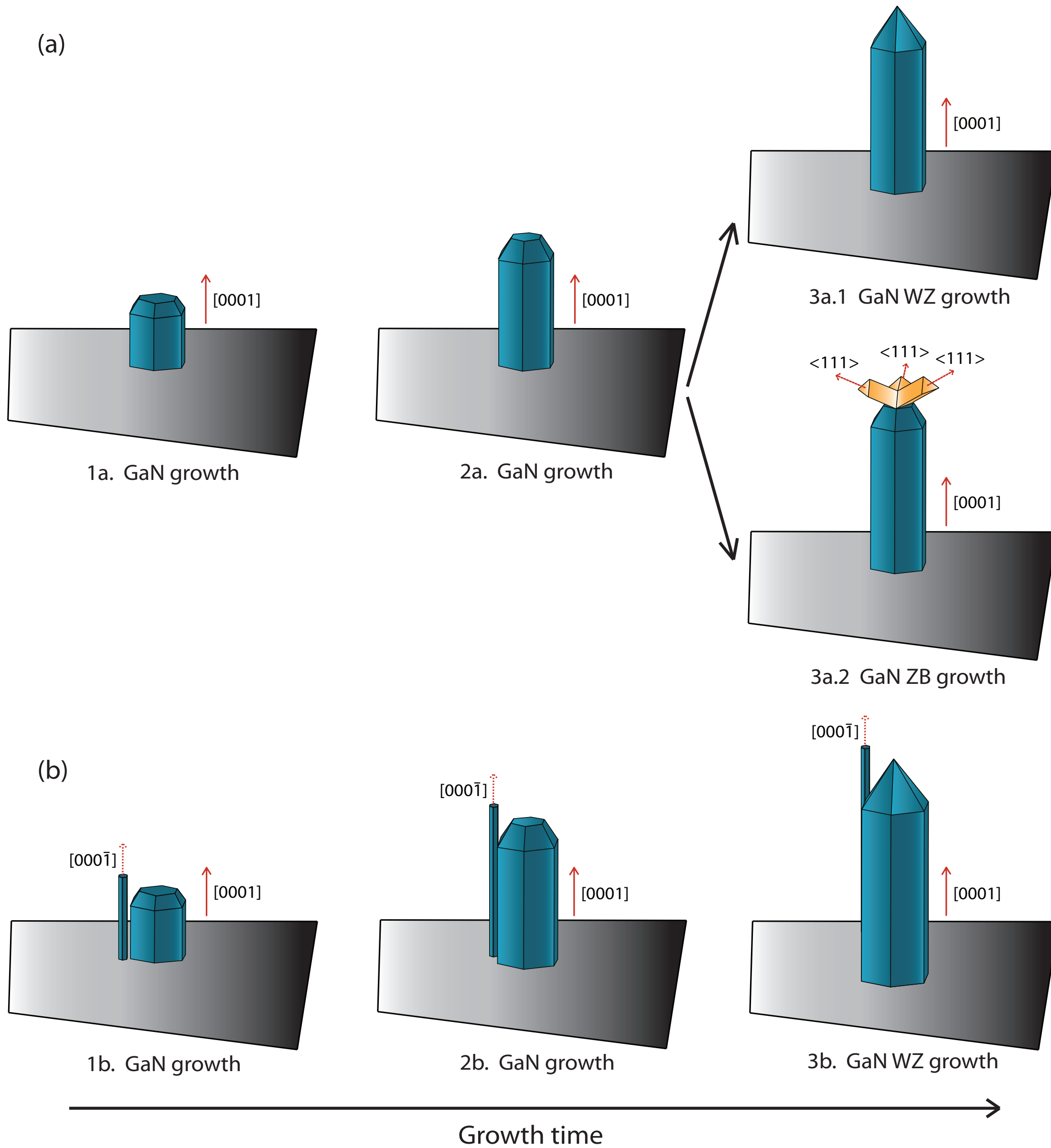

Figure 25: Schematic representation of SAG GaN NCs growth process. (a) At the beginning of the growth process, the NC axial growth benefits from the Ga adatoms contribution from mask diffusion (1a). Once the NC height is higher than the Ga adatoms diffusion length on the NC sides, the diffusion on the mask does not contribute anymore to the NC axial growth and a lowering of the axial growth rate is observed (2a). At this point, if the local ϕ_{Ga}/ϕ_N ratio is still enough high to satisfy the conditions for the growth of good quality GaN, the tip of the NC closes and the axial growth can be attained only with the growth of the semi-polar surfaces at the NC tip. Due to the lower rate which characterizes the growth along the semi-polar directions, a further reduction of the NC axial growth rate takes place (3a.1). If the ϕ_{Ga}/ϕ_N ratio is too low, the possibility of stacking faults formation increases. These stacking faults acts as a seed for the growth of GaN ZB along the $< 111 >$ direction (3a.2), with consequent formation of a ZB tetrahedron (see Figure 18 and Figure 14(e)-(h)). (b) Once the diffusion on the mask is no more contributing to the axial growth, it supports the NC radial growth. If a SOG NC is growing enough close to the SAG NC, after a certain amount of growth time, it will be incorporate within the SAG structure (3b) as also shown in Figure 20.

4.3 GROWTH OF GaN SAG NANOPYRAMIDS

This section is meant to give an overview on similar growth attempts of GaN nanostructures, under SAG conditions, using Ti nanoholes masks.

Ti mask is an alternative choice to the Mo mask, which enable the growth at remarkable higher temperatures. Therefore, it has been considered to improve the crystal quality of GaN SAG NCs.

When changing mask material for the SAG, it is important to tune the growth conditions in an appropriate way. As starting point for the growth, the experimental conditions found in literature [74, 75] have been considered and adjusted, in conformity with the characteristics of our GENII MBE system.

After several attempts with systematic variation of the growth conditions, a good selectivity of GaN nanostructures could be achieved, but no axial growth has been observed resulting on the SAG of GaN Nanopyramids (NPs).

Figure 26 shows a Ti mask SAG of GaN NPs example. The growth has been performed at $T_S = 940°C$ and under nominal $\phi_N = 9\ nm/min$ and $\phi_{Ga} = 5,2\ nm/min$ conditions (for preventing degradations the Ti mask underwent a nitridation step previous to growth [75]).

The nominal $\phi_{Ga}/\phi_N \approx 0,58$ ratio is very high as compared with that typically supplied during the SAG on Mo masks, but it has to be considered that the remarkable higher T_S, used on Ti masks, boosts the Ga adatoms desorption probability on the mask surface.

For these specific growth conditions, the Ga adatoms desorption probability $1/\tau_{des}$ may be estimated as following:

$$\frac{1}{\tau_{des}} = \frac{dN_{Ga_{des}}}{dt} \approx e^{\frac{\Delta E}{kT}}, \tag{22}$$

where $N_{Ga_{des}}/dt$ is the fraction of Ga atoms desorbing per unit of time, ΔE is the lowest activation energy for Ga desorption ($\Delta E = 3.1 \pm 0.2\ eV$ [76]), k is the Boltzmann's constant and T is the surface temperature of the mask during growth.

Therefore, assuming $T_{Ti} = 940°C$ and $T_{Mo} = 789°C$, the desorption probabilities ratio between the two growth conditions results to be:

$$\frac{e^{\frac{\Delta E}{kT_{Mo}}}}{e^{\frac{\Delta E}{kT_{Ti}}}} \approx 60. \tag{23}$$

Thus, the Ga desorption probability on Ti mask is around 60 times higher than that occurring at T_S typically used on Mo mask, which implies a very low local ϕ_{Ga}/ϕ_N ratio.

However, with the aim of supporting axial growth, several growths with different conditions have been carried out. The T_S has been lowered down to $T_S = 900°C$, corresponding to a desorption probability of 20 times higher than that taking place at T_S typically used on Mo mask. Under such conditions, the local ϕ_{Ga}/ϕ_N ratio becomes comparable with the one experienced by the

SAG NCs on Mo mask of Figure 14(g)-(h). Nevertheless, the growth results on Ti mask always showed SAG of GaN NPs.

The mask of the sample shown in Figure 26 was designed to include several lithographic fields consisting of different nanoholes diameters and pitches. The growth has been performed for $t = 45min$, which allowed the complete formation of NPs grown on the $d = 300nm$ field Figure 26(a)-(b), but resulted not sufficient to allow the complete formation of the NPs grown on the $d = 500nm$ (c)-(d) and the $d = 800nm$ fields (e)-(f). It is therefore possible to observe in the same sample different NPs growth moments. What stands out from Figure 26 is the outstanding crystal quality of the structures, with very homogeneous morphology and absence of staking faults (SFs) formation on the semi-polar tip. This observation could be confirmed also by HR-TEM analysis (not shown). The higher crystal quality of these structures as compared with that of NCs grown on Mo mask, is considered one of the reason which allows the growth of homogeneous InGaN/GaN heterostructures on NPs structures and will be the focus of Section 5.2.

4.4 RESULTS DISCUSSION

In Section 4.1, the morphological evolution of SAG GaN NCs has been investigated as a function of the ϕ_{Ga}/ϕ_N ratio. It is well known that NCs growth conditions require low nominal ϕ_{Ga}/ϕ_N ratios (nominal very nitrogen rich conditions), however it is astonishing to observe how even small variation in the ϕ_{Ga}/ϕ_N ratio may drive the growth to very different morphological shapes (see Figure 14).

Li *et al.* [77] recently reported a computational study on wurtzitic crystal shapes of GaN NCs, which uses a generalization of the Wulff's construction under different growth conditions. They found the important quantity governing the 3D Wulff crystal shape to be the energy corresponding to the crystal radius along the polar axis and show how it continuously varies from Ga-rich to N-rich conditions. In this way, they predict the crystal to form a complete pyramid under extremely high Ga-rich conditions and to assume the shape of a truncated pyramid, by moving in the N-richer direction. Going further N-richer the crystal shape eventually turn into another pyramid formed by $\{1\bar{1}02\}$ facets based on a dodecagonal prism, with side walls consisting of both non-polar facets (namely *m-* and *a-plane*). These predictions are in good agreement with the experimental results of Figure 14, even if the appearance of two non-polar planes on the NCs wall sides becomes more evident by considering the results of Figure 21 and Figure 22.

In Section 4.2, the MBE SAG of several GaN NCs samples, as a function of the growth time and the nanoholes diameter, has been reported. SAG GaN NCs formation and growth stages have been experimentally observed and

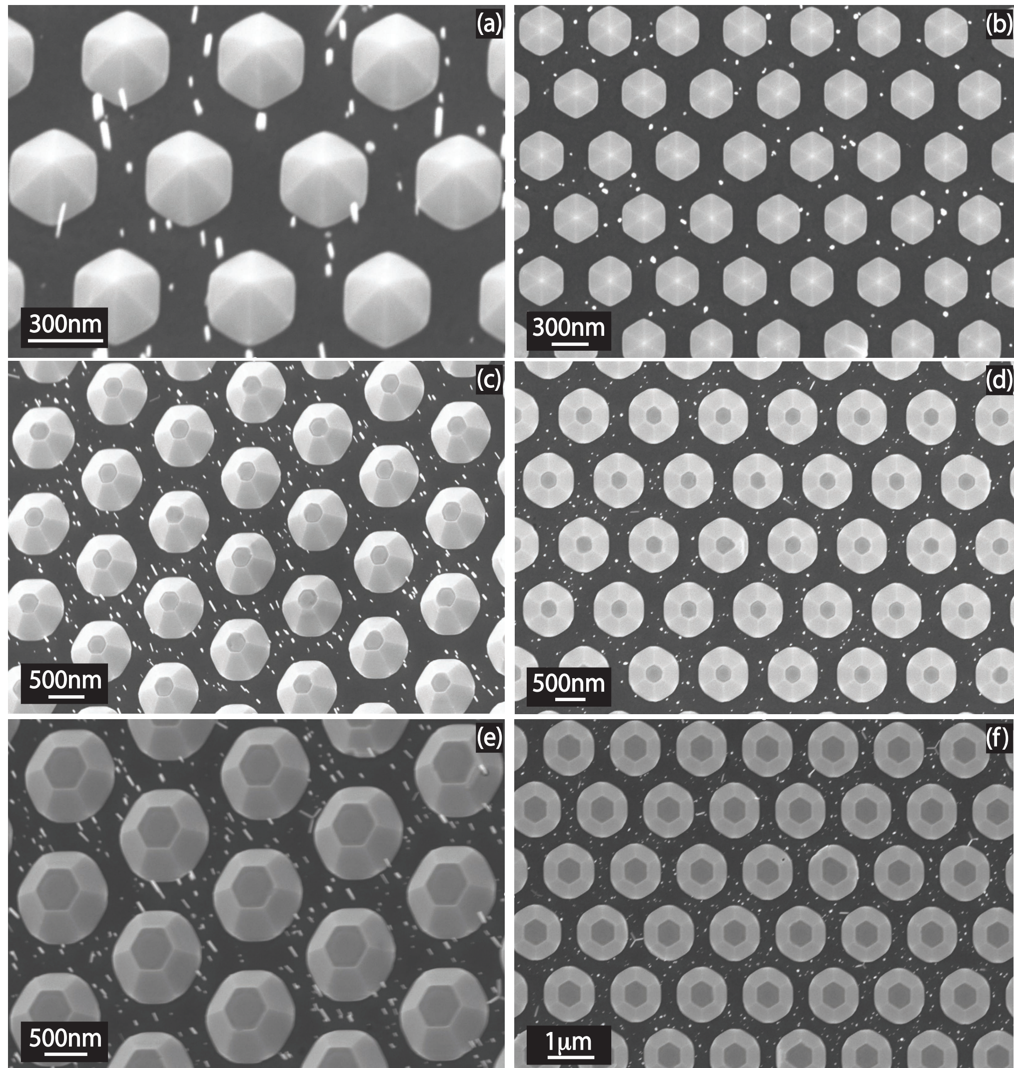

Figure 26: Bird's eye and top view SEM micrographs of SAG GaN nanopyramids on Ti mask. Growth conditions have been set to $t = 45min$, $T_S = 940°C$, nominal $\phi_N = 9\ nm/min$ and nominal $\phi_{Ga} = 5,2\ nm/min$. NPs grown on differen nanoholes diameter are shown in (a)-(b) $d = 300nm$, (c)-(d) $d = 500nm$ and (e)-(f) $d = 800nm$ (Sample G1714).

studied, for a more comprehensive understanding of the growth mechanisms concerned. The SAG of GaN NCs could be divided in three different growth regimes:

A *nucleation regime*, in which GaN nuclei first nucleate in the central part of the Mo nanoholes mask and then coalesce together, until the full coverage of the nanoholes area.

At the beginning of the growth process, Ga and N adatoms impinge on the GaN bare surface of the lithographed nanoholes, but also and especially on the Mo mask surface. Under SAG conditions, the higher diffusion coefficient on Mo mask than on GaN drives Ga adatoms to nucleate into the nanoholes. The preferential nucleation in the center of the nanoholes can also be explained by the lower surface energy of the Mo mask.

The incubation time before nucleation is observed to be strongly related to the size of the nanoholes, in a way in which larger nanoholes show faster nucleation than the smaller ones. Larger diameters experience lower ϕ_{Ga}/ϕ_N local ratio in comparison to smaller nanoholes, thus implying an higher probability for the Ga adatoms reaching the nanoholes to be trapped by a N adatom and nucleate onto the GaN bare surface.

A *polar & semi-polar regime*, in which the axial growth of GaN NCs is supported by the NCs prism axial growth as well as by the semi-polar growth of the NCs tip.

When the axial growth begins, GaN nanostructures show irregular side walls and cylindrical-like shape, without any preferential non-polar facets. This morphology is highly costly in terms of surface energy and thus thermodynamically unstable for a wurtzitic nanocrystal. However, the isotropic growth of the GaN nanostructures within the nanoholes causes the NCs to assume the cylindrical shape of the underlying nanoholes.

As soon as the radial growth begins, the shape of the side walls smooths down and the NCs assume a dodecagonal shape. It is well known that *m*- and *a-plane* are the most energetically favorable non-polar planes [78, 79], therefore due to the total free-surface energy minimization criterion, the formation of NCs with dodecagonal 6*a*/6*m* non-polar facets is promoted [77].

A *semi-polar regime*, in which the axial growth of GaN NCs is supported exclusively by the semi-polar growth of the NCs tip facets.

Once the NCs tip is completely formed, the axial growth reduces without stopping. This phenomenon is supported by the NCs radial growth, which allows a further growth of the NCs tip along its semi-polar directions.

A further observation can be made with regard to the NCs side walls shape evolution. When the NCs tip is completely formed, it is possible to observe a further evolution of the NCs dodecagonal shape to a thermodynamically more stable hexagonal shape, made of 6*m* non-polar facets.

This behaviour has been recently reported also by Gačević *et al.* [80], who observed a similar morphological evolution of the NCs shape. In their letter,

the authors consider, as limiting criterium for NCs morphologies, the minimization of the total free energy per unit volume and found the free-surface per unit-volume energy to be the exclusive driving term for the NCs shape evolution.

In view of the Wulff's theorem [81], an argument based only on surface energies would lead to NCs radial growths conserving the same proportion of *m-* and *a-plane* surfaces, without therefore explaining the expansion of *m-plane* over *a-plane* facets. Moreover, the *m-plane* surface energy is very similar and only slightly lower than that of the *a-plane* surface ($\approx 5\mathrm{meV}/\mathring{A}^2$ lower) [78, 77], thus making difficult to think that a comprehensive explanation of the NC shape evolution, from the dodecagonal to the hexagonal shape, can be based only on surface energy arguments.

With this purpose, it is interesting to consider the density-functional theory study made by Lymperakis *et al.* [82], which shows the presence of a large anisotropy in the diffusion barriers along ($\|$) and perpendicular ($\perp$) to the c-axis for non-polar *m-* and *a-plane* surfaces. For the *a-plane* surface larger diffusion length parallel to the c-axis are observed ($E^{\|}_{\mathtt{diff}} = 0.32\mathrm{eV}$ for *a-plane*, $0.93\mathrm{eV}$ for *m-plane*), while for the *m-plane* surface the in plane anisotropy is reversed, and significantly smaller barriers are found for diffusion normal to the c-direction ($E^{\perp}_{\mathtt{diff}} = 0.63\mathrm{eV}$ for *a-plane*, $0.21\mathrm{eV}$ for *m-plane*). Thus, the lower diffusion barrier path on the *m-plane* (*a-plane*) surface is normal (parallel) to the c-direction.

This implies that the diffusion induced mechanism, which describes the growth of a NC by material transfer from the side facets to the top, is less pronounced on *m-plane* side facets, where only Ga adatoms impinging in close proximity to the top of the NCs are able to reach the top before getting desorbed or incorporated into the side surfaces. At the same time, on *m-plane* surfaces Ga adatoms find much faster diffusion to the facets edges, promoting the expansion of *m-plane* facets. The opposite mechanism takes place for Ga adatoms impinging the *a-plane* facets, where higher diffusion to the top promotes the NCs axial growth, while lower diffusion normal to the c-direction damps the *a-plane* facets growth.

Due to the low diffusion of Ga adatoms on the NCs side walls, once the NCs morphology completely turn into a 6*m* non-polar facets hexagonal shape, the Ga adatoms contribution from the mask accumulate on the lower part of the NCs, bringing to a tampering of the NCs prism shape.

Also the shape evolution of the NCs is related to the size of the undelying lithographed nanoholes. As observed before, the absolute radial growth of NCs having larger diameters is the same than that of NCs of smaller base. Bigger structures need therefore more time to fully change the morphology of their lateral side walls.

In Section 4.3, an overview on the growth of SAG GaN nanostructures on Ti mask was briefly reported. The growth mechanisms under such different SAG

conditions seem to depart from what was observed during the SAG of GaN NCs on Mo mask. In fact, only SAG GaN NPs could be grown and no axial growth was achieved. The crystal quality of these NPs is however higher than that of SAG GaN NCs grown on Mo mask, as much that no SFs formation during the NPs growth was observed.

This divergence in growth mechanisms is probably due to kinetics effects due to the different T_S used during the growth. Kinetics effects are difficult to analyse experimentally, because of the really small window of T_S suitable for the SAG growth (expecially on Mo mask, where the temperatures window is smaller than 10°C). However, the axial growth of SAG NCs on Ti mask has been reported by several groups [74, 75] and should therefore be investigated in a more comprehensive way by further works.

5 InGaN incorporation on GaN-based SAG nanostructures

Once the mechanisms behind the SAG of GaN NCs have been better understood, the additional growth of epitaxial InGaN on the NCs tip has been investigated. This chapter reports on the InGaN growth implementation and the influence of different InGaN growth conditions on the SAG NCs composition and morphology.

As already discussed in Section 2.4, the growth of InGaN alloys takes place under very different conditions in comparison with that of GaN material.

In this chapter, with the aim of promoting indium incorporation during the growth of epitaxial InGaN on SAG GaN nanostructures, different processes for the InGaN growth are carried out and presented.

All of the SAG GaN/InGaN samples, reported in the following sections, underwent a two steps growth. A first step, for the initial growth of GaN NCs arrays, following the standard procedures and nominal conditions reported as best growth conditions in Section 4.1. A second step, performed directly after the formation of the pencil-like SAG GaN NCs array, for the implementation of an epitaxial InGaN cap on the top of such structures.

The morphology of the samples is investigated by SEM imaging. Due to the need of high spatial resolution analysis (see Section 3.3), the characterization on the formation and composition of InGaN heterostructures is performed by scanning transmission electron microscopy (STEM) and SEM chatodoluminescence (SEM-CL) analysis.

Table 4 gives an overview of the nominal growth parameters used during the InGaN epitaxial growth step of the relevant samples presented in this Chapter.

5.1 Growth of epitaxial InGaN on GaN SAG NCs

5.1.1 *InGaN layers based growth conditions*

The samples reported in this section have been grown following an optimized scheme developed for the growth of epitaxial InGaN layers in our system [17]. Here the growth under In bilayer stabilized conditions provided a

Sample	T_S (°C)	ϕ_{Ga} (nm/min)	ϕ_N (nm/min)	$\frac{\phi_{Ga}}{\phi_{Ga}+\phi_{In}}$	Growth time (min)
G1660	625	2.65	3.5	1/4	60
G1648	600	0.42	6	1/4	60
G1649	625	0.42	6	1/4	60
G1646	650	0.42	6	1/4	60

Table 4: Nominal growth parameters used for the InGaN epitaxial growth on SAG GaN NCs (Mo mask).

favorable growth window at $T_S = 700°C$, with obtainable In-concentrations of up to 20%. A degradation of the surface was found due to In desorption, which coincides with the observation of a $(\sqrt{3}x\sqrt{3})R30°$ reconstruction by RHEED. This effect could be counteracted by covering the surface with a protective Ga adlayer at the end of InGaN growth.

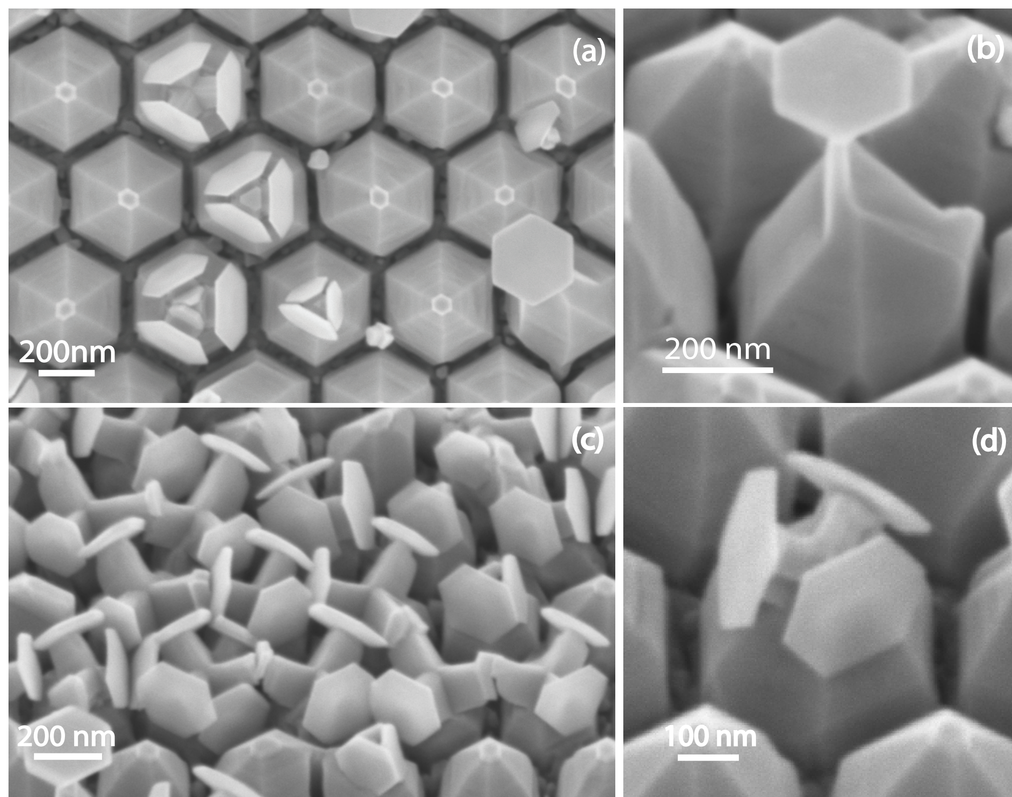

Figure 27: Top and bird's eye view SEM micrograph of sample G1660. Different kinds of nanoplates grew on the top of SOG NCs as well as on the tripod branches grown on the NCs tips.

Accordingly, epitaxial InGaN was grown for 60 min on top of the SAG GaN NCs. The nitrogen flux was changed to 0.5sccm and 300W excitation power, corresponding to $\phi_N = (3.50 \pm 0.05)$ nm/min, while the Ga flux was increased to $\phi_{Ga} = (2.65 \pm 0.05)$ nm min^{-1}. An excess of indium was applied, with a fluxes ratio of $Ga/(Ga + In) \approx 0.25$.

Figure 27 presents top and bird's eye view SEM micrographs of sample G1660, grown under the above mentioned flux conditions (see also Table 4). To avoid indium reevaporation, the T_S during the InGaN growth was set at $T_S = 625°C$. These images show the formation of hexagonal nanoplates on top of (c)-(d) ZB GaN tetrahedron-like structures and on top of (b) SOG GaN NCs (see Section 4.1.2 for elucidations). The observed growth of these hexagonal nanoplates has been also schematized, for facilitating the understanding, in Figure 29.

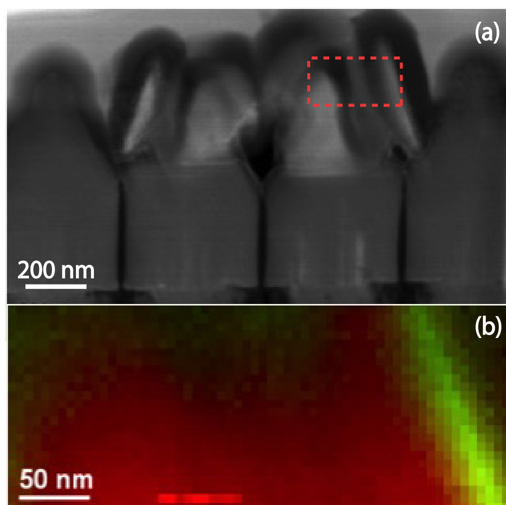

Figure 28: (a) STEM micrograph of nanoplates structures grown on the top of branched NCs (sample G1660). The red dashed rectangle is a guide to the eyes pointing out the area of the EELS analysis. (b) The EELS compositional maps shows the spatial distribution of Ga (in red) and In (in green) within the nanostructures. The experiments were done by R. Zamani, Georg-August University Göttingen.

Figure 28(a) shows a lateral STEM micrograph of sample G1660, while in (b) electron energy loss spectroscopy (EELS) has been employed for studying the material composition of the hexagonal nanoplates. In this case, due to the oblique position of the nanoplates as well as the underneath presence of GaN ZB structures, EELS analysis turned to be a more powerful tool than SEM-CL and allowed to put in evidence the spatial distribution of Ga (in red) and In (in green) within the nanostructures. As a result, it was possible to confirm that the hexagonal nanoplates are formed by homogeneously distributed InGaN material, with an N-polar wurtzitic crystal structure.

The formation of such InGaN nanoplates is of a certain interest, due to their potential employement as whispering gallery mode (WGM) resonators [83]. Following this scope, finite-difference time-domain (FDTD) analysis has been applied to simulate the behaviour as resonators of such platelets. However, no resonance in the frequency domain $\upsilon = (350 - 600)$nm could be revealed, probably due to their excessive small size ($d \approx 250$nm).

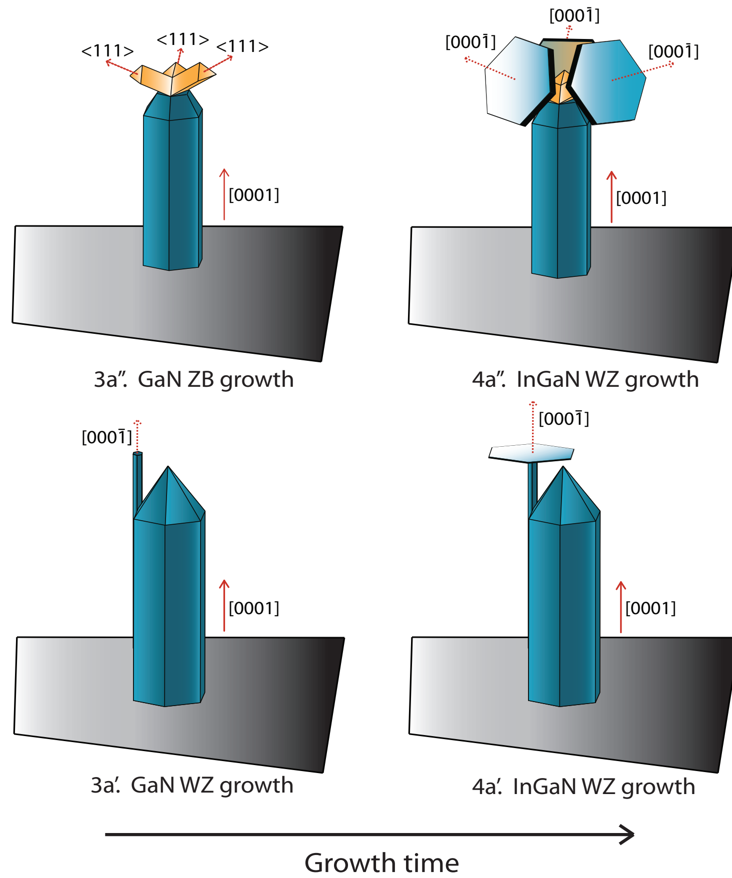

Figure 29: Schematic representation of the hexagonal nanoplates growth on $(3a'' - 4a'')$ the top of ZB tetrahedrons as well as on $(3a' - 4a')$ the tip of SOG NCs. These two representations follow the growth scheme of Figure 25.

By increasing the T_S of the InGaN growth, no InGaN nanoplates have been observed on the NCs structures and SEM-CL analysis (not shown) did not reported any InGaN growth on the NCs tips.

5.1.2 *SAG NCs based growth conditions*

In this section, another approach has been considered, for the growth of epitaxial InGaN on SAG GaN NCs, by taking into account the procedures known from the state of the art [15, 18, 19, 20, 21, 22, 23].

To adjust these conditions to our MBE growth system, the InGaN epitaxial growth step was performed under the same nominal nitrogen flux ($\phi_N = 6\ nm/min$) as for the standard GaN SAG NCs and with a nominal gallium flux of $\phi_{Ga} = 0,42\ nm/min$, which corresponds to the 70% of the standard nominal flux used for the growth of GaN SAG NCs. This ϕ_{Ga} was chosen for supporting the incorporation of indium into the structure, together with a $Ga/(Ga+In) \approx 0.25$ fluxes ratio. Also in these growths, to avoid indium reevaporation, the substrate temperatures were drastically kept lower than during the SAG GaN NCs standard growth and varied from sample to sample from $T_S = 600°C$ (sample G1648) to $T_S = 625°C$ (sample G1649) and $T_S = 650°C$ (sample G1646).

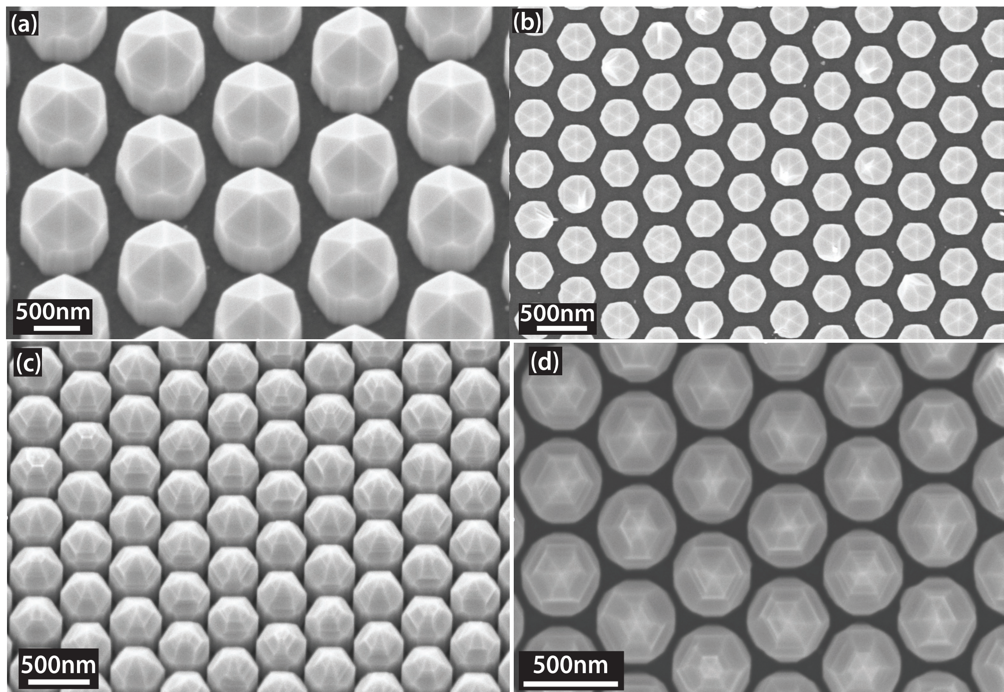

Figure 30: Bird's eye and top view SEM micrograph of SAG GaN/InGaN NCs on Mo mask. For the growth of InGaN, the growth conditions have been set to $t = 60min$, $\phi_N = 6\ nm/min$, $\phi_{Ga} = 0,42\ nm/min$, $Ga/(Ga+In) \approx 0.25$ and (a)-(b) $T_S = 625°C$ (sample G1649), (c)-(d) $T_S = 600°C$ (sample G1648).

Figure 30 shows the bird's eye and top view SEM micrographs of samples (a)-(b) G1646 and (c)-(d) G1648. Comparing the morphology of the samples it can be observed how, even if the SAG GaN growth took place under the same conditions, the different InGaN growth T_S heavily influenced the crystal quality of the final structures. In fact, while the high T_S grown structures are almost free of crystal defects (Figure 30(a)-(b)), the structures grown under lower temperatures show very defective tips (Figure 30(c)-(d)).

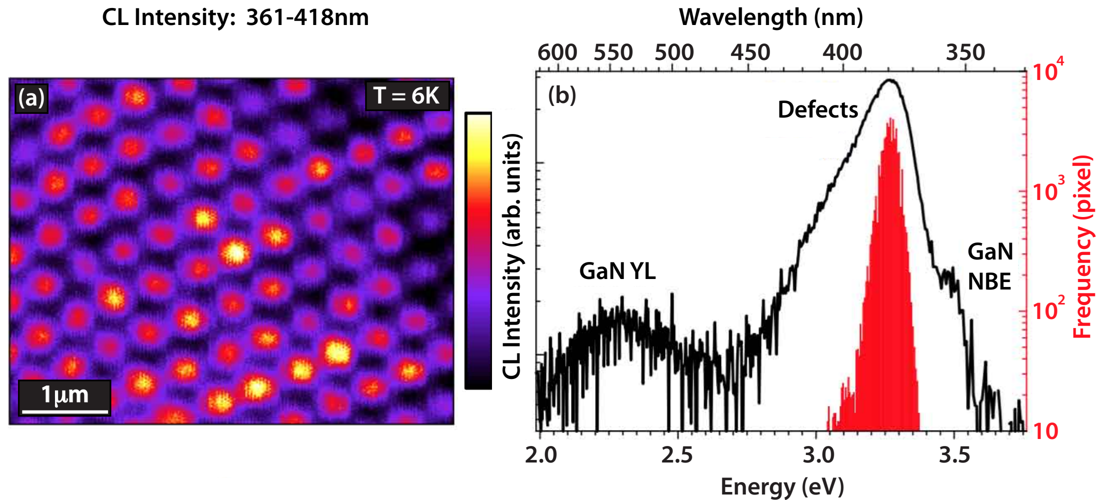

Figure 31: (a) Monochromatic SEM-CL intensity image of sample G1648. The energy range $367 - 418\mathrm{nm}$ corresponds to luminescence emissions due to the presence of GaN ZB and BSFs. (b) CL spectrum in semi-log scale, with spectral resolution of $\sim 1.5\mathrm{nm}$. The red histogram gives the frequency of a specific peak energy. The measurement was performed at $T = 6\mathrm{K}$. The experiments were done by M. Müller, Otto-von-Güricke-University Magdeburg.

A SEM-CL analysis performed on these structures, in collaboration with the Otto-von-Güricke University of Magdeburg, confirmed the different crystal quality of the samples, with increased contributions from GaN ZB and basal stacking faults (BSFs) emissions from the structures grown under lower T_S.

Figure 31(a) shows a monochromatic SEM-CL intensity image of sample G1648. The energy range $361 - 418\mathrm{nm}$, considered in this CL emissions map, corresponds to the luminescence emissions due to the presence of GaN ZB and BSFs within the structures. Figure 31(b) shows the CL spectrum related to the panchromatic SEM-CL image (not shown) of the sample area considered in (a) and in which the spatial distribution of the peaks wavelength is visualized. The histogram in red gives the frequency of a specific peak energy (number of pixels which report a given wavelength of the emission peak), showing a considerable presence of GaN ZB and BSFs within the NCs crystal structure. The GaN yellow luminescence emission results instead anti-correlated with the NCs position and therefore ascribable to the emission from the underlying GaN template. The same emission has been observed in other samples and is

shown in Figure 33.

However, none of the samples, grown under these molecular beam fluxes conditions, showed any CL emission which could be univocally related with a successful InGaN growth onto the NCs tip.

5.2 GROWTH OF EPITAXIAL InGaN ON GaN SAG NPs

The same attempts of growing InGaN heterostructures have been also carried on the SAG GaN NP structures, grown on Ti mask. In this approach, while the SAG NPs have been grown after the conditions reported in Section 4.3, the subsequent InGaN growth has been carried out following the substrate temperatures and flux conditions described in Section 5.1.2.

Sample G1782, for which the T_S during the InGaN growth has been set at $T_S = 650°C$, is shown in the bird eye's and top view SEM micrographs of Figure 32. Two different lithographic fields of this sample are shown: (a)-(b) $d = 200nm$ and $p = 200nm$, (c)-(d) $d = 500nm$ and $p = 200nm$. The inset in (d), showing a SEM micrograph top view magnification of a single NP, emphasize a variation in the nanostructures morphology occurring, also in this growth, after the InGaN growth step.

Differently than the previous samples reported in this Chapter, the growth of InGaN heterostructures on SAG NPs succeeded. Figure 33 shows (a) the SEM micrograph and (b) the corresponding CL spectrum of the InGaN/GaN NPs of sample G1782 ($d = 500nm$ and $p = 200nm$). The CL spectrum points out the GaN near band edge (NBE) emission at 3.46eV and two luminescence contributions from InGaN at 2.81eV and 2.54eV. The histogram in red gives the frequency of a specific peak energy (number of pixels which report a given wavelength of the emission peak), revealing a locally slight variation of InGaN CL on different NPs. To investigate the spatial occurrence and spatial homogeneity of different CL emission wavelengths, monochromatic CL images limited to a small spectral range are shown in Figure 33(c)-(f). The (c) GaN NBE emission and (d)-(f) InGaN emissions results from these images anti-correlated, confirming that GaN NBE emission originates from the template, while InGaN CL from the nano pyramidal structures.

In Figure 34, a panchromatic SEM-CL image of the NPs exhibits highest CL intensity from the InGaN/GaN NPs. CL spectra from the single NPs have been investigated and reveal homogeneous CL intensity distribution within the different nanostructures.

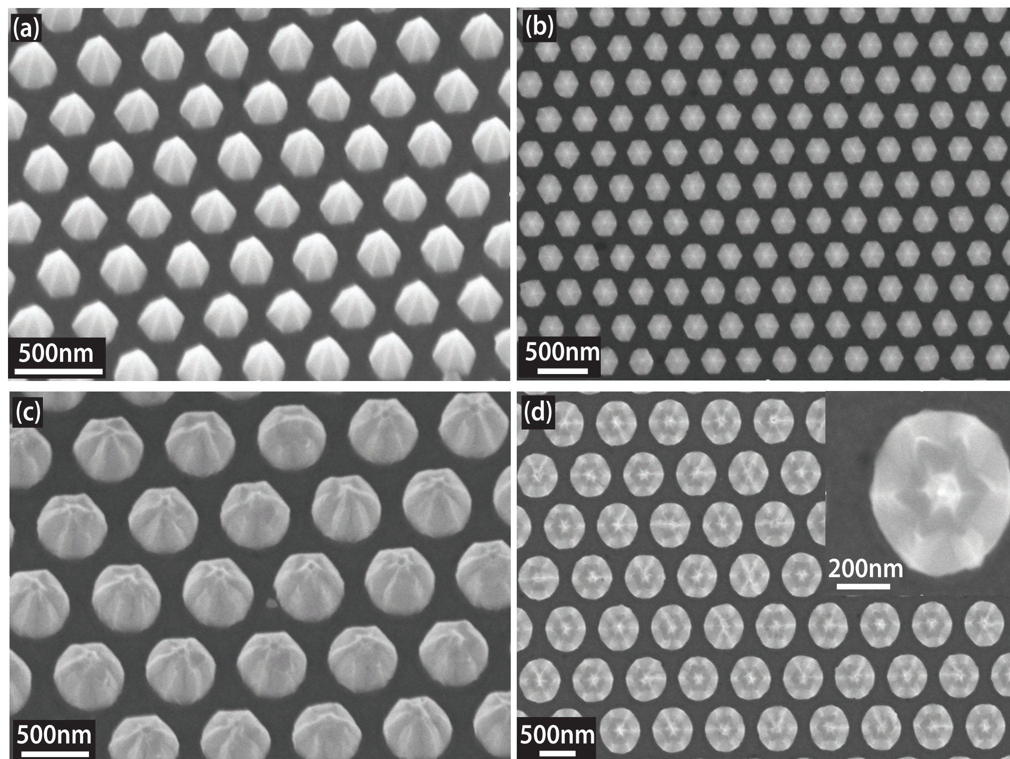

Figure 32: Bird's eye and top view SEM micrograph of SAG GaN/InGaN nanopyramids on Ti mask. The micrographs show to two different lithographic fields of sample G1782 having holes diameter of (a)-(b) $d = 200nm$ and $p = 200nm$ (c)-(d) $d = 500nm$ and $p = 200nm$ (the inset in (d) shows the SEM micrograph top view magnification of a single NP).

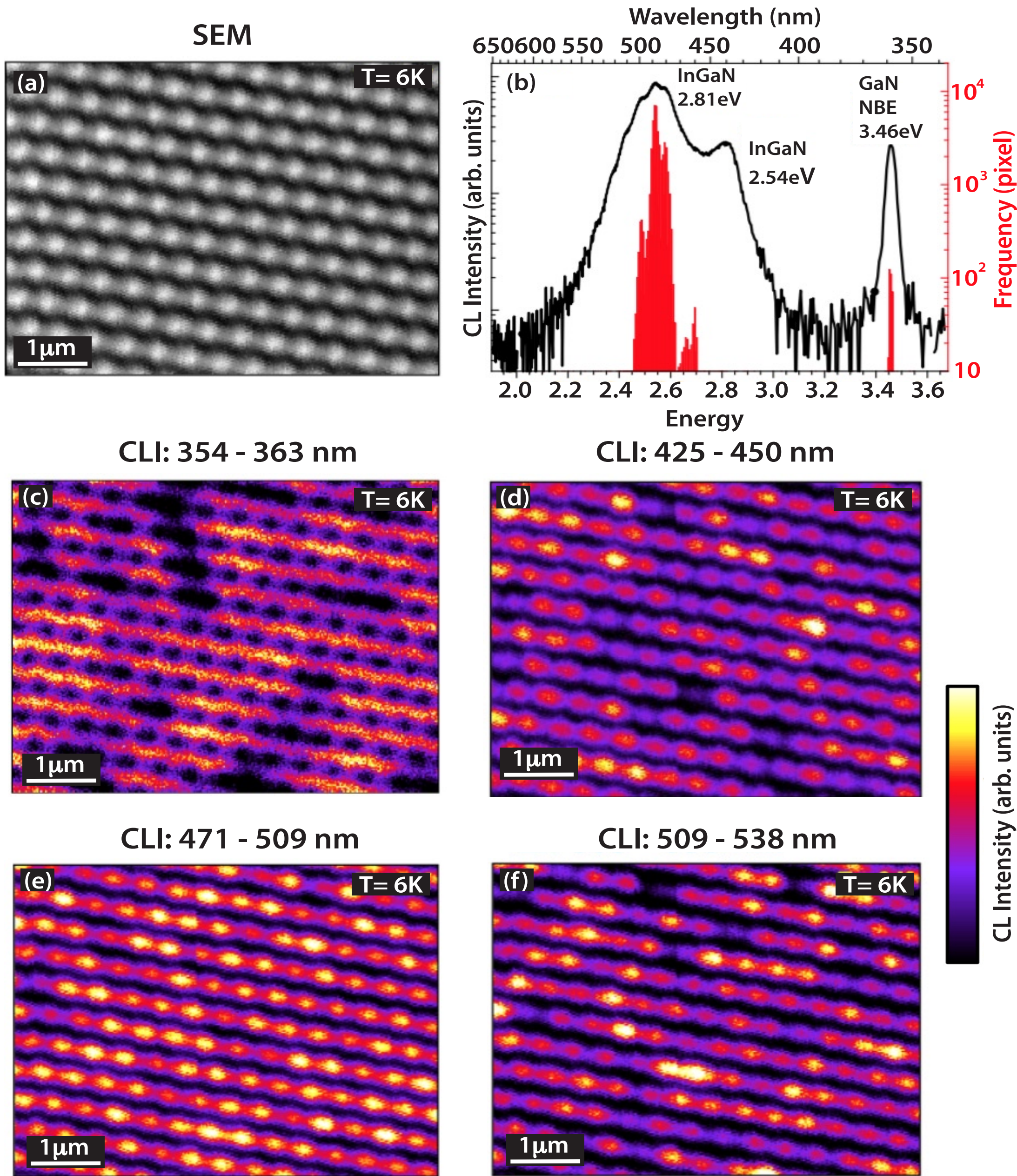

Figure 33: (a) SEM micrograph of SAG GaN/InGaN nanopyramids array and corresponding (b) CL spectrum in semi-log scale, with spectral resolution of $\sim 1.5\text{nm}$. The red histogram gives the frequency of a specific peak energy. (c)-(f) Corresponding monochromatic CL intensity images. The energy ranges correspond to luminescence presumably due to: (c) GaN NBE, (d)-(f) InGaN emissions. The intensity scale is identical for all images. The measurement was performed at $T = 6\text{K}$. Sample G1782. The experiments were done by M. Müller, Otto-von-Güricke-University Magdeburg.

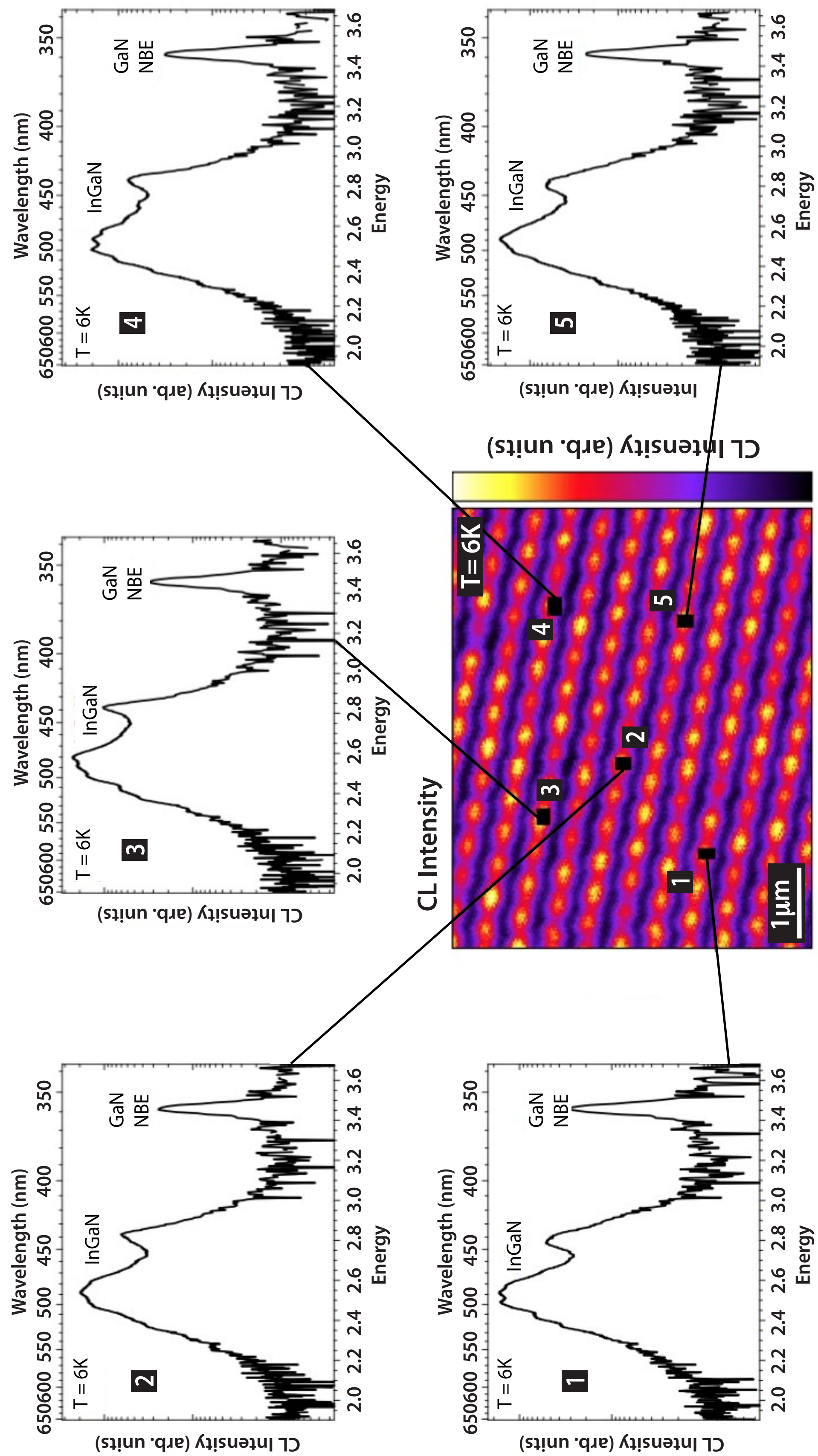

Figure 34: Panchromatic CLI image on a logarithmic scale and CL spectra in semi-log scale of single nanopyramids $(1-5)$ of sample G1782. The nanopyramids show an homogeneous emission of InGaN material, ascribable to two main In content components with CL peak at $E \sim 2.54eV$ and $E \sim 2.81eV$. The experiments were done by M. Müller, Otto-von-Güricke-University Magdeburg.

5.3 RESULTS DISCUSSION

In this Chapter different growth procedures, for the implementation of epitaxial InGaN heterostructures on the SAG GaN NCs, have been investigated. Two different epitaxial InGaN growth approaches have been considered and applied on several SAG GaN NCs sample under different T_S conditions. As already reported in Section 2.4, the T_S plays a crucial role on the growth of InGaN alloys and it is therefore important to consider a representative range of T_S for studying, in a comprehensive manner, the epitaxial InGaN growth dependency on T_S.

In Section 5.1.1, the growth of epitaxial InGaN on NCs has been first performed by applying an optimized scheme developed for the growth of epitaxial InGaN layers in our system [17]. For $T_S \geqslant 650°C$, this procedure did not result in any InGaN growth. However, by reducing the substrate temperature to $T_S \leqslant 625°C$, the formation of hexagonal nanoplates on top of ZB GaN tetrahedron-like structures and SOG GaN NCs (see Section 4.1.2) has been observed.

After EELS analysis, the composition of such nanostructures has been revealed to be formed by homogeneously distributed InGaN material, with N-polar wurtzitic crystal structure.

Similar platelets has been observed also by *Kouno et al.* [83, 84], who reported their appearance after the epitaxial InGaN growth step on top of Ti mask SAG GaN N-polar NCs. In their works *Kouno et al.* proposed and simulated the behaviour of such nanoplates as whispering gallery mode (WGM) resonators.

FDTD analysis on our structures showed no resonances in the frequency domain $\upsilon = (350 - 600)nm$. However, it is believed that such result may depends exclusively on the small size of the grown nanoplates ($d \approx 250nm$). Since the size of such structures may be controlled by varying the growth time, further investigations on these structures are needed to realize microcavity arrays, for application as low consumption GaN-based laser and sensing devices.

In Section 5.1.2, a second approach for the epitaxial InGaN growth has been performed by taking into account the procedures known from the state of the art [15, 18, 19, 21] and adapting such conditions to our MBE growth system.

Also in this case, several T_S have been applied to the epitaxial InGaN growth step and a strong temperature dependency of the NCs morphology has been observed. At lower T_S the morphology of the NCs exhibits very poor crystal quality, which supplementary investigations by SEM-CL analysis related to the formation of SFs and ZB crystal structure, whilst at higher T_S the NCs showed a less defective morphology. However, after SEM-CL investigation, no epitaxial InGaN growth could be observed in any of these samples.

In Section 5.2, the epitaxial growth of InGaN on SAG GaN NPs has turned to be successful. SEM-CL investigations showed homogeneous CL intensity distribution within the different SAG NPs, with the presence of two main InGaN

alloy contributions. According to Moses and Van der Walle [38], it is possible to estimate the indium incorporation of the two main CL emission components and ascribe them to an In concentration between $x = 0.13$ and $x = 0.20$.

The unsuccessful InGaN growth on Mo mask SAG GaN NCs may be explained by considering that the contributions in the state of the art [15, 18, 19, 21], about the growth of epitaxial InGaN on SAG of GaN NCs, do not report on the MBE growth using Mo mask and that such growth conditions may therefore differ more than expected from the ones reported in this chapter.

However, Mo mask has been chosen in this work, as preferred mask material for the SAG of NCs, to provide continuity of investigation with the work of our former colleagues.

When the same approach has been applied to the SAG GaN NPs grown on Ti mask, the growth of epitaxial InGaN turn out successful. This result, however, has to be read also considering the fact that the SAG GaN NPs did not show axial growth of non-polar surfaces and consequently the diffusion processes on this structures are also different from that expected on axially grown NCs.

6 InGaN incorporation on GaN-based self-organized nanocolumns

During the growth of SAG NCs, parasitic nucleation may occur on the metal mask with consequent growth of disordered self-organized (SOG) NCs. This process may be supported by the presence of imperfections on the metal mask, but is generally observed when the growth time is long enough to make the Ga-adatoms diffusion length on the SAG NC sidewalls to be smaller than the height of the NC itself. As reported in the previous chapter, the spatial compositional characterisation of InGaN/GaN NCs is a very challenging matter, which needs the employment of high spatial resolution experimental techniques. This requirement is even more essential when dealing with SOG NCs, which are typically inhomogeneous in both distribution and dimensions, with diameters which sporadically are larger than ∼100 nm. In this chapter the growth of SOG GaN/InGaN/GaN NCs and their investigation, by means of several high-spatial resolution techniques, are presented and discussed.

As already introduced in Section 2.4.2, experimental [25] and computational [27] evidence in literature suggest In incorporation to be easier on GaN $(000\bar{1})$ (N-polar) than on GaN (0001) (Ga-polar) epitaxial layers, so that higher temperatures can be used for a given indium concentration. This suggestion has been considered in this work with the aim of investigating the growth of InGaN/GaN heterostructures on GaN-based N-polar NCs.

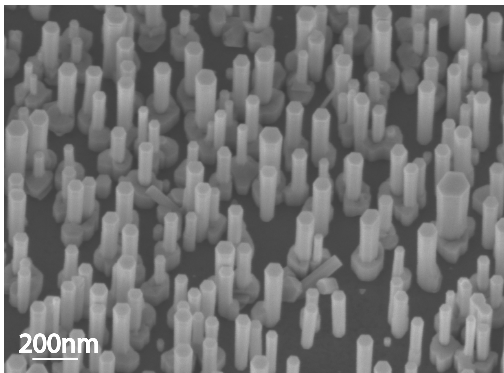

Figure 35: SEM birds eye view micrograph of as grown GaN/InGaN/GaN SOG NCs (sample G1406). Figure adapted from Ref. [86].

Figure 35 shows a SEM micrograph of the as-grown sample G1406 in a range were SOG NCs grow on an unpatterned area of the Mo mask due to self-induced nucleation. A closer look reveals a morphology which differs markedly from the one of Ga-polar SAG NCs (investigated in the previous chapters), since the SO growth results in flat top facets characteristic of $(000\bar{1})$ N-polar plane [15, 16, 85]. The influence of the N-polarity on the heterostructure formation has been investigated by means of different high spatial resolution techniques: nano X-ray fluorescence (nano-XRF) and diffraction (nano-XRD), performed

Growth steps	Growth time (min)	T_S (°C)	ϕ_N (nm/min)	ϕ_{Ga} (nm/min)	$\frac{Ga}{Ga+In}$
GaN	180 min	780	5.65	0.50	1
InGaN	60 min	700	3.50	2.65	0.25
GaN	30 min	700	5.65	0.50	1

Table 5: MBE growth conditions used for sample G1406.

in collaboration with the nano-imaging beamline ID22NI of the ESRF (see Section 3.3.2 for technical details), high-angle annular dark-field scanning transmission electron microscopy (HAADF-STEM) and high-resolution transmission electron microscopy (HR-TEM). These powerful tools allowed to study the indium inclusion as well as the axial and radial elemental distribution in single NCs. Additionally single NC micro-photoluminescence (μ-PL) investigations have been performed, in collaboration with Dr. P. C. Ricci of the physics department of the University of Cagliari, in order to supplement the nano-XRF/XRD experimental results and allow a consistent interpretation of In incorporation in the heterostructures [86].

6.1 MBE growth conditions

Sample G1406 has been grown on a 10 nm thick Mo layer deposited on a commercial $\mathrm{GaN}(0001)/\mathrm{Al_2O_3}$ template. The growth process followed three steps, which are also summarized in Table 5. First, GaN NCs grew following the standard procedures and nominal conditions reported as best growth conditions in Section 4.1. In a second step the growth of InGaN on top of the GaN nanocolumns was performed at a substrate temperature of $T_S = 700°\mathrm{C}$ for 60 min, with an increased Ga flux of $\phi_{Ga} = (2.65 \pm 0.05)$ $\mathrm{nm/min}$ and a Ga/(Ga + In) flux ratio of about 0.25. The nitrogen flux was changed to 0.5 sccm and 300 W excitation power, corresponding to $\phi_N = (3.50 \pm 0.05)$ $\mathrm{nm/min}$. The last step for the deposition of a GaN cap layer was carried out by keeping constant the substrate temperature at $T_S = 700°\mathrm{C}$, in order to avoid the re-evaporation of the In. This growth step was performed for 30 min with the same ϕ_{Ga} and ϕ_N as for the growth of GaN in the first step.

6.2 Characterization techniques

The acquisition of nano-XRF and nano-XRD maps of single NCs requires a Synchrotron light source hard X-ray nano-probe station. To this purpose,

the potentiality of the nano-imaging beamline ID22NI (now installed at the upgraded ID16B) at the European Synchrotron Radiation Facility (ESRF) has been used. This multi-technique X-ray microscope simultaneously probes the elemental distribution and structural properties of crystalline nano-objects. Experimental set-up and procedures have been described in detail in Section 3.3.2.

For the X-ray characterization, the NCs were mechanically removed from the substrate and dispersed on a commercial Silson 100 nm thick silicon nitride membrane window. This manipulation was a necessary step to prevent the signal from the GaN template to overlap the one coming from the NC heterostructures during the X-ray fluorescence analysis.

For the high-spatial resolution XRF mapping, the pink beam mode provided a spot size and therefore a spatial resolution of 70×95 nm^2, while for simultaneous nano-XRF and nano-XRD mapping the monochromatic beam mode was used with a spot size of 136×154 nm^2.

The crystal structure of the NCs and In-incor poration have been also investigated by means of HR-TEM and HAADF-STEM imaging (Z-contrast). These experiments were performed on a FEI Titan ETEM G2, equipped with a C_S image corrector and a monochromator operated at 300 kV.

Single NC micro-photoluminescence (μ-PL) has been carried out at room temperature in backscattering geometry using the 405.0 nm line of wavelength stabilized diode modules (Ondax Inc. Surelock LM series) coupled with a Reflecting Bragg Grating (Optigrate-Braggrade 405) to narrow the laser line. The laser excitation beam (with an output power of about 0.5 mW) was focused through a 100× objective on a surface area of about 1 μm^2 (corresponding to an excitation power density of about 5×10^7 mW/cm^2).

6.3 CHARACTERIZATION RESULTS

The elemental composition of several SOG single GaN/InGaN/GaN NCs, deposited on a SiN membrane, was investigated by nano-XRF imaging. Figure 36(b) shows the SEM micrograph of a representative NC with a length of about 640 nm and diameter between 130 nm and 190 nm. In Figure 36(a) the averaged XRF spectrum of the scanned area comprising the whole NC is shown. This spectrum includes the Ga-$K_{(\alpha+\beta)}$ and In-K_α fluorescence peaks. Figure 36(c) and Figure 36(d) show the elemental distribution maps of In-K_α and Ga-$K_{(\alpha+\beta)}$ XRF emissions, repectively. The data clearly show an InGaN/-GaN heterostructured NC morphology. In Figure 36(e)-(g) the elemental distribution maps of Pb-L, Mo-$K_{(\alpha+\beta)}$ and Ag-K_α are characterized by a random distribution all over the scanned area, without any evidence of correlation with the NC morphology and are most probably related to the set-up collima-

tor (Pb), to the mask material (Mo) and the silver paint (Ag) used to create an electrical conduction on the SiN template, for performing the SEM analysis.

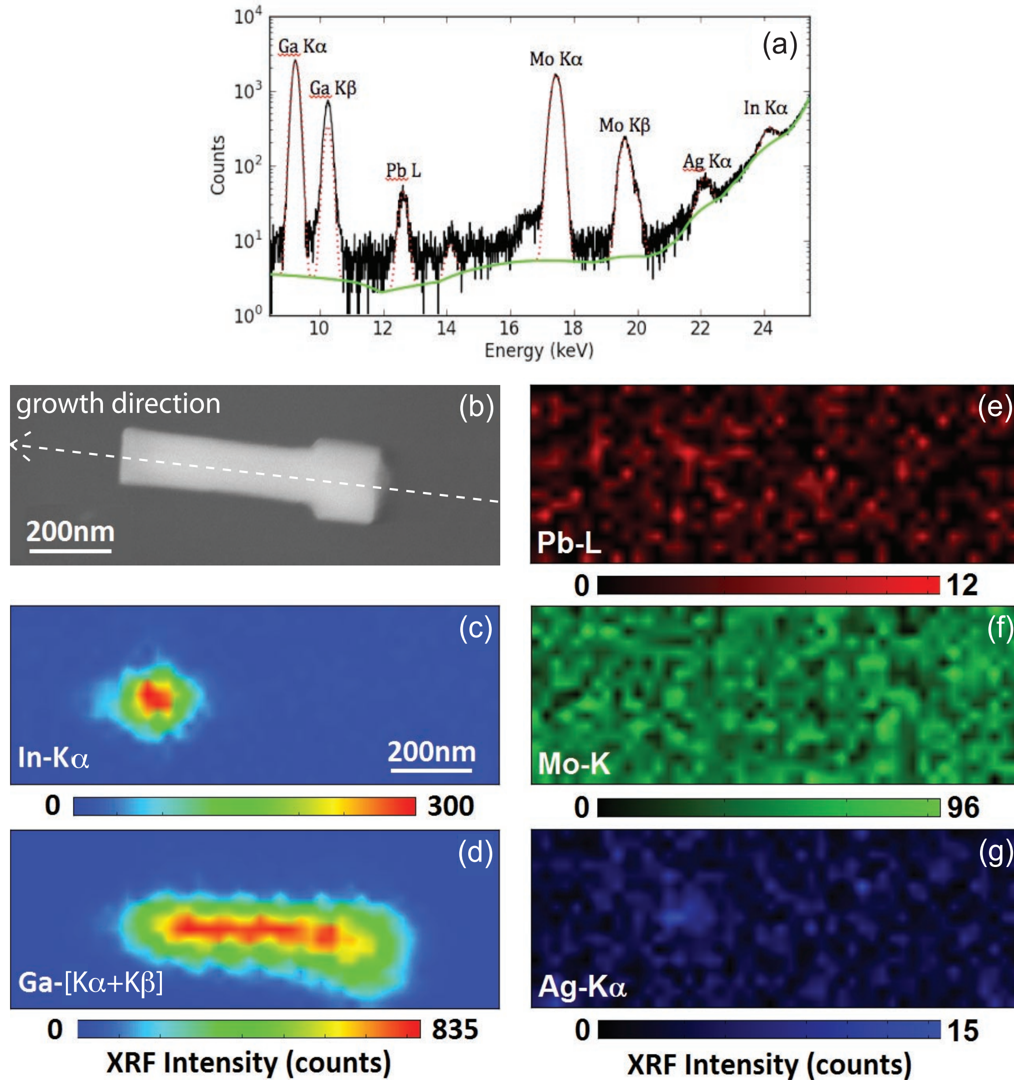

Figure 36: (a) Average XRF spectrum of a representative SOG single GaN/InGaN/-GaN NC (sample G1406) dispersed on a SiN membrane. (b) SEM micrograph of the NC. (c) XRF spatial distribution maps of In-K_{α}, (d) Ga-$K_{(\alpha+\beta)}$, (e) Pb-L, (f) Mo-$K_{(\alpha+\beta)}$ and (g) Ag-K_{α} emission lines. The XRF maps were taken with a pixel size of 25 x 25 nm^2 and an accumulation time of 200 ms per pixel. Figures adapted from Ref. [86].

In Figure 37(a) the spatial distributions of gallium (green) and indium (red) are superimposed to visualize the InGaN/GaN heterostructure formed along the axis of the NC.

The XRF intensity profiles reveal the axial (Figure 37(b)) and the radial (Figure 37(d)) elemental distribution of gallium and indium. The axial profile does

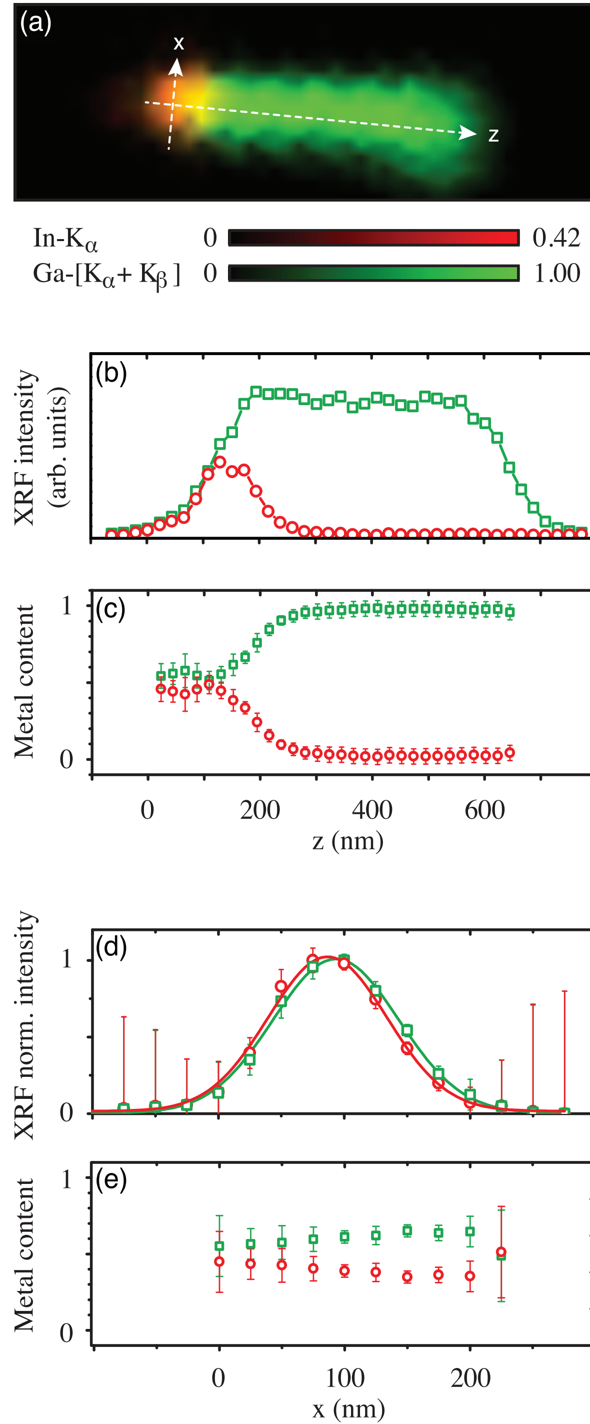

Figure 37: (a) XRF spatial distribution maps of In-K_{α} (red) and Ga-$K_{(\alpha+\beta)}$ (green) emissions of the same NC showed in Figure 36. The color coded In and Ga contents were estimated from the XRF data. The dashed arrows indicate position and direction of the XRF intensity axial (b) and radial (d) profiles. Ga and In relative elemental composition along the axial (c) and radial (e) profiles. Each point represents one pixel (25 x 25 nm^2). The zero point of the spatial coordinates corresponds to the top of the NC. Figures adapted from Ref. [86].

not show any clear evidence of the GaN cap layer. Instead the overlapping tails of both intensities toward the NC surface point to a In-rich top region. At around $z = 200$ nm below the surface the In-profile reveals a marked transition from $In_xGa_{1-x}N$ to GaN.

The elemental composition of the NC was estimated by processing the XRF intensity data using the PyMca program [71] and the results are shown in Figure 37(c). The transition at the GaN/InGaN interface along the growth direction extends over about 100 nm (corresponding to 4 pixels) with a continuous increase of the In concentration from zero up to about 42% of the relative metal content.

In Figure 37(d) the radial XRF intensity profiles for both elemental distributions at the top of the NC are peaked at the center due to decreasing sampled volume towards the edge of the nanocolumns. The relative elemental composition in Figure 37(e) suggests the presence of a radially homogeneous indium distribution in the heterostructure within the sensitivity of the technique. In fact, even if the pixel size was set at 25 x 25 nm^2, the spatial resolution is always dominated by the beam size. Therefore, details smaller than the beam size cannot be considered as real features, but only as a guess, which has to be confirmed by complementary higher spatial-resolution electron techniques.

HR-TEM and HAADF-STEM has been performed on several SOG NCs. The results for a representative one are depicted in Figure 38 and Figure 39. The contrast reveals the presence of a trapezoidal InGaN core embedded in a thin (about 7 nm) GaN shell. The formation of an InGaN/-GaN core-shell structure could not be detected in the XRF radial profile (Figure 37(d)), since the GaN shell and cap layer thickness is below the spatial resolution of the XRF measurements (beamsize of 70 x 95 nm^2).

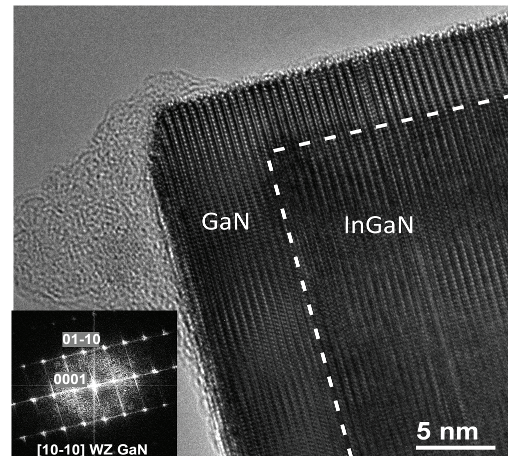

Figure 38: HR-TEM image of the InGaN/-GaN interface at the top of the NC showed in Figure 39, with the corresponding power spectrum (FFT) as inset. Figure adapted from Ref. [86].

Since the intensity in HAADF-STEM contrast depends on the atomic number (Z-contrast) and the thickness of the sample (neglecting channelling effects due to defects or strain), an increase in intensity evidences the presence on indium in the NC. According to it, Figure 39(a) reveals the presence of indium in the NC, if the sample thickness is constant. On the other hand, the intensity profile directly reflects the thickness variation due to the prismatic shape of the NC, if the composition is constant. For this reason and assumining a constant composition, the radial intensity profile of Figure 39(c) puts in evidence the prismatic shape of the NC. Further it reveals

a core-shell structure, which is reflected in the fact that the intensity is much lower at the border of the NC, due to the absence of indium. The gradual increase of the axial intensity profile in Figure 39(b) is due to an increasing indium concentration on the one hand and due to the increasing diameter of the trapezoidal InGaN heterostructure on the other hand. The presence of ripples in the spectrum is attributed to inhomogeneities in the indium concentration.

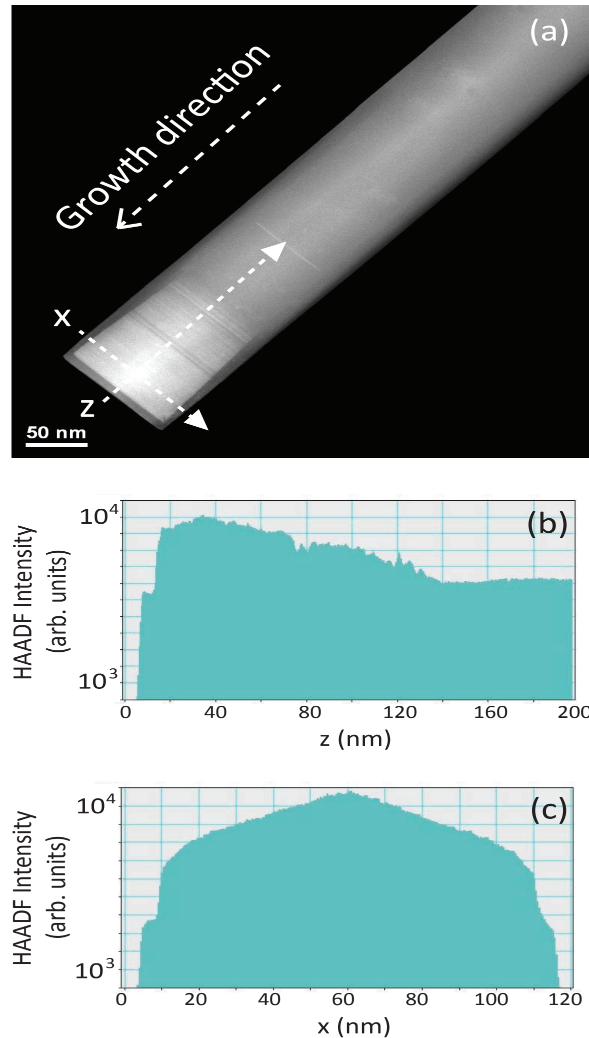

Figure 39: (a) (HAADF)-STEM image along the $[1\bar{1}00]$ zone axis of a SOG GaN/InGaN/GaN NC (sample G1406). The arrows indicate the position and the direction of the (b) axial and (c) radial intensity profiles. Figures adapted from Ref. [86].

In Figure 40 the results from the simultaneous nano-XRF and nano-XRD mapping are shown. These measurements allow to correlate the elemental dis-

tribution with the structural properties for the same NC that was studied by high resolution XRF and shown in Figure 36 and Figure 37.

The nano-XRF/nano-XRD maps are measured with a monochromatic beam and a larger pixel size of 100×100 nm^2, which explains the differences in resolution between the XRF maps in Figure 37(a) and Figure 40(a). Still, the $In_xGa_{1-x}N$ and GaN regions can be clearly separated.

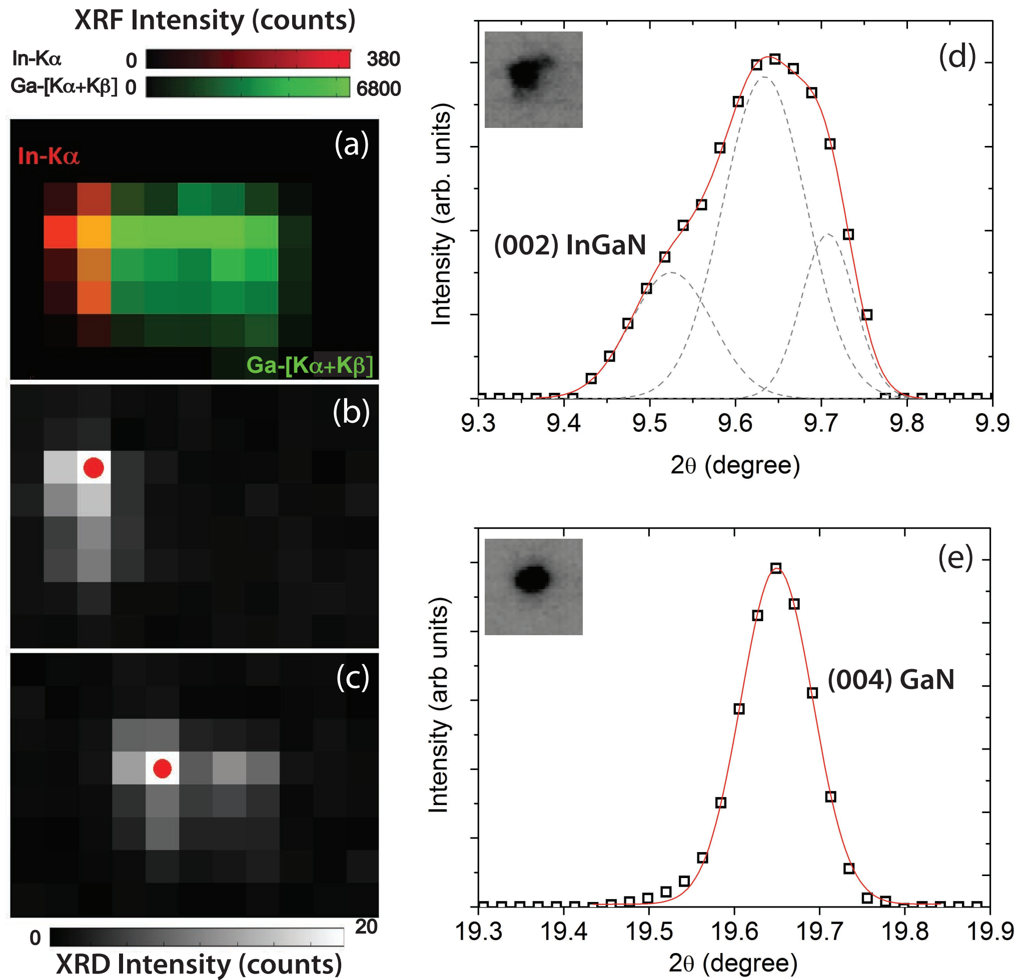

Figure 40: (a) XRF spatial distribution maps of In-K_α (red) and Ga-$K_{(\alpha+\beta)}$ (green) emissions of the same NC showed in Figure 36. (b)-(c) Spatial intensity distribution maps of two different diffraction peaks collected on the scanned area. (d)-(e) 2θ spectra corresponding to the (002)-$In_xGa_{1-x}N$ alloy and (004)-GaN X-ray diffractions peaks acquired at the pixel marked with red dots in the spatial distribution maps (b) and (c), respectively. The insets show the CCD images of this two diffracted signals. The combined XRF/XRD maps were taken with a pixel size of 100 x 100nm^2 and an accumulation time of 3 s per pixel. Figures adapted from Ref. [86].

2θ position	x_{In}
9.71°	(0.06 ± 0.02)
9.68°	(0.13 ± 0.02)
9.52°	(0.30 ± 0.04)

Table 6: Estimated indium concentrations for the (002)-$In_xGa_{1-x}N$ angular intensity profile of Figure 40(d).

Diffraction peak intensity maps and θ-2θ spectra at two selected positions (indicated by red dots) are shown in Figure 40(b)-(e).

The peak at around $2\theta = 9.65°$ shown in the diffraction map in Figure 40(b) appears only in the $In_xGa_{1-x}N$ region of the NC and corresponds to the (002)-InGaN reflection. The inset of Figure 40(d) shows the CCD image at the most intense pixel pointed out in Figure 40(b). It reveals a multi-component spot and an asymmetric peak in the angular intensity profile (Figure 40(b)). Figure 40(c) shows the spatial diffraction map of the (004)-GaN reflection in the pure GaN region of the NC. Figure 40(e) shows the θ-2θ spectrum and the corresponding CCD image acquired at the most intense pixel marked with a red dot in Figure 40(c).

In general, the relation between the interplanar distance $\boldsymbol{d}$, the Miller indices (hkl) and the lattice parameters $\boldsymbol{a}$ and $\boldsymbol{c}$ of the wurtzite structure is:

$$\frac{1}{\boldsymbol{d}_{hkl}^2} = \frac{4}{3}\frac{h^2 + k^2 + hk}{\boldsymbol{a}^2} + \frac{l^2}{\boldsymbol{c}^2} \,. \tag{24}$$

For basal lattice planes, Equation 24 can be simplified to $\boldsymbol{c} = l \cdot \boldsymbol{d}_{00l}$, where the interplanar distance can be easily obtained from *Bragg's law*. Thus, the (002) and (004) diffraction spots are only related to the $\boldsymbol{c}$-lattice constant of the wurtzite structure.

The (004)-GaN peak was fitted with a single Gaussian and its angular position corresponds to a lattice constant of $\boldsymbol{c} = (5.18 \pm 0.02)$ Å, in good agreement with the value expected for unstrained GaN material [28].

Owing to the inherent ability of nanocolumns to effectively relax strain, we make the simplified assumption of fully unstrained InGaN. Then, it is straightforward to estimate the indium content by means of *Vegard's law* [87]. Despite the poor statistics imposed by limitations in the experimental configuration, the (002)-InGaN diffraction peak in Figure 40(d) can be well fitted with three components, which reveal the presence of at least three different indium concentrations in the small $In_xGa_{1-x}N$ region where the diffraction spot was measured (Figure 40(b)). The computed concentrations are reported in Table 6.

Considering the whole set of NCs studied in this work, the indium concentration varied from $x = 0.06$ up to $x = 0.32$, showing an inhomogeneus indium incorporation within the individual heterostructures and within the ensemble of SOG NCs.

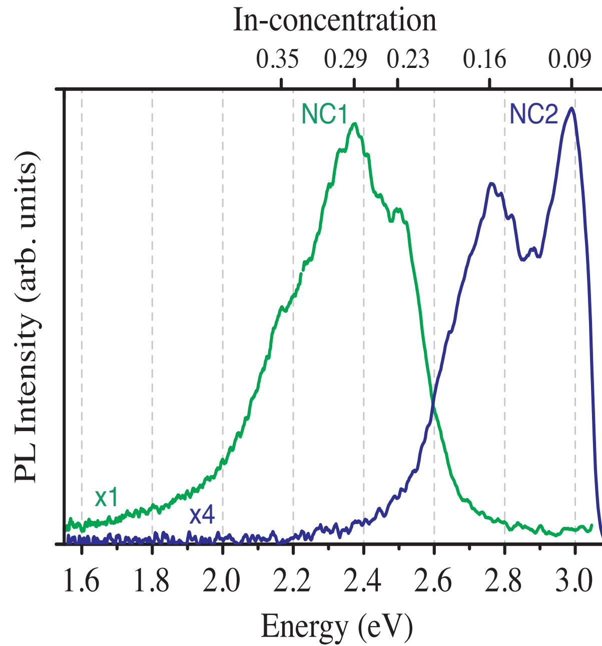

Figure 41: Continuous-wave micro-PL of two representative SOG GaN/InGaN/GaN NCs (sample G1406). The excitation line at 405 nm had a power of about 0.5 mW and a spot area of about 1 μm^2 ($\sim 5 \cdot 10^7$ mW/cm^2). Figure adapted from Ref. [86].

This trend is also corroborated by micro-photoluminescence measurements (μ-PL) carried out on single SOG NCs at room temperature. The excitation wavelength of $\lambda = 405$ nm was chosen in order to suppress GaN related luminescence and focus on the InGaN emission. Figure 41 shows the spectra of two representative SOG GaN/InGaN/GaN NCs. The different spectral positions of the emission bands confirm the inhomogeneous indium incorporation in different NCs. Moreover, different indium concentrations are also observed within the same NC. According to Moses and Van der Walle [38], it is possible to estimate an indium incorporation ranging from $x = 0.23$ to $x = 0.35$ for NC1, while the two main components of NC2 can be ascribed to an In concentration between $x = 0.09$ and $x = 0.16$.

6.4 RESULTS DISCUSSION

In this Chapter, the growth of SOG GaN/InGaN/GaN NCs has been investigated and the formation of well defined InGaN/GaN heterostructures has been observed by means of several high-spatial resolution techniques.

SOG NCs nucleated on different substrates, e.g. Si(111) or as here on a thin Mo-mask layer, grow along the N-polar direction $[000\bar{1}]$ and have a flat tip morphology with a *c-plane* top facet, which can be explained by semi-quantitative arguments based on surface energies under N-rich conditions [16].

As already discussed in Section 2.4 Duff *et al* [27] have recently studied the incorporation of indium at (0001) Ga-polar and $(000\bar{1})$ N-polar InGaN surfaces by *ab initio* methods. In their work they found much smaller energy barriers for indium diffusion and desorption on the Ga-polar surface as compared to the N-polar surface. Nath *et al* [25] reported a comparative growth study of N-face and Ga-face InGaN layers grown by MBE both on N-polar and Ga-polar templates under identical growth conditions and by changing the substrate temperature. They found the indium incorporation efficiency to be significantly higher in N-face InGaN than in Ga-face InGaN at any given substrate temperature. These results support the fact that for a given In composition the N-polar orientation allows for higher growth temperatures than the Ga-polar one. Similar conclusions have been drawn by Xu *et al* [26] for the growth of InN layers by MBE, where they reported the possibility to grow N-polar InN films at higher temperature than In-polar ones.

All these results are consistent with the observation in our experiments that no indium is incorporated when growing Ga-polar GaN/InGaN NCs (Section 5.1), while indium incorporation takes place on the N-polar NCs (Section 6.3).

The elemental composition of several self-organized single GaN/InGaN/-GaN NCs deposited on a SiN membrane was investigated by nano-XRF imaging and clearly showed an InGaN/GaN heterostructured NC morphology. The XRF intensity profiles reporting the axial elemental distribution of gallium and indium (Figure 37(b)) did not reveal any clear evidence of GaN cap layer at the top of NCs. However, HAADF-STEM images of the tip region of SOG N-polar NCs show the presence of a trapezoidal InGaN core embedded in a thin (about $7\ \mathrm{nm}$) GaN layer. The formation of an InGaN/GaN core-shell structure could not be detected in the XRF radial profile (Figure 37(e)), since the GaN shell and cap layer thickness are below the spatial resolution of the XRF measurements (beamsize of $70 \times 95\ \mathrm{nm}^2$). Furthermore, the HAADF-STEM intensity profile reveals the tendency of indium to segregate to the upper region of the heterostructure. Consistent with the results obtained from the XRD analysis, PL measurements on single SOG NCs exhibit an inhomogeneous incorporation of indium in different NCs and also within the same heterostructure. The indium concentration has a broad range between $x = 0.09$ and $x = 0.34$. Within

the error of the method, this result agrees with the quantification of indium content deduced from the XRF intensity and the XRD peak positions.

7 CONCLUSIONS

In this work, the mechanisms regulating the MBE SAG of GaN-based NCs have been investigated, under different growth conditions, with the aim of improving the control over the growth of InGaN/GaN heterostructures.

First of all, following the investigations of our research group former colleague A. Urban [16], the morphological evolution of GaN SAG NCs, grown on Mo mask, has been further investigated, as a function of the nominal ϕ_{Ga}/ϕ_N ratio, revealing severe changes in the NCs shape, even under small variations of ϕ_{Ga}/ϕ_N ratio. Furthermore, a study on the growth mechanisms, as a function of the growth time and the lithographed nanohole dimensions, showed that GaN nuclei first nucleate in the central part of the Mo nanoholes mask and then coalesce together, until the full coverage of the nanoholes area is complete (*nucleation regime*). After this stage, the axial growth of GaN NCs begins, supported by the growth of the NCs tip in both, polar and semi-polar directions (*polar and semi-polar regime*). Once the NCs tip is completely formed, the axial growth reduces and is supported exclusively by the semi-polar growth of the NCs tip facets (*semi-polar regime*). Also a shape evolution of the NCs is observed as a function of the underlying lithographed nanohole dimensions.

Once the mechanisms behind the SAG of GaN NCs, grown on Mo mask, have been better understood, the additional growth of epitaxial InGaN on the NCs tip has been investigated and different InGaN growth approaches have been considered to this scope. However, the growth of semi-polar InGaN heterostructures on the top of GaN SAG NCs did not proceed straightforward. No InGaN growth could be pointed out along the semi-polar directions of the pencil-like shaped NCs, while the formation of InGaN nano-plates on top of ZB GaN tetrahedron-like structures, as well as on top of SOG GaN NCs, has been observed, when using epitaxial InGaN layers growth conditions.

Finally, the attention was turned to the disordered SOG NCs grown on the Mo mask during the growth of InGaN/GaN SAG NCs. Differently from the SAG NCs, which develop along the Ga-polar direction, these NCs grow with flat tip and along the N-polar direction. With the support of high spatial resolution techniques, it has been possible to observe, on the top of SOG NCs, the presence of well defined InGaN/GaN heterostructures, confirming the higher indium incorporation efficiency on N-polar orientation than on Ga-polar one.

A preliminary study on the growth mechanisms of SAG GaN nanopyramids (NPs), grown on Ti mask, has also been performed in this work. Notwithstand-

ing the higher crystal quality achieved for these structures, as compared with that of SAG GaN NCs grown on Mo mask, no axial growth could be observed.

However, when the same approaches for the growth of epitaxial InGaN on SAG GaN NCs have been applied to the SAG GaN NPs, grown on Ti mask, the growth of InGaN has turned to be successful, with very homogeneous InGaN distribution, within the different SAG NPs.

In conclusion, if on one hand the MBE growth of GaN/InGaN heterostructures on the semi-polar facets of SAG NCs grown on patterned Mo mask does not seems to be a valid alternative for the development of a phosphor-free NCs-based white LEDs technology, on the other hand and in view of the positive preliminary results, further studies are needed for a better understanding of the growth mechanisms taking place when choosing Ti masks for the selective growth of the GaN/InGaN nanostructures.

Part III

APPENDIX

APPENDIX A

A.1 MOLYBDENUM OR TITANIUM DEPOSITION AT THE UNIVEX 350

This section has been written to give a step-by-step procedure guideline for depositing thin metal layers of molybdenum or titanium by means of electron beam evaporation technique.

First of all, the samples have to be pretreated as described in Section 3.1. Once they are ready to be introduced in the Univex 350, the following steps have to be considered:

- **Check** that the *main power* is turned *off*
- If in the *touch screen* the function *auto mode* is *on*, turn the *manual mode on*
- **Release the vacuum** from the chamber by pressing in the touch screen on *V*4
- Wait ;-)
- **Open** the chamber and **decharge** all the possible components which could be touched
- Check the transparency of the glass window and change it if needed
- **Open** the shutter by pressing the button *shutter* in the *MAXTEK controller* (not in the touch screen)
- Place the samples in the chamber
- **Close** the *shutter* again
- In the *MAXTEK controller screen* check the *Healt percentage* (%) of the detector crystal (if lower then 92%, replace the crystal)
- **Check** the residual quantity of the material to be evaporate in the crucible (*turn on* the *power* of the *crucible indexer*, select the *Manual Mode* and select the *number of the material* being evaporated by turning the knob between 1 and 6 (Molybdenum is 3, Titanium is 4)
- The shutter over the bowl can be open by pressing *Shutter* in the *touch screen* (when *e-beam* and not AS053 is selected)
- **Close** the chamber and start the vacuum by pressing on *P*1 on the *touch screen*.
- **Wait** until the pressure is at least around $10^{-6}\mathrm{mbar}$
- **Turn on** the rotation of the sample holder by pressing on the *black disk* under the showed temperature in the touch screen
- **Check** that the *voltage adjust knob* is adjusted to *zero*

- **Turn** the *main power* **on**
- In the same panel **set** the lever on *manual*
- **Wait** 2-3 minutes
- **Check** the *emission current knob* in the *control panel* is adjusted to 0
- **Turn on** the *voltage emission*
- **Check** that all the 5 green lamps *(ZERO, WATER, DOORS, VAC, READY)* are *on*
- Looking the *voltage value* on the display, **turn slowly** (in the *main power panel*) the voltage adjust knob until the value reaches 7eV (which means 7keV in the reality)
- In the same main *power panel* **set** at this point the lever on *auto* (the *main voltage* is on *manual* only when adjusting the voltage)
- **Start** cooling the sample holder by pressing on *cooling* in the *touch screen*
- **Check** that the screen in the *MAXTEK controller* is set on the material you want to evaporate, if not change the program by pressing:

  1. *PROGRAM*
  2. *START*
  3. Select the process e.g. *Mo* or *Ti*
  4. *START* and immediately *ABORT*
  5. *RESET*
  6. *MANUAL*

- Take the joystick and insert it in *manual*
- **Start** increasing the *Power* % of the beam until ~ 10% (for Mo) and ~ 2% (for Ti)
- Adjust the position parameters of the electron beam, by selecting in the *sweep select* the number for the material being evaporated (Molybdenum is 4, Titanium 3), setting the *manual mode* and moving the *LAT-LONG* knobs of the *POS line*
- **Increase** the *power* % of the beam until ~ 18% (for Mo) and ~ 5% (for Ti)
- **Check** that the deposition rate is 1å/s by opening the shutter over the bowl (press *shutter* in the *touch screen*) and adjust the *power* % consequently.

  To **start the deposition**:
- **Press** *shutter* and *zero* (in the *MAXTEK controller*) to put to *zero* the *thickness counter*
- **Deposit** the desired thickness of material (take always under control the deposition rate)
- **Close** the *shutter* which cover the samples (press *shutter* in the *MAXTEK controller*)
- **Close** the shutter over the bowl (press *shutter* in the *touch screen*)

Shutting down procedure:

- **Decrease** the *power* % until 0%
- **Set** again the lever on *auto* on the *main power panel*
- **Decrease** slowly the *voltage*
- **Turn off** the *voltage emission*
- **Wait** 2-3 minutes
- **Turn** the *main power* **off**
- **Stop** the rotation of the sample
- **Turn off** the cooling of the sample holder
- **Vent** the chamber by pressing on *V4* in the *touch screen*
- Wait ;-)
- **Open** the chamber and **decharge** all the possible components which could be touched
- Remove the samples
- **Close** the chamber and start the vacuum by pressing on *P1* on the *touch screen*.

A.2 PATTERN A MASK FOR SAG WITH ELECTRON BEAM LITHOGRAPHY (EBL)

In this section a step-by-step procedure for patterning arrays on metallic masks by means of EBL is described.

First of all, the sample has to be pretreated as described in Section 3.1. Afterwards, it is important to deposit polystyrene microspheres on the sample, as close as possible to the area in which the lithography will take place (but not on it!), this will help during the focusing process. Now the sample is ready to enter the EBL device:

- **Open** the N_2 knob
- **Vent the chamber:** in the *Smart SEM window* click on *Vacuum –> Vent*
- Select the *TV detector* to see inside the chamber: *Detectors –> Signal A = TV*
- In the *e_LiNE window* check that the z-coordinate is about 30 mm
- Wait! ;-)
- Open the chamber and insert the sample holder with the samples
- While closing again the chamber ***check*** on the *Smart SEM window* that the sample holder ***doesn't get in touch*** with other components of the *e_LiNE* facility
- After closing pump again the chamber: in the *Smart SEM window* click on *Vacuum –> Pump*
- Wait ;-) (the device needs to reach $\sim 2e^5$ $mbar$ to allow the beam on)

In the meanwhile the right EHT and aperture can be set ($EHT : 20kV$ and $Aperture : 10\mu m$): in the *Smart SEM window* click on:

- *Gun –> EHT Target* = 20.00kV and then on *Apertures –> Aperture Size*
- **Turn on the beam:** in the *Smart SEM window* click on *Gun –> Beam state = EHT off –> EHT on*
- **Go to the Faraday cup position:** in the *e_LiNE window* click on the icon *Adjustments –> Stage control –> Position –> Faraday on ush (universal sample holder) –> go*
- The beam is still blanked, to open it click in the *e_LiNE window* on the icon: *Beam on/off (Ctrl+B)*
- Put the Faraday cup in the middle of the screen and magnify to the maximum allowed
- **Measure the current:** in the *e_LiNE window* click on the icon *Exposure –> Beam Current –> Measure*
- Click on the *Exposure Parameter Calculation* icon in the *Exposure Parameter section* to calculate the exposure parameters commensurate to the daily beam current

Area	Area Step Size	it is the distance between pixels and has to be ~ 1/10 of the total area (in my case 0.004 μm)
	Area Dose	the value comes from the dose test (in my case 350 $\mu As/cm^2$)
	Area Dwell Time	will be calculated
	Beam Speed	it has to be between 2 and 5 mm/s (but for dose tests it doesn't matter!)
Curved elements	Curved step size	(0.004 μm)
	Area Dose	(350 $\mu As/cm^2$)
Dot	Dot Dose	(0.04 pAs)
	Dot Dwell Time	will be calculated

- to calculate the *Dwell Times* click on the *Calculate area/Curved Elements/ dot-dwell time* icon
- **Move to the sample:** in the *e_LiNE* window click on *Adjustments –> Stage control –> Position –> Sample* 1 (e.g.) *–> go*
- in the *Smart SEM window* put the down/left-corner of your sample in the middle of the screen (use the *Crosshairs icon* tool)
- **Coordinates adjustment:** in the *e_LiNE window Adjustment –> Adjust UVW (Local) –> Origin correction –> Adjust*
- **Angle correction:** take the measure of the *Label* 1 at the left-down-corner of the sample and the *Label* 2 at the right-down-corner of the sample by clicking on

Read XY position as *Mark* 1 and *Read XY position* as *Mark* 2 –> *Adjust*

- Check if everything went good: Blank the beam with the *Beam on/off (Ctrl+B)* icon, drive for instance to $U = 10mm$ and $V = 10mm$, open again the beam and check if the opposite corner of the sample is in the middle of the *Smart SEM window*
- Drive the beam to the polystyrene microspheres and *adjust Focus, Stigmator X/Y and Aperture X/Y* on them (at this point, to have a easier view on the microspheres, start the process by changing the aperture to $30\mu m$, and after adjusting the parameters move again to $10\mu m$ aperture and improve the image)
- Move away from the microspheres and select the *Frame Average Mode*:
- in the *Smart SEM window: Scanning* –> *Spot* (try several points with different exposure times)
- then again: *Scanning* –> *Spot* (to blank the exposure)
- If everithing is satisfactory: –> **Write field alignment (WFA)**
- Set the beam again on the microspheres
- in the *e_LiNE window* click on:
  Microscope control icon –> *set parameters* 1000*x*, $100\mu m$ –> *set*
- an then:
  Adjustment –> *Align Write Field Procedures* –> *Manual* (it scan at the desired amplification)
- Click on the icon:
  New image –> *Scan image continuously (Shift+F5) (take an image)* –>
  –> *Scan image*
- Check if the image is enough clear and if there are distinctive feature, which could be easily recognized (if not, move to another position on the sample and do it again)
- Click on the icon:
  New Position list window (a *Position list NONAME.pls window* opens)
- Drag the *write field alignment file* (i.g. $100\mu m$ *WF - Manual ALWF* $25\mu m$ marks in *Position list NONAME.pls*
- Click on the *square button* (*Scan selection* (F9)) for scanning
- On the scanned picture, look for a characterizing feature (which can be easily recognized)
- Click on the scanned image (pointing at the same position of the chosen feature) for 3 times: *ctrl + left mouse click* –> *continue*
- the software will ask to accept the aligment:
  –> *yes* (or *no* if the alignment is not satisfactory)
- Close the Position list *NONAME.pls* and click on *no*
- Click again on the icon *New Position list window* and follow the same process for smaller size of *WFA file* (generally $25\mu m$, $5\mu m$ and $1\mu m$ marks)
- Check if the write field alignment went good: in the *e_LiNe* computer click on
  Start –> *Programs* –> *Raith* –> *Raith Protocol Tool* (Right data and shift should be at around 0, while the zoom at around 1)
- Open the file with the designed mask which has to be written on the

sample: in the *e_LiNE window* click on the icon
Design –> open another database file (Ctrl+O) –> find the file!

- Open a *New Position list window* and drag the file in it
- Set the position on which the exposure has to start [e.g. if the exposure cover an area of $0.5x0.5mm^2$, and the exposure has to be done in the middle of the sample (which is $10x10mm^2$) the position values to set are $U = 4.5mm$ and $V = 4.5mm$]
- Set the *Layer 0*
- Set the value of the *Dose Factor* at 1.1 (or perform a dose test to find the new good value)
- Click with the *right button of the mouse –> Properties*
- In the *Exposure Properties window* click on *Exposure Parameter* and check if everything is correct. If needed the time needed for the exposure to complete can be calculate, clicking on *Times* (this process can take a really long time if the mask pattern is big)
- when all the parameters are checked, click on *ok*
- Always in the *e_LiNE window* click on *Scan –> All...*

The exposure will now run!

A command to shutdown the beam once the exposure is finished can be added in the *Position list NONAME.pls* file (otherwise after exposure the beam will stay on):

- in the *e_LiNE window* click on *Automation* and drag the file *Beam Shutdown* in the *Position list NONAME.pls* file

This can also be done manually when the exposure is finished: in the *Smart SEM window* click on
Gun –> Beam state = EHT on –> EHT off

Once the beam is off the chamber can be vent and the samples bring out.

ACKNOWLEDGMENTS

The accomplishment of this thesis would not have been possible without the financial support from the European Union Seventh Framework Programme under grant agreement no. 265073 (nanowiring), as well as without the permanent support I received from a large number of people throughout the last years.

I would like to thank Prof. Dr. Angela Rizzi and Dr. Jörg Malindretos for giving me the possibility of joining their research group, as well as the chance of taking part in the Nanowiring Project, which allowed me to develop the doctoral studies in the most stimulating scientific environment I could ever have wished for. In particular I thank them for the fruitful discussions, the after lunch coffee (or better, for the real *espresso*, which is priceless for an Italian abroad) and the emotional care that they always showed me when needed. I really appreciated it.

A special thanks goes to Dr. Arne Urban, who literally taught me all the background of the experimental techniques that I needed to start the work. He also had the bad luck, together with Dr. Reza R. Zamani after him, to share the office with a temperamental colleague like me. They both gained my full respect for their positive response to cultural shocks.

Essential to this work have been the countless discussions with Dr. Christian Zube, who is also responsible, together with Dr. Reiner Bormann and Dr. Hans-Joachim Helms, of my outstanding integration within the German culture. I am sure that no other *Wohngemeinschaft* would have achieved similar results.

Very meaningful to me has also been the scientific support of Dr. Pier Carlo Ricci, whose ongoing cheering for me date from the time of my bachelor degree.

Thanks to Dr. Andrea Pescaglini, Dr. Davide Cammi and Dr. Eleonora Secco, for their friendship and to have shared with me both the sweet and the bitter moments of this journey.

Finally, and especially for his support once I left Germany, I need to thank my Tobias, because he never doubted it.

This work would not have either started, without the backing of my family: *the encouragement of my father, the strength of my mother and the love of my sister*.

BIBLIOGRAPHY

[1] S. P. DenBaars, D. Feezell, K. Kelchner, S. Pimputkar, C.-C. Pan, C.-C. Yen, S. Tanaka, Y. Zhao, N. Pfaff, R. Farrell, M. Iza, S. Keller, U. Mishra, J. S. Speck, and S. Nakamura. Development of gallium-nitride-based light-emitting diodes (LEDs) and laser diodes for energy-efficient lighting and displays. *Acta Materialia*, 61(3), 2013. doi: 10.1016/j.actamat.2012.10.042.

[2] Matthew T. Hardy, Daniel F. Feezell, Steven P. DenBaars, and Shuji Nakamura. Group III-nitride lasers: a materials perspective. *Materials Today*, 14 (9):408– 415, 2011. doi: http://dx.doi.org/10.1016/S1369-7021(11)70185-7.

[3] Nichia Chemical Ind. Ltd., S. NAGAHAMA, M. SENOH, and S. NAKAMURA. European Patent 1017113: Nitride semiconductor device, August 2012.

[4] Toyoda Gosei Co., Nagoya University, M. Kotaki, I. Akasaki, and H. Amano. European Patent 0483688: Light emitting semiconductor device using gallium nitride group compound, January 1997.

[5] Osram Opto Semiconductors Gmbh, U.D. Strauss, and A. Weimar. Deutsches Patent 10152922: Nitrid-basierendes Halbleiterbauelement, May 2010.

[6] Philips Lumileds Lighting Company, Koninklijke Philips Electronics, J.G. Neff, S.J. Bierhuizen, and J.E. Epler. European Patent 2425462: Controlling edge emission in package-free led die, July 2013.

[7] URL https://www.nobelprize.org/nobel_prizes/physics/laureates/2014/popular-physicsprize2014.pdf.

[8] Hongjian Li, Panpan Li, Junjie Kang, Zhi Li, Zhicong Li, Jing Li, Xiaoyan Yi, and Guohong Wang. Phosphor-free, color-tunable monolithic InGaN light-emitting diodes. *Applied Physics Express*, 6(10):102103, 2013. doi: 10.7567/APEX.6.102103.

[9] I.-H. Ho and G. B. Stringfellow. Solid phase immiscibility in GaInN. *Applied Physics Letters*, 69(18):2701, 1996. doi: 10.1063/1.117683.

[10] J. E. Northrup, L. T. Romano, and J. Neugebauer. Surface energetics, pit formation, and chemical ordering in InGaN alloys. *Applied Physics Letters*, 74(16):2319, 1999. doi: 10.1063/1.123837.

[11] D. Gerthsen, E. Hahn, B. Neubauer, A. Rosenauer, O. Schön, M. Heuken, and A. Rizzi. Composition Fluctuations in InGaN Analyzed by Transmission Electron Microscopy. *physica status solidi (a)*, 177(1):145–155, 2000. doi: 10.1002/(SICI)1521-396X(200001)177:1<145::AID-PSSA145>3.0.CO;2-0.

[12] G.B. Stringfellow. Microstructures produced during the epitaxial growth of InGaN alloys. *Journal of Crystal Growth*, 312(6):735–749, 2010. doi: 10.1016/j.jcrysgro.2009.12.018.

[13] Xiaobin Niu, Gerald B. Stringfellow, and Feng Liu. Phase separation in strained epitaxial InGaN islands. *Applied Physics Letters*, 99(21):213102, 2011. doi: 10.1063/1.3662927.

[14] Daniel F. Feezell, James S. Speck, Steven P. DenBaars, and Shuji Nakamura. Semipolar $(20\overline{2}\overline{1})$ InGaN/GaN Light-Emitting Diodes for High-Efficiency Solid-State Lighting. *Journal of Display Technology*, 9(4):190–198, 2013. doi: 10.1109/JDT.2012.2227682.

[15] S. Li and A. Waag. GaN based nanorods for solid state lighting. *Journal of Applied Physics*, 111(7):071101, 2012. doi: 10.1063/1.3694674.

[16] A. Urban, J. Malindretos, J.-H. Klein-Wiele, P. Simon, and A. Rizzi. Ga-polar GaN nanocolumn arrays with semipolar faceted tips. *New Journal of Physics*, 15(5):053045, 2013. doi: 10.1088/1367-2630/15/5/053045.

[17] D. Broxtermann. *Towards high electron mobility in GaN* (0001) *based InGaN and AlGaN heterostructures*. PhD thesis, Georg-August-Universität Göttingen, 2011.

[18] Hon-Way Lin, Yu-Jung Lu, Hung-Ying Chen, Hong-Mao Lee, and Shangjr Gwo. InGaN/GaN nanorod array white light-emitting diode. *Applied Physics Letters*, 97(7):073101, 2010. doi: 10.1063/1.3478515.

[19] S. Albert, A. Bengoechea-Encabo, P. Lefebvre, F. Barbagini, M. A. Sanchez-Garcia, E. Calleja, U. Jahn, and A. Trampert. Selective area growth and characterization of InGaN nano-disks implemented in GaN nanocolumns with different top morphologies. *Applied Physics Letters*, 100(23):231906, 2012. doi: 10.1063/1.4728115.

[20] S. Albert, A. Bengoechea-Encabo, X. Kong, M. A. Sanchez-Garcia, E. Calleja, and A. Trampert. Monolithic integration of InGaN segments emitting in the blue, green, and red spectral range in single ordered nanocolumns. *Appl. Phys. Lett.*, 102:181103, 2013. doi: 10.1063/1.4804293.

[21] Th Kehagias, G P Dimitrakopulos, P Becker, J Kioseoglou, F Furtmayr, T Koukoula, I Häusler, A Chernikov, S Chatterjee, Th Karakostas, H-M Solowan, U T Schwarz, M Eickhoff, and Ph Komninou. Nanostructure and strain in InGaN/GaN superlattices grown in GaN nanowires. *Nanotechnology*, 24(43):435702, 2013. doi: 10.1088/0957-4484/24/43/435702.

[22] Steven Albert, Ana Bengoechea-Encabo, Xiang Kong, Miguel A. Sánchez-Garcia, Achim Trampert, and Enrique Calleja. Correlation among Growth Conditions, Morphology, and Optical Properties of Nanocolumnar InGaN/GaN Heterostructures Selectively Grown by Molecular Beam Epitaxy. *Crystal Growth & Design*, 15(6):2661–2666, 2015. doi: 10.1021/cg501798j.

[23] Ž. Gačević, N. Vukmirović, N. García-Lepetit, A. Torres-Pardo, M. Müller, S. Metzner, S. Albert, A. Bengoechea-Encabo, F. Bertram, P. Veit, J. Christen, J. M. González-Calbet, and E. Calleja. Influence of composition, strain, and electric field anisotropy on different emission colors and recombination dynamics from InGaN nanodisks in pencil-like GaN nanowires. *Phys. Rev. B*, 93(12):125436, 2016. doi: 10.1103/PhysRevB.93.125436.

[24] D. N. Nath, E. Gür, S. A. Ringel, and S. Rajan. Molecular beam epitaxy of N-polar InGaN. *Applied Physics Letters*, 97(7):071903, 2010. doi: 10.1063/1.3478226.

[25] D. N. Nath, E. Gür, S. A. Ringel, and S. Rajan. Growth model for plasma-assisted molecular beam epitaxy of N-polar and Ga-polar $In_xGa_{1-x}N$. *Journal of Vacuum Science & Technology B: Microelectronics and Nanometer Structures*, 29(2):021206, 2011. doi: 10.1116/1.3562277.

[26] K. Xu and A. Yoshikawa. Effects of film polarities on InN growth by molecular-beam epitaxy. *Applied Physics Letters*, 83(2):251, 2003. doi: 10.1063/1.1592309.

[27] A. Ian Duff, L. Lymperakis, and J. Neugebauer. Understanding and controlling indium incorporation and surface segregation on $In_xGa_{1-x}N$ surfaces: An ab-initio approach. *Physical Review B*, 89(8), 2014. doi: 10.1103/PhysRevB.89.085307.

[28] H. Morkoç. *Nitride Semiconductor Devices: Fundamentals and Applications*. WILEY-VCH Verlag GmbH & Co. KGaA, Weinheim, 2013.

[29] M. Grundmann. *The Physics of Semiconductors: An introduction including nanophysics and applications*. Springer, 2nd edition, 2010.

[30] F. Bernardini and V. Fiorentini. Nonlinear macroscopic polarization in III-V nitride alloys. *Physical Review B*, 64(8), 2001. doi: 10.1103/PhysRevB.64.085207.

[31] O. Ambacher, J. Majewski, C. Miskys, A. Link, M. Hermann, M. Eickhoff, M. Stutzmann, F. Bernardini, V. Fiorentini, V. Tilak, B. Schaff, and L. F. Eastman. Pyroelectric properties of Al(In)GaN/GaN hetero- and quantum well structures. *Journal of Physics: Condensed Matter*, 14:3399–3434, 2002. doi: 10.1088/0953-8984/14/13/302.

[32] M. Suzuki, T. Uenoyama, and A. Yanase. First-principles calculations of effective-mass parameters of AlN and GaN. *Physical Review B*, 52(11), 1995. doi: 10.1103/PhysRevB.52.8132.

[33] I. Vurgaftman, J. R. Meyer, and L. R. Ram-Mohan. Band parameters for III-V compound semiconductors and their alloys. *Journal of Applied Physics*, 89(11):5815, 2001. doi: 10.1063/1.1368156.

[34] J. Wu, W. Walukiewicz, K. M. Yu, J. W. Ager, S. X. Li, E. E. Haller, H. Lu, and W. J. Schaff. Universal bandgap bowing in group-III nitride

alloys. *Solid State Communications*, 127(6):411–414, 2003. doi: 10.1016/S0038-1098(03)00457-5.

[35] Y. P. Varshni. Temperature dependence of the energy gap in semiconductors. *Physica*, 34(1):149–154, 1967. doi: 10.1016/0031-8914(67)90062-6.

[36] R. Pässler. Parameter sets due to fittings of the temperature dependencies of fundamental bandgaps in semiconductors. *physica status solidi(b)*, 216 (2):975–1007, 1999. doi: 10.1002/(SICI)1521-3951(199912)216:23.3.CO;2-E.

[37] S. Nakamura, T. Mukai, and M. Senoh. Candela-class high-brightness InGaN/AlGaN double-heterostructure blue-light-emitting diodes. *Applied Physics Letters*, 64(13):1687, 1994. doi: 10.1063/1.111832.

[38] P. G. Moses and C. G. Van de Walle. Band bowing and band alignment in InGaN alloys. *Applied Physics Letters*, 96(2):021908, 2010. doi: 10.1063/1.3291055.

[39] E. Calleja, M. A. Sanchez-Garcia, F. J. Sanchez, F. Calle, F. B. Naranjo, E. Munoz, U. Jahn, and K. Ploog. Luminescence properties and defects in GaN nanocolumns grown by molecular beam epitaxy. *Physical Review B*, 62(24):16826, 2000. doi: 10.1103/PhysRevB.62.16826.

[40] P. Schley, R. Goldhahn, G. Gobsch, M. Feneberg, K. Thonke, X. Wang, and A. Yoshikawa. Influence of strain on the band gap energy of wurtzite InN. *physica status solidi (b)*, 246(6):1177–1180, 2009. doi: 10.1002/pssb.200880924.

[41] E. S. Hellman. The polarity of GaN: a critical review. *MRS Internet Journal of Nitride Semiconductor Research*, 3(11), 1998. doi: 10.1557/S1092578300000831.

[42] F. Bernardini, V. Fiorentini, and D. Vanderbilt. Spontaneous polarization and piezoelectric constants of III-V nitrides. *Physical Review B*, 56(16), 1997. doi: 10.1103/PhysRevB.56.R10024.

[43] J. S. Speck and S. F. Chichibu. Nonpolar and semipolar group III nitride-based materials. *MRS bulletin*, 34(05), 2009. doi: 10.1557/mrs2009.91.

[44] V. Fiorentini, F. Bernardini, and O. Ambacher. Evidence for nonlinear macroscopic polarization in III-V nitride alloy heterostructures. *Applied Physics Letters*, 80(7), 2002. doi: 10.1063/1.1448668.

[45] M. Yamaguchi, T. Yagi, T. Azuhata, T. Sota, K Suzuki, S. Chichibu, and S. Nakamura. Brillouin scattering study of gallium nitride: elastic stiffness constants. *Journal of Physics: Condensed Matter*, 9:241–248, 1997. doi: 10.1088/0953-8984/9/1/025.

[46] A. E. Romanov, T. J. Baker, S. Nakamura, and J. S. Speck. Strain-induced polarization in wurtzite III-nitride semipolar layers. *Journal of Applied Physics*, 100(2):023522, 2006. doi: 10.1063/1.2218385.

[47] H. Yamada, K. Iso, M. Saito, H. Hirasawa, N. Fellows, H. Masui, K. Fujito, J. S. Speck, S. P. DenBaars, and S. Nakamura. Comparison of InGaN/GaN light emitting diodes grown on m-plane and a-plane bulk GaN substrates. *Physica status solidi (RRL) Rapid Research Letters*, 2(2), 2008. doi: 10.1002/pssr.200701313.

[48] H. Masui, H. Asamizu, T. Melo, H. Yamada, S. C. Iso, K.and Cruz, S. Nakamura, and S. P. DenBaars. Effects of piezoelectric fields on optoelectronic properties of InGaN/GaN quantum-well light-emitting diodes prepared on nonpolar $(10\bar{1}0)$ and semipolar $(11\bar{2}2)$ orientations. *Journal of Physics D: Applied Physics*, 42(13):135106, 2009. doi: 10.1088/0022-3727/42/13/135106.

[49] M. Sawicka, C. Chèze, H. Turski, G. Muziol, S. Grzanka, C. Hauswald, O. Brandt, M. Siekacz, R. Kucharski, T. Remmele, M. Albrecht, M. Krysko, E. Grzanka, T. Sochacki, and C. Skierbiszewski. Ultraviolet light-emitting diodes grown by plasma-assisted molecular beam epitaxy on semipolar gan $(20\bar{2}\bar{1})$ substrates. *Applied Physics Letters*, 102(11), 2013. doi: 10.1063/1.4796123.

[50] A. Zoroddu, F. Bernardini, P. Ruggerone, and V. Fiorentini. First-principles prediction of structure, energetics, formation enthalpy, elastic constants, polarization, and piezoelectric constants of AlN, GaN, and InN: Comparison of local and gradient-corrected density-functional theory. *Physical Review B*, 64(4), 2001. doi: 10.1103/PhysRevB.64.045208.

[51] C. Kittel. *Introduction to solid state physics*. WILEY-VCH Verlag GmbH & Co. KGaA, Weinheim, 8th edition, 2004.

[52] Stephen J. Pearton. *GaN and Related Materials II*. CRC Press, 2000.

[53] C. S. Gallinat, G. Koblmüller, J. S. Brown, and J. S. Speck. A growth diagram for plasma-assisted molecular beam epitaxy of In-face InN. *Journal of Applied Physics*, 102(6):064907, 2007. doi: 10.1063/1.2781319.

[54] Bernard Gil. *III-Nitride Semiconductors and Their Modern Devices*. OUP Oxford, 2013.

[55] J. Neugebauer, T. Zywietz, M. Scheffler, J. Northrup, H. Chen, and R. Feenstra. Adatom Kinetics On and Below the Surface: The Existence of a New Diffusion Channel. *Physical Review Letters*, 90(5), 2003. doi: 10.1103/PhysRevLett.90.056101.

[56] J. E. Northrup, J. Neugebauer, R. M. Feenstra, and A. R. Smith. Structure of GaN (0001): The laterally contracted Ga bilayer model. *Physical Review B*, 61(15):9932, 2000. doi: 10.1103/PhysRevB.61.9932.

[57] C. Adelmann, R. Langer, G. Feuillet, and B. Daudin. Indium incorporation during the growth of InGaN by molecular-beam epitaxy studied by reflection high-energy electron diffraction intensity oscillations. *Applied Physics Letters*, 75(22):3518, 1999. doi: 10.1063/1.125374.

[58] S. Keller, H. Li, M. Laurent, Y. Hu, N. Pfaff, J. Lu, D. F Brown, N. A. Fichtenbaum, J. S. Speck, S. P. DenBaars, and U. K. Mishra. Recent progress in metal-organic chemical vapor deposition of $(000\bar{1})$ N-polar group-III nitrides. *Semiconductor Science and Technology*, 29(11):113001, 2014. doi: 10.1088/0268-1242/29/11/113001.

[59] J. Northrup. Impact of hydrogen on indium incorporation at m-plane and c-plane $In_{0.25}Ga_{0.75}N$ surfaces: First-principles calculations. *Physical Review B*, 79(4), 2009. doi: 10.1103/PhysRevB.79.041306.

[60] A. Urban. *Position-controlled selective area growth of Ga-polar GaN nanocolumns by molecular beam epitaxy: A versatile approach towards semipolar GaN and the characterization of single nanocolumns*. PhD thesis, Georg-August-Universität Göttingen, 2013.

[61] URL www.crystals.saint-gobain.com/LUMILOG_GaN.aspx.

[62] B. Henne. Growth of ingan on semi-polar facets of selective grown gan nanocolumns. Master's thesis, Georg-August-Universität Göttingen, 2013.

[63] T. Djenizian, L. Santinacci, and P. Schmuki. Electron-Beam Induced Nanomasking for Metal Electrodeposition on Semiconductor Surfaces. *Journal of The Electrochemical Society*, 148(3):C197, 2001. doi: 10.1149/1.1348258.

[64] M. Carsten. Charakterisierung mit xps. Master's thesis, Georg- August-Universität Göttingen, 2010.

[65] URL www.amptek.com/pdf/characteristic_xrays.pdf.

[66] Lawrence Berkeley National Library. URL xdb.lbl.gov.

[67] Ture Hinrichsen. Reciprocal space mapping of gan-based heterostructures. Master's thesis, Georg-August-Universität Göttingen, 2012.

[68] A. Somogyi, R. Tucoulou, G. Martinez-Criado, A. Homs, J. Cauzid, P. Bleuet, S. Bohic, and A. Simionovici. ID22: a multitechnique hard X-ray microprobe beamline at the European Synchrotron Radiation Facility. *Journal of Synchrotron Radiation*, 12(2):208–215, 2005. doi: 10.1107/S0909049504030882.

[69] Gema Martínez-Criado, Rémi Tucoulou, Peter Cloetens, Pierre Bleuet, Sylvain Bohic, Jean Cauzid, Isabelle Kieffer, Ewelina Kosior, Sylvain Labouré, Sylvain Petitgirard, Alexander Rack, Juan Angel Sans, Jaime Segura-Ruiz, Heikki Suhonen, Jean Susini, and Julie Villanova. Status of the hard x-ray microprobe beamline ID22 of the European Synchrotron Radiation Facility. *Journal of Synchrotron Radiation*, 19(1):10–18, 2012. doi: 10.1107/S090904951104249X.

[70] *Characterization of Semiconductor Heterostructures and Nanostructures*, chapter 9, pages 361–412. Elsevier B.V., 2013.

[71] V.A. Solé, E. Papillon, M. Cotte, Ph. Walter, and J. Susini. A multiplatform code for the analysis of energy-dispersive X-ray fluorescence spectra. *Spectrochimica Acta Part B: Atomic Spectroscopy*, 62(1):63–68, 2007. doi: 10.1016/j.sab.2006.12.002.

[72] URL http://www.esrf.eu/computing/scientific/FIT2D/.

[73] J. Segura-Ruiz, G. Martínez-Criado, C. Denker, J. Malindretos, and A. Rizzi. Phase separation in single $In_xGa_{1-x}N$ nanowires revealed through a hard x-ray synchrotron nanoprobe. *Nano Letters*, 14(3):1300–1305, 2014. doi: 10.1021/nl4042752.

[74] Katsumi Kishino, Hiroto Sekiguchi, and Akihiko Kikuchi. Improved Ti-mask selective-area growth (SAG) by rf-plasma-assisted molecular beam epitaxy demonstrating extremely uniform GaN nanocolumn arrays. *Journal of Crystal Growth*, 311(7):2063–2068, 2009. doi: 10.1016/j.jcrysgro.2008.11.056.

[75] A. Bengoechea-Encabo, F. Barbagini, S. Fernandez-Garrido, J. Grandal, J. Ristic, M.A. Sanchez-Garcia, E. Calleja, U. Jahn, E. Luna, and A. Trampert. Understanding the selective area growth of GaN nanocolumns by MBE using Ti nanomasks. *Journal of Crystal Growth*, 325(1):89–92, 2011. doi: 10.1016/j.jcrysgro.2011.04.035.

[76] Gregor Koblmüller, Robert Averbeck, Henning Riechert, and Peter Pongratz. Direct observation of different equilibrium Ga adlayer coverages and their desorption kinetics on GaN (0001) and $(000-1)$ surfaces. *Physical Review B*, 69(3), 2004. doi: 10.1103/PhysRevB.69.035325.

[77] H. Li, L. Geelhaar, H. Riechert, and C. Draxl. Computing equilibrium shapes of wurtzite crystals: The exemple of GaN. *Physical Review Letters*, 115, 2015. doi: 10.1103/PhysRevLett.115.085503.

[78] J. E. Northrup and J. Neugebauer. Theory of GaN(1010) and (1120) surfaces. *Physical Review B*, 53(16), 1996. doi: 10.1103/PhysRevB.53.R10477.

[79] C. E. Dreyer, A. Janotti, and C. G. Van de Walle. Absolute surface energies of polar and nonpolar planes of GaN. *Physical Review B*, 89(8), 2014. doi: 10.1103/PhysRevB.89.081305.

[80] Žarko Gačević, Daniel Gómez Sánchez, and Enrique Calleja. Formation mechanisms of gan nanowires grown by selective area growth homoepitaxy. *Nano Letters*, 15(2):1117–1121, 2015. doi: 10.1021/nl504099s.

[81] G. Wulff. Zur frage der geschwindigkeit des wachstums und der aufloesung der krystallflaechen. *Zeitschrift fuer Kristallographie*, 34(449), 1901. doi: 10.1524/zkri.1901.34.1.449.

[82] L. Lymperakis and J. Neugebauer. Large anisotropic adatom kinetics on nonpolar GaN surfaces: Consequences for surface morphologies and nanowire growth. *Physical Review B*, 79(241308), 2009. doi: 10.1103PhysRevB.79.241308.

[83] Tetsuya Kouno, Katsumi Kishino, and Masaru Sakai. Lasing Action on Whispering Gallery Mode of Self-Organized GaN Hexagonal Microdisk Crystal Fabricated by RF-Plasma-Assisted Molecular Beam Epitaxy. *IEEE Journal of Quantum Electronics*, 47(12):1565–1570, 2011. doi: 10.1109/JQE.2011.2175369.

[84] Tetsuya Kouno and Katsumi Kishino. Well-arranged novel InGaN hexagonal nanoplates at the tops of nitrogen-polarity GaN nanocolumn arrays. *AIP Advances*, 2(1):012140, 2012. doi: 10.1063/1.3687237.

[85] X. J. Chen, G. Perillat-Merceroz, D. Sam-Giao, C. Durand, and J. Eymery. Homoepitaxial growth of catalyst-free GaN wires on N-polar substrates. *Applied Physics Letters*, 97(15):151909, 2010. doi: 10.1063/1.3497078.

[86] C I Oppo, J Malindretos, R R Zamani, D Broxtermann, J Segura-Ruiz, G Martinez-Criado, P C Ricci, and A Rizzi. Polarity dependent strongly inhomogeneous In-incorporation in GaN nanocolumns. *Nanotechnology*, 27(35):355703, 2016. doi: 10.1088/0957-4484/27/35/355703.

[87] C. G. Van de Walle, M. D. McCluskey, C. P. Master, L. T. Romano, and N. M. Johnson. Large and composition-dependent band gap bowing in $In_xGa_{1-x}N$ alloys. *Materials Science and Engineering: B*, 59(1):274–278, 1999. doi: 10.1016/S0921-5107(98)00340-7.